# Proteomic Analyses Identify Novel Regulatory Mechanisms of Coinhibitory Receptor PD-1

# Share Your Story

## HARVARD UNIVERSITY
### Graduate School of Arts and Sciences

## DISSERTATION ACCEPTANCE CERTIFICATE

The undersigned, appointed by the

Harvard Integrated Life Sciences

Committee on Chemical Biology

have examined a dissertation entitled

**Proteomic Analyses Identify Novel Regulatory Mechanisms of Coinhibitory Receptor PD-1**

presented by Emily Gaudiano
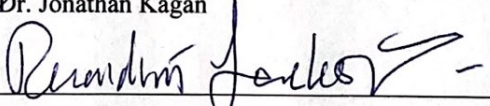
candidate for the degree of Doctor of Philosophy and hereby certify that it is worthy of acceptance.

Signature _____
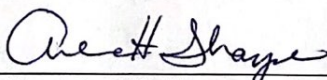
Typed name: Dr. Peter Sorger

Signature _____

Typed name: Dr. Jonathan Kagan

Signature _____

Typed name: Dr. Ruaidhrí Jackson

Signature _____

Typed name: Dr. Arlene H. Sharpe

Date: May 11, 2022

# Proteomic Analyses Identify Novel Regulatory Mechanisms

# of Coinhibitory Receptor PD-1

A dissertation presented

by

**Emily Gaudiano**

to

The Committee on Higher Degrees in Chemical Biology

in partial fulfillment of the requirements

for the degree of

**Doctor of Philosophy**

In the subject of

**Chemical Biology**

Harvard University

Cambridge, MA

May 11, 2022

Dissertation Advisor: Arlene Sharpe, MD PhD                          Emily Gaudiano

# Proteomic Analyses Identify Novel Regulatory Mechanisms

# of Coinhibitory Receptor PD-1

**Abstract**

Coinhibitory immunoreceptor programmed cell death-1 (PD-1, CD279) plays a critical role in mediating T cell exhaustion and blockade of this pathway can promote antitumor immunity. While PD-1 pathway inhibitors are revolutionizing cancer therapy, only a subset of patients respond and show durable remission, highlighting the need to better understand the basic mechanisms by which the PD-1 pathway inhibits T cell functions. Studies assessing PD-1 signaling mechanisms have the potential to identify novel targets for therapeutic intervention in cancer to improve patient responses.

To identify novel mechanisms of PD-1 function, we utilized proximity labeling as an unbiased approach to survey proteins proximal to PD-1 following ligation and identified the mechanosensitive cation channel PIEZO1 as a primary target of PD-1-mediated inhibition. Stimulation of $CD8^+$ T cells through the T cell receptor (TCR) and costimulatory receptor CD28 triggered the activation of PIEZO1 at the immune synapse, while simultaneous ligation of PD-1 countered this activation. We found that mice lacking PIEZO1 selectively on $CD8^+$ T cells exhibited significantly increased tumor growth marked by impaired $CD8^+$ T cell function and this could not be rescued by PD-1 blockade. Conversely, $CD8^+$ tumor infiltrating lymphocytes (TILs) from wild-type (WT) mice treated with PIEZO1 agonist showed greater functionality compared to controls. Coadministration of PIEZO1 agonist and PD-1 blockade significantly reduced tumor burden and improved survival in a PD-1 blockade-unresponsive tumor model. These findings identify PIEZO1 inhibition as an important mechanism by which PD-1 signaling regulates $CD8^+$ T cell functions and suggest that modulating PIEZO1 activity on $CD8^+$ T cells may be a novel approach to augment cancer immunotherapy.

To determine how PD-1 tyrosine-phosphorylation motifs differentially impact downstream signaling, we relied on PD-1 mutant mouse models and proteomic methodology to uncouple the functions of PD-1

immune tyrosine-based inhibition motif (ITIM) and immune tyrosine-based switch motif (ITSM), as well as other potential signaling motifs. We found that ITSM-mutant mice controlled tumor growth similar to PD-1 knockout (KO) mice, but did not full recapitulate PD-1 KO phenotypes. Furthermore, ITIM-mutant mice showed no significant improvement in tumor control, similar to WT mice. To further characterize these differences, we performed proximity phospho-proteomic analysis and PD-1 phospho-peptide pulldowns to assess PD-1 binding interactions and phosphorylation alterations. We confirmed that the ITSM recruits inhibitory phosphatases and kinases to dampen TCR-mediated activation and discovered that the ITIM associates with proteins involved in ubiquitin-mediated degradation, suggesting that the ITIM regulates the degradation of TCR effector proteins. Novel phospho-serine sites identified on the cytoplasmic tail of PD-1 also exhibited unique protein binding behavior, implying that PD-1 retains residual signaling function beyond the ITIM and ITSM. While additional experimentation is necessary to confirm these findings, our results significantly advance our mechanistic understanding of PD-1-mediated signaling.

Together, our studies have discovered a novel regulatory mechanism of PD-1-mediated inhibition and have substantially built upon our understanding of the function of PD-1 signaling motifs. Specifically, our findings demonstrate that PD-1 inhibition of PIEZO1 is therapeutically relevant in cancer and that novel PD-1 phosphorylation sites and binding partners may participate in uncharacterized functions of PD-1.

# Table of Contents

**Acknowledgements**

Words cannot express how fortunate and grateful I am for the endless support I've received from my family, friends and colleagues throughout the course of my PhD. Your encouragement and advice has meant the world to me and I don't know that I could have completed this tumultuous journey without each and every one of you playing an important role. My years at Harvard have been nothing short of incredible, as I was given the opportunity to rub shoulders with the most intelligent minds on Earth. More importantly, these brilliant people have become great friends and I will always think of our time together with fondness.

I want to begin by thanking the first person I encountered at Harvard, Jason Millberg. Though I wasn't the most competitive candidate, you were my cheerleader from day one. You go above and beyond to organize fun and thoughtful events to maintain a strong sense of community within the Chem Bio program. More importantly, you make an effort to get to know each student on a personal level to make us feel at home. I will always appreciate your help and support over the years.

The Chem Bio program would not exist if it weren't for our amazing program chairs Suzanne Walker and Dan Kahne. I want to thank you for maintaining such a stellar program and recruiting not only talented faculty and students, but truly wonderful people. The connections I've made within the Chem Bio program have been invaluable for promoting my positive experience in grad school.

I want to thank my classmates for being such a strong source of support and laughter as we struggled through classes and commiserated about lab life. We always remained a tight-knit group no matter how long we were apart. We have supported each other through many milestones and I look forward to seeing what you all achieve in the future. To Jonnell, Tony, Jake, Nafta, Patrice, Mark, Katherine, Kevin and Anthony -- I will always remember the many fun times we had together at retreats and the many meaningful conversations we've shared over the years. I hope to keep in touch and I am so proud of all of you.

I want to extend a massive thank you to my advisor, Dr. Arlene Sharpe. I am so grateful for your guidance, enthusiasm and encouragement over the years. Whether we were celebrating exciting data or addressing

challenging hurdles, you were there to support me along the way. I believe we both share a willingness to step outside of our comfort zones when it comes to science and joining your lab allowed me to do just that. Thank you for giving a biochemist the opportunity to explore the magnificent world of immunology.

Joining an immunology lab meant that I had a massive learning curve to ascend. I can't thank the Sharpe lab enough for their infinite support and patience as I navigated a new area of research. A special thanks to my mentor Marty, who was tasked with the not-so-easy job of helping me get my footing in lab, along with Thao, who trained alongside me. I think all of those "good lucks" have really paid off. To the big sister I never had, Erica, thank you so much for keeping me afloat when I needed it most. I also want to thank my favorite Sharpe lab alumni, Jefte and Cat, for being great role models and for continuing to remind me that there's a light at the end of the tunnel. I want to thank by bay mates Joon, Raj and Jossef for their comradery and Sarah H and Mike for always keeping the lab in tip-top shape. And to all the other current and past Sharpe lab members, thank you for making my experiencing in the lab one that I will look back on with great joy and appreciation.

I would like to thank my dissertation and defense committee members, Peter Sorger, Wade Harper, Jon Kagan and Ruaidhrí Jackson, for their ongoing support for my research. Your scientific input has been instrumental to my project's success and has contributed to my growth as a scientist.

I owe a heartfelt thank you to all of my collaborators and research cores, specifically the Laboratory of Systems Pharmacology, Micron Core, and Flow Core, who spent countless hours performing experiments, troubleshooting, planning and discussing results with me. Your efforts significantly contributed to the progress of my research and I so greatly appreciate your dedication to my projects.

To my dear friends, your support outside of the lab has arguably been the most critical and grounding. You have always reminded me that there is a life worth living outside the stress of work. Thank you for being there when I needed you the most, and more importantly, for convincing me to travel the world with you. While it's not easy to verbalize the crushing defeat brought on by failed experiments and incessant

troubleshooting, you were always willing to listen. To my dimes, Turks crew, BC gals, Cape crew, D'Andrea affiliates, Kelly, Alyssa and many more – I appreciate you more than you know.

Lastly, I owe the greatest thanks of all to my family. Mom, Dad, Mikey and Matty – I couldn't love you more if I tried. Writing this now, it's hard for me to verbalize just how much your love and support has meant to me. You have taught me to be hard working, persistent, resourceful, thoughtful, communicative, generous and patient, and for that I owe my success to you. Mom and Dad – I know that when I am stressed, you're stressed and I can't thank you enough for helping me to shoulder that in any way possible, whether it be doing my laundry or driving all over to shuttle me around. Mikey and Matty – your sense of humor helped me to stay positive and your encouragement pushed me through. Thanks for being the best friends I could ever ask for. We are so lucky to have each other.

*"The woods are lovely, dark and deep.*

*But I have promises to keep,*

*And miles to go before I sleep,*

*And miles to go before I sleep."*

-Robert Frost

# Chapter 1:

# Introduction

## 1.1 Introduction

The adaptive immune system has evolved countless mechanisms to defend against a wide variety of invading pathogens. Importantly, the immune system must regulate these responses to maintain peripheral tolerance and protect healthy tissues from inflammatory tissue damage[1,2]. The balance between immunity and immune tolerance is regulated by costimulatory and coinhibitory molecules[1–3]. T cells express costimulatory and coinhibitory molecules for optimal activation and subsequent attenuation of positive signaling, respectively[2,4,5]. Naïve T cell activation in the lymph node requires two signals[6]. First, engagement of the T cell receptor (TCR) by major histocompatibility complex (MHC) I- or II-presented peptides (signal one), initiates a downstream signaling cascade that promotes T cell proliferation, differentiation and effector functions[3,7,8]. Simultaneous engagement of the costimulatory receptor CD28 by its ligands B7-1 or -2 (CD80 or CD86) is required for full T cell activation initiated by the TCR (Fig. 1)[3,6,9–11]. TCR ligation lacking a second costimulatory signal can lead to T cell anergy, a hyporesponsive state with low interleukin-2 (IL-2) production believed to be a tolerogenic mechanism[6,12]. In addition to the two-signals, signal 3 provided by inflammatory cytokines including interleukin-12 (IL-12) and Type I interferon (IFN) promotes T cell differentiation and acquisition of effector functions[3,9]. These signals culminate in T cell activation, differentiation, acquisition of effector functions and proliferation.

Early during activation, negative regulators are induced to counter the activation program[1–3]. Programmed cell death-1 (PD-1, encoded CD279) is a coinhibitory receptor expressed on the surface of T cells, functioning as an attenuator of TCR and costimulatory receptor signaling[1,2,13]. Interaction with either of its ligands, programmed cell death ligand-1 (PD-L1; B7-H1; CD274) or -2 (PD-L2; B7-H2; CD273), results in PD-1-mediated dephosphorylation of TCR-related components and inhibition of proliferative and effector functions including cytokine production, cytolysis, $Ca^{2+}$ flux, cytoskeletal rearrangements, migration and metabolic machinery[14–20]. While PD-1 inhibitory signaling plays a significant role of maintaining tolerance, it has received considerable attention for its role in contributing to T cell exhaustion, a discrete state of T cell differentiation caused by chronic antigen exposure. Exhausted T cells are dysfunctional T cells that progressively lose effector functions, and develop in the settings of cancer and chronic viral infection[1,2,21]. Tumors exploit the PD-1 pathway to avoid immune-mediated destruction.  Tumor cells can express PD-

L1/2 ligands that engage PD-1 on T cells, and PD-L1 expression on tumor cells can contribute to inhibition of antitumor immunity [1,22,23]. Guided by these principles, researchers developed PD-1 checkpoint blockade therapies to combat immune evasion by tumors, and these have emerged as revolutionary treatments for cancer patients in over 20 different cancer types[4,21,24–27]. Unfortunately, however, a significant subset of patients do not respond to PD-1 checkpoint blockade therapy or do not experience long lasting remission[1,23].

Despite widespread success of PD-1 pathway inhibitors in the clinic, the molecular signaling mechanisms governing PD-1-mediated inhibition in T cells are not well understood[1,17]. For this reason, a better understanding of PD-1 signaling could identify novel targets for single agent or rationale combination therapy to improve antitumor immunity and extend the benefit of cancer immunotherapy. In this chapter I first will discuss PD-1 function and how this function has been utilized in the clinic to stimulate robust T cell responses to fight cancer (1.2). Next, I will review our current understanding of the specific molecular mechanisms that mediate PD-1 inhibitory signaling, which result in attenuation of T cell function (1.3). I will also examine the role of mechanosensation in immune cells, as our studies have discovered a novel role of PD-1 in inhibiting mechanosensation that is required for optimal T cell function (1.4). Finally, I will provide an overview of this thesis, which substantially builds upon our understanding of how the PD-1 receptor functions (1.5).

## 1.2 PD-1 function and clinical relevance

PD-1 was discovered in 1992 by the Honjo lab, who sought to identify molecular mechanisms involved in self-nonself discrimination by the immune system[13]. While studying apoptosis as a feature of self-reactive immature T cells, the Honjo lab identified PD-1 as a novel gene potentially involved in activating the classical programmed cell death pathway, as its name suggests[13,28]. Subsequent studies assessing activation-induced PD-1 expression on lymphocytes, PD-1-mediated inhibition on B cells and lupus-like autoimmunity in PD-1 deficient mice demonstrated, however, that PD-1 functions as negative regulator of immune cell responses, rather than an inducer of programmed cell death[29–32]. Surveillance of B7 homology-based

molecules lead to the identification of PD-1 ligands PD-L1/2, providing a mechanism for the induction of PD-1 inhibitory signals[33–35].

PD-1 is expressed on T cell, B cells, natural killer (NK) cells and natural killer T (NKT) cells, while its expression and function on activated monocytes and dendritic cells (DCs) is still debated[2]. PD-1 expression is induced following TCR or B cell receptor (BCR) ligation and its surface expression can be detected 24 h following T and B cell activation[2,29]. Seminal work from the Sharpe lab elucidated that inhibitory signals propagated by PD-1 are important for regulating central and peripheral tolerance[2,36–38]. Upregulation of PD-1 following TCR engagement on CD8$^+$ CD4$^+$ thymocytes inhibited ERK activation and expression of anti-apoptotic protein Bcl-2 to inhibit TCR-mediated positive selection of thymocytes[37]. Interestingly, elimination of PD-L1, but not PD-L2, was sufficient to resolve defects resulting from PD-1 overexpression in murine thymocytes[37]. Moreover, self-reactive T cells that escaped negative selection in the thymus were controlled by PD-1 ligation in the periphery[2]. Initial studies of T cell-mediated diabetes explored the necessity of PD-L1 and PD-L2 in regulating peripheral tolerance[36]. Transfer of prediabetic T cells into PD-L1/2 wild-type (WT) or knockout (KO) non-obese diabetic (NOD) severe combined immunodeficient (SCID) mice and into bone marrow chimeras expressing PD-L1/2 only on nonlymphoid tissues showed that both PD-L1 and PD-L2 played a role in dampening CD4$^+$ T cell effector function, but PD-L1 uniquely protected the pancreas from self-reactive T cell-mediated tissue damage[36]. In addition, PD-1 KO CD8$^+$ OT-1 adoptive transfer studies in RIP-OVA mice demonstrated that PD-1/PD-L1 interactions in cross-presenting DCs were critical for regulating the induction of tolerance, while PD-L1 expression on parenchymal cells controlled self-reactive effector T cell responses to maintain this tolerance[38].

Given the emerging role of the PD-1 pathway in regulating self-tolerance, concurrent studies explored the role of PD-1 in mediating tumor immunity. Work pioneered by the Allison lab discovered that antibody blockade of coinhibitory receptor CTLA-4, which sequesters CD28 ligands B7-1/2 to prevent CD28 ligation and optimal T cell activation, resulted in tumor rejection, proving that tumors actively inhibited the immune system to evade immune-mediated destruction[39]. The similar role of PD-1 as a T cell inhibitor led researchers to assess the role of the PD-1 pathway in cancer progression. Multiple studies found that

expression of PD-L1 on various tumor types resulted in worse prognosis marked by a decrease in CD8^{+} T cell infiltration[40–42]. Moreover, antibody blockade of PD-1 or PD-L1 resulted in potent antitumor responses in mice driven by improved immune T cell activation, pro-inflammatory cytokine production, cytolysis, and CD8^{+} T cell infiltration in the tumor[41,43,44]. Together, these studies proved that the PD-1 pathway is a primary source of immune evasion in numerous cancer types and could be targeted to elicit antitumor immunity. In response to these findings, PD-1 and CTLA-4 blocking antibodies were designed and optimized for use in clinical trials. Early clinical trials for CTLA-4 and PD-1 blockade in melanoma and refractory tumors, respectively, resulted in improved median survival and showed evidence of antitumor activity, with many more successful trials to follow[27,45,46]. Currently, FDA approval of PD-1 and PD-L1 blocking antibodies allows for the treatment of non-small cell lung cancer, melanoma, renal cell carcinoma, bladder cancer and colorectal cancer among others[23,47]. Unfortunately, while many single and combination immunotherapies decrease tumor burden and increase overall survival for many patients, a significant subset of patients do not respond to PD-1 therapy or do not experience long-lasting remission despite expression of these molecules[1,23–26].

**1.3 PD-1 signaling mechanisms**

To properly address the variability of responses experienced by patients treated with PD-1 blockade therapy, it is crucial to develop a better understanding of the intracellular signaling mechanisms driving PD-1-mediated inhibition. Despite agreement in the literature regarding the role of PD-1 as a negative T cell regulator, the mechanisms by which PD-1 inhibits T cell function are widely disputed. PD-1 is type I transmembrane receptor containing an extracellular stalk with an immunoglobulin (Ig) superfamily domain, a transmembrane domain and a flexible cytoplasmic tail[2]. As a non-enzymatic membrane receptor, PD-1 exercises its inhibitory function via the recruitment of tyrosine phosphatases following PD-L1/2 ligation and subsequent phosphorylation (Figure 1.1a). The kinase that phosphorylates PD-1 has not been determined, though tyrosine protein kinase LCK and c-terminal Src kinase (CSK) are involved in the TCR signaling cascade and have been implicated in PD-1 phosphorylation[15,16]. SH2-containing protein tyrosine phosphatases SHP1 (PTPN6) and SHP2 (PTPN11) bind two tyrosine-containing immunoreceptor motifs on the PD-1 cytoplasmic tail: an immunoreceptor tyrosine-based inhibition motif (ITIM) and an

immunoreceptor tyrosine-based switch motif (ITSM)[2,14,15,30,48]. Recruitment of SHP1 and SHP2 to the cytoplasmic tail of PD-1 results in dephosphorylation of TCR , CD28 and downstream effector proteins, leading to attenuation of T cell function (Figure 1.1b-c)[14–16,30,49]. While SHP2 associates with both the ITSM and ITIM, SHP1 associates primarily with the ITSM, although some groups have not been able to identify SHP1 association with PD-1[14,15,19,50]. Moreover, affinity purification mass spectrometry studies found that signaling lymphocytic activation molecule-associated protein SAP (SH2D1A) opposed PD-1 signaling by shielding tyrosine phosphorylation sites from SHP2, suggesting that negative regulators of inhibitory signaling also exist in T cells[50].
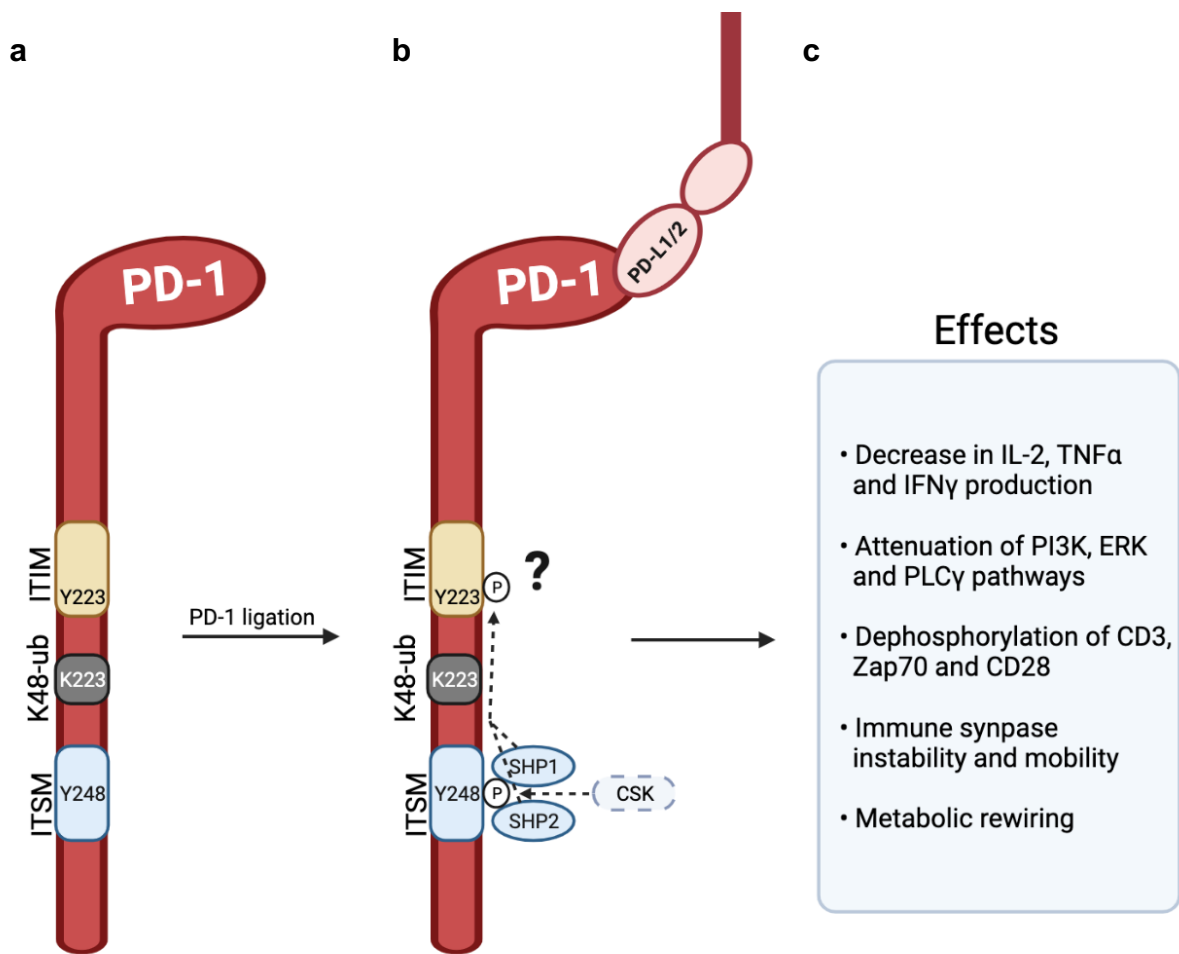


**Figure 1.1: Current model of PD-1 signaling.** a) The structure of PD-1 containing tyrosine phosphorylation motifs and K48-linked ubiquitination site on the cytoplasmic tail[48,52]. b) Phosphatase and kinase recruitment to the cytoplasmic tail of PD-1 following ligation by PD-L1/2[48]. c) Effects of PD-1-mediated inhibition observed in human and murine CD8^{+} and CD4^{+} T cells[17]. Solid lines and arrows originating from proteins depict strong associations with PD-1 while dotted lines and arrows depict less robust associations with PD-1. Question mark denotes unknown function. Schematic created using BioRender.

Single tyrosine to phenylalanine mutation in the ITIM or ITSM sequence of PD-1 enabled the investigation of each motif's distinct function[48]. Experiments conducted using Jurkat cells, human T cell blasts, B cells and CD4^{+} and CD8^{+} T cells, as well as synthetic cell systems have demonstrated that PD-1 ITSM mutant cells exhibit increased cytokine production, proliferation and TCR-mediated signaling pathway activation marked by a lack of SHP2 recruitment compared to ITIM mutant cells[14–16,19,30,49,50]. However, the distinct role of each motif in driving effective PD-1 signaling is not clearly understood[14,19,48,50]. Because mutation in the ITSM significantly attenuates PD-1 effector functions compared to mutation in the ITIM, ITSM recruitment of SHP2 is thought to be the primary mediator of PD-1 signaling[14,30,48,50]. Interestingly, T cell-specific SHP2 KO mice respond to PD-1 blockade and T cells from these mice acquire a dysfunctional state when exposed to chronic antigen, suggesting that SHP-2 modulates select exhaustion features in T cells and that additional factors are involved in mediating PD-1 signaling[51]. Furthermore, these studies do not comment on a potential function for the ITIM. These data suggest that SHP2 association with PD-1 is more complex than previously characterized and that unidentified proteins are necessary for potentiating PD-1-mediated inhibition.

In addition to tyrosine phosphorylation sites, a ubiquitin site was recently identified on the cytoplasmic tail of PD-1 (Figure 1.1a)[52]. In studies examining downregulation of PD-1 surface expression, PD-1 was found to be ubiquitinated on a conserved lysine residue (Lys223) in between the ITIM and ITSM[52]. K48-linked poly-ubiquitination of PD-1 was carried out by E3 ligase FBXO38, leading to the subsequent downregulation and degradation of PD-1[52]. Moreover, mice lacking FBXO38 in T cells experienced increased tumor burden due to high surface expression of PD-1, which was reversed with PD-1 blockade[52]. These studies introduce an alternative method to blocking PD-1 by promoting its degradation through intracellular mechanisms and emphasize that aspects of PD-1 signaling and regulation remain to be characterized.

Direct targets of PD-1 inhibitory phosphatases have also not been well-established. Western blotting in human T cell blasts and PD-1 phospho-peptide pulldowns in Jurkat cells have shown that PD-1 association with SHP2 resulted in the dephosphorylation of the CD3$\zeta$ chain as well as TCR-effector kinase ZAP70, which triggered the down-regulation of TCR-induced signaling pathways and effector functions[15].

Conversely, *in vitro* studies using a synthetic cell system reported a direct and preferential dephosphorylation of the cytoplasmic tail of CD28 by the PD-1/SHP2 complex[16]. Interestingly, the studies demonstrating CD28 dephosphorylation in Jurkat cells observed no dephosphorylation of CD3 subunits or ZAP70, conflicting with previous data[15,16]. *In vivo* studies also demonstrate a necessity for CD28 ligation in processing PD-1-mediated inhibition in exhausted CD8^{+} T cells in the context of lymphocytic choriomeningitis virus (LCMV) and cancer[53]. Direct dephosphorylation of CD3 subunits or CD28 by SHP2 would significantly influence downstream molecular events that have been observed upon PD-1 ligation, yet the preferred targets of PD-1-mediated inhibition have not been determined.

Downstream of TCR and CD28 inhibition, PD-1 ligation results in the attenuation of various effector functions in primary human and murine CD4^{+} and CD8^{+} T cells (Figure 1.1c). Downregulation of PI3K/AKT, Ras/ERK, PKC$\theta$/NF$\kappa$B and PLC$\gamma$/NFAT pathways and stimulation of basic leucine transcription factor ATF-like (BATF) together decrease the production IL-2, IFN$\gamma$ and TNF$\alpha$ cytokines, reduce the expression anti-apoptotic proteins Bim and Bcl-X$_L$ and impair CD4^{+} and CD8^{+} T cell proliferation[14,17,30,49,54–56]. In addition to disrupting signal transduction, studies investigating primary human CD4^{+} T cell metabolism have also highlighted a role for PD-1 in promoting beta-oxidation while suppressing oxygen consumption and impairing CD4^{+} T cell glycolysis and glutaminolysis, emphasizing a role for PD-1 in regulating metabolic function of CD4^{+} T cells[20]. Furthermore, PD-1 ligation controls murine CD8^{+} T cell motility and suppresses cell couplings between T cells and tumor cells in the tumor microenvironment, suggesting a significant role for PD-1 in regulating actin cytoskeletal dynamics[18,57]. Given the dramatic changes observed in CD4^{+} and CD8^{+} T cells upon PD-1 ligation and the complexity of membrane bound signaling, it is likely that additional mechanisms are necessary to attenuate the function of unidentified PD-1 target proteins, thereby influencing cancer pathogenesis. Since PD-1 biologics target only surface interactions, studying intracellular signaling poses an attractive avenue for determining whether these molecular events govern responsiveness to immunotherapy. In this way, mechanistic studies may uncover novel targets for cancer therapeutics that overcome the challenges faced by extracellular blockade, including penetration of antibody therapeutics in solid tumors[58].

### 1.4 Mechanosensation in immune cells

The studies conducted in this thesis have identified mechanosensation as a significant regulator of CD8^{+} T cell biology. For this reason, it is important to evaluate the various forces imparted on immune cells throughout the body and understand how these forces are translated into meaningful biological signals. Immune cell intravasation and migration to tissues exposes cells to a variety of forces, including shear stress, cyclical pressure, membrane deformation and cytoskeletal contractility[59–61]. Forces applied from the outside of the cell are termed "outside-in" forces, in that the external environment imparts force on the outside of the cell to induce signaling inside of the cell[62,63]. In addition, the generation of internal forces enables "inside-out" sensing which surveys stiffness, surface topography and ligand density in the extracellular environment, all of which are common functions of migrating or interacting immune cells[59,62–64]. Many studies have determined that immune cells, as well as various parenchymal cells, not only endure these forces, but translate force into biological signals[59,62].

The discovery of mechanosensitive cation channels PIEZO1 (Fam38a) and PIEZO2 (Fam38b) has shed light on this important paradigm of cellular biology[65]. Until PIEZO1 and 2 were found to conduct mechanically active currents in a mouse neuroblastoma cell line, little progress had been made to characterize mechanosensors in mammals, as mammals do not have an ortholog for mechanically active ion channels studied in invertebrates[66,67]. The evolutionarily conserved PIEZO1 and 2 proteins play critical roles in various mechanotransduction processes, including pain sensation, proprioception, vascular development, bone remodeling, airway stretching, response to vascular and lymphatic flow, red blood cell volume, innate immunity and aging in the central nervous system, among others[65,68–76]. Structurally, PIEZO1 and 2 are homo-trimeric proteins containing three curved, nonplanar propellor blades, an extracellular cap and a central ion conducting pore[77–80]. External force deforms the cell membrane, known as the force-from-lipid model, and this lateral membrane tension opens the channel to induce an influx of cations (Figure 1.2a-b)[77,79,81–83] . Multiple monovalent and divalent ions are able to pass through the central pore of PIEZO channels, however, studies have largely focused on $Ca^{2+}$ influx and its influence on downstream signaling[81]. In addition, anchorage to dynamic cytoskeletal or extracellular matrix (ECM) proteins can pull PIEZO channels open, a process termed the tethered-spring or force-from-filament model

(Figure 1.2a,c)[62,64,77,83–85]. Both force-from-filament and force-from-lipid models contribute to ion channel gating, a process by which an ion channel transitions between its open and closed conformation to regulate the passage of electrical current through the ion-conducting pore, leading to downstream signaling (Figure 1.2a-c)[86]. The fate of $Ca^{2+}$ entering the cell depends largely on the cell type. PIEZO1 is expressed on a variety of cells types and tissues, including the lungs, bladder, pancreas, skin, bone, endometrium, heart and immune cell subsets, where it regulates a myriad of physiological functions mentioned above[64–66,69,70,73,74,87–89]. More recent studies have begun to explore PIEZO1 function in adaptive immunity, namely in T cells[90,91]. Conversely, PIEZO2 is highly expressed in sensory dorsal root ganglia where is senses touch, pain, movement and airway stretching, while PIEZO1 is not expressed in sensory neurons[66,71,72,87]. Together, these studies suggest that force is an appreciable cellular stimulus and that mechanosensation is critical for cellular function, particularly in immunity.
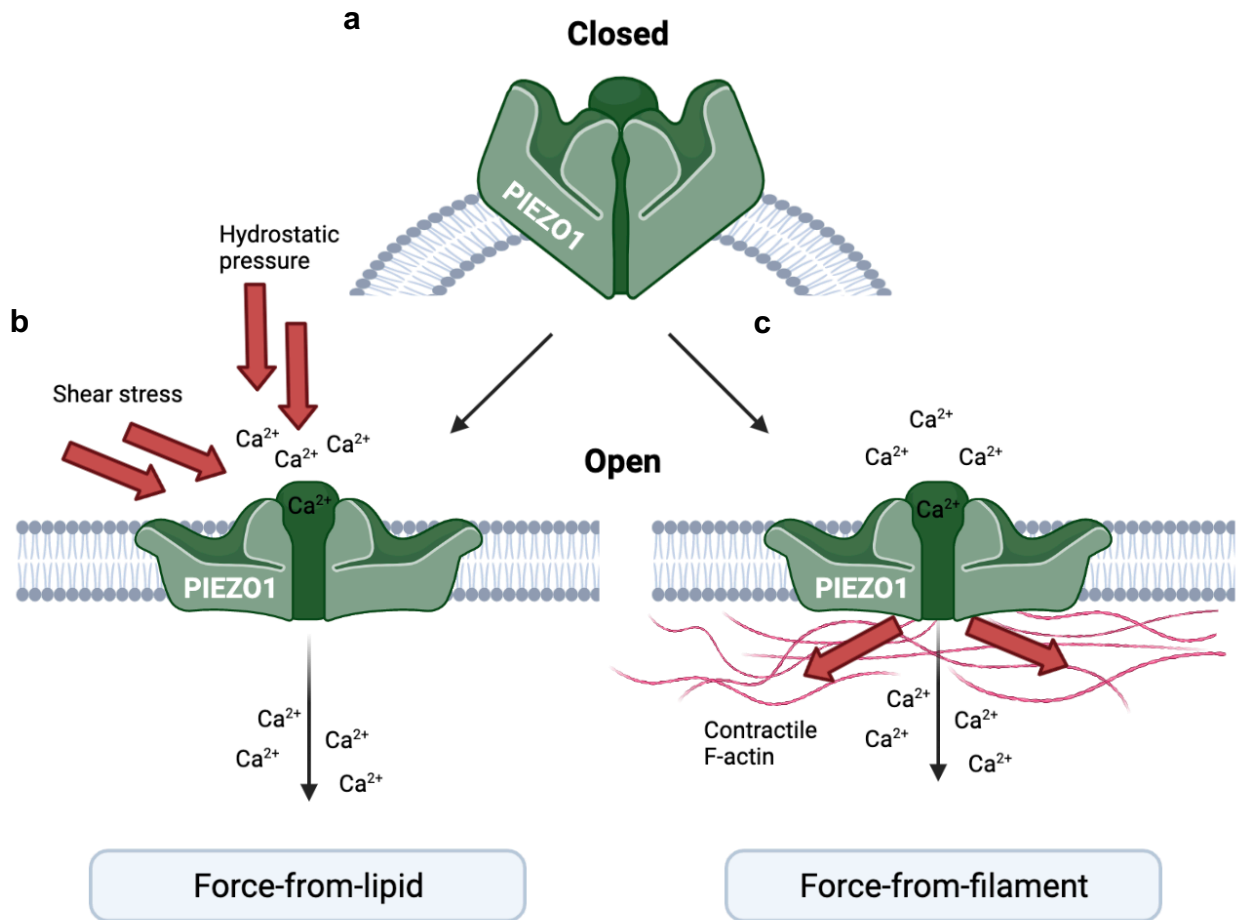
**Figure 1.2: PIEZO1 gating mechanisms.** a) PIEZO1 in a closed confirmation in the plasma membrane in the absence of force. b) Force-from-lipid model where external forces applied to the cell deform the plasma membrane and gate PIEZO1 in an open confirmation[83]. c) Force-from-filament model where forces from contractile cytoskeleton filaments tethered to PIEZO1 pull on the channel to gate it in an open confirmation[83]. Schematic created using BioRender.

While the function of PIEZO1 in immune cells has recently emerged, it is well-established that lymphocyte migration and activation are mechanosensitive processes[73,74,90,91]. To achieve movement throughout the body, lymphocytes rely on retrograde F-actin flow and catch-bond mechanics mediated by integrin adhesions to induce cell polarity for migration while shear force from fluid flow and catch-bond mechanics mediated by selectins regulate rolling and adherence to blood vessel walls[59,92–94]. Catch bonds refer to bonds, often between ligand-receptor pairs, that have increasing lifetime up to an optimal applied force, but decrease with increasing force beyond the threshold[59,85]. Since immune cells require direct cell-cell communication for function, many ligand receptor interactions depend on mechanosensitive catch bonds to mediate signaling, Specifically in T cells, catch bonds are formed between MHCI/II and the TCR during lymphocyte activation[59,94–96]. Studies assessing mechanosensation at the APC/T cell interface have found that the TCR mechanically samples antigen, uses force to assess substrate stiffness and experiences increased and prolonged signaling under higher levels of tension, which is marked by persistent $Ca^{2+}$ influx[59,94–97]. In addition, the actinomyosin cytoskeleton regulates T cell responses to environmental mechanical rigidity and applies forces within the immune synapse to activate mechanosensitive receptors and induce receptor clustering[59,95]. Moreover, forces exerted by cytotoxic T cells at the immune synapse mediated by actin protrusions potentiate the release of cytotoxic granules for target cell killing[59,98,99]. Preliminary reports using mechanically strained DNA probes linked to a fluorescent reporter have also observed force transmission through the PD-1/PD-L2 complex[97]. Activated OT1 CD8^{+} T cells imaged on DNA probes containing PD-L2 resulted in a measurable piconewton force through PD-1, suggesting the storage of mechanical information by various immune cell receptors[97]. These studies underscore the necessity of mechanosensation for optimal T cell activation and function and introduce the notion that regulatory mechanisms likely exist to counter mechano-mediated signaling.

**1.5 Thesis overview**

Despite clinical success of PD-1 blockade in treating numerous cancer types, the majority of patients do not show long lasting remission[1,23–26]. Unfortunately, the mechanisms underlying PD-1 function remain unclear, highlighting the need to better understand PD-1 signaling to improve the efficacy and durability of PD-1 immunotherapy in cancer patients, and develop rationale combination therapies[1,17,23,25].

In this thesis, we investigate intracellular signaling mechanisms driving PD-1-mediated inhibition. In Chapter 2, we describe an unbiased proximity labelling platform used to identify novel mediators and targets of PD-1 signaling. We show that PD-1 associates with mechanosensitive ion channel PIEZO1 over time, and this association results in PIEZO1 inactivation at the immune synapse, where it is required for optimal T cell activation. Mice deficient in PIEZO1 in CD8$^+$ T cells have increased tumor burden that cannot be reversed by PD-1 blockade, confirming the necessity of PIEZO1 in regulating antitumor T cell responses. Mice treated with PIEZO1 agonist in combination with PD-1 blockade in a PD-1 blockade-resistant tumor model significantly attenuate tumor growth, highlighting PIEZO1 as a potential therapeutic target in cancer. In Chapter 3, we examine the distinct functions of the PD-1 ITIM and ITSM *in vivo* and find that ITSM mutant mice control tumor growth similar to PD-1 KO mice, while tumor growth kinetics in ITIM mutant mice resemble those observed in WT mice. Using various proteomic methods, we confirm the role of the ITSM in recruiting effector phosphatases and kinases to inhibit T cell function and identify a potential role for the ITIM in recruiting ubiquitin ligase machinery to potentially regulate the degradation of TCR effector proteins. Additionally, we identify novel phospho-serine sites on the cytoplasmic tail of PD-1 and demonstrate unique protein binding activity that may contribute to PD-1 function. These studies identify a novel mechanism of PD-1 inhibition through regulation of mechanosensation and further elucidate the distinct mechanisms by which PD-1 signaling motifs execute their inhibitory functions. Moreover, methods described in this thesis can be applied to immunoreceptors for which signaling remains unclear.

# Chapter 2:


# PD-1 inhibits PIEZO1 on CD8+ T cells to impair antitumor immunity

**2.1 Introduction**

The coinhibitory receptor PD-1 has received considerable attention for its role in contributing to T cell exhaustion during chronic infection and cancer[1,2]. PD-1 pathway inhibitors are FDA approved for treating over 20 types of cancer and have shown tremendous success in a subset of patients[47]. However, most cancer patients do not show durable responses and patients with specific cancer types experience little to no benefit from PD-1 pathway inhibitors[24–26] Consequently, intense efforts are focused on identifying potential combination treatments that can synergize with PD-1 blockade to benefit more patients.

Despite its widespread use in the clinic, there is a limited mechanistic understanding of PD-1 signaling. Ligation of PD-1 on CD8$^+$ T cells by its ligands PD-L1 and PD-L2 results in the attenuation of various cellular processes driven by engagement of the TCR and costimulatory molecule CD28[17,100]. PD-1 plays a pivotal role in regulating the dephosphorylation of TCR-related components and inhibiting activation of T cell proliferative and effector functions including cytokine production, cytolosis, Ca$^{2+}$ flux, cytoskeletal rearrangements, migration and metabolic machinery[14–20]. PD-1 exerts its inhibitory functions, at least in part, through the recruitment of SH2-containing tyrosine phosphatases SHP2 and SHP1, which bind tyrosine phosphorylation motifs, ITIM and ITSM, in the PD-1 cytoplasmic tail[14,15,19,30,48]. However, the precise mechanisms by which PD-1 and SHP2/SHP1 counter this activation program remain unclear. Recent studies have shown that T cell-specific SHP2 KO mice respond to PD-1 blockade and T cells from these mice acquire a dysfunctional state when exposed to chronic antigen[51]. These data suggest that phosphatase association with PD-1 is more complex than previously characterized and that unidentified proteins and signaling pathways may play a role in mediating PD-1 inhibition. Thus, we predicted that additional unidentified proteins contribute to PD-1-mediated CD8$^+$ T cell inhibition and hypothesized that these proteins may provide novel therapeutic targets to augment PD-1-based immunotherapy.

To test this hypothesis, we developed an unbiased proximity-labeling platform to identify proteins recruited to the cytoplasmic tail of PD-1 following ligation and identified the mechanosensitive ion channel PIEZO1 as a primary target of PD-1-mediated inhibition. PIEZO1 is expressed on a variety of cancer, epithelial and immune cell subsets where its activity can be regulated by both force-from-lipid (shear stress, cyclical

pressure, membrane deformation) and force-from-filament (actinomyosin contractility, ECM tethering) mechanics that gate the ion channel in an open confirmation allowing $Ca^{2+}$ to influx [65,68,73,74,76,86–88,90,101]. We found that stimulation of $CD8^+$ T cells through TCR and CD28 engagement triggered the activation of PIEZO1, consistent with previous reports[90]. Notably, simultaneous ligation of PD-1 countered PIEZO1 activation and subsequent $Ca^{2+}$ influx. Moreover, mice deficient in PIEZO1 in $CD8^+$ T cells exhibited significantly increased tumor growth. $CD8^+$ tumor infiltrating lymphocytes (TILs) isolated from these mice were less abundant, less activated and less cytotoxic. Importantly, tumor-bearing $CD8^+$-specific PIEZO1 KO had diminished response to PD-1 blockade. In complementary studies, WT tumor-bearing mice treated systemically with PIEZO1 agonist Yoda1 showed increased activation of effector $CD8^+$ T cells in the TME as well as decreased tumor burden and improved survival when combined with PD-1 blockade. Our results identify inhibition of PIEZO1 activity as a novel mechanism by which PD-1 mediates its inhibitory functions and suggest that pharmacological engagement of PIEZO1 may be an effective combination therapy to augment PD-1 inhibitors in cancer patients.

## 2.2 Results

*Proximity labelling identifies PD-1 and PIEZO1 association*

Despite the clinical success of PD-1 pathway inhibitors, the proximal signaling events following ligation of PD-1 by PD-L1/2 remain unclear[1,2,17]. Previous proteomic immunoprecipitation methods used to identify direct binding partners of PD-1 did not characterize membrane dynamics and protein localization changes proximal to PD-1 in real time[15,50]. To circumvent these issues, we designed a multiplexed proximity-labelling proteomics platform to spatially and temporally determine the molecular events that occur following PD-1 ligation (Figure 2.1a)[102,103]. First, we generated Jurkat cell lines stably expressing human or murine PD-1 fused to an ascorbate peroxidase 2 (APEX2) labelling probe on the C-terminus of the PD-1 cytoplasmic tail (Figure 2.S1a)[102]. PD-1-APEX2-expressing Jurkat cells were sorted and assessed for labelling efficiency using anti-streptavidin Western blotting (Figure 2.S1b-c). Tosyl-activated Dynabeads were covalently coupled to CD3 and CD28 crosslinking antibodies and PD-L1 (TCR-PD-L1) or control ligand (murine $IgG_1\kappa$, $mIgG_1\kappa$, TCR-control) to provide primary and costimulatory signals for T cell activation while driving strong inhibitory signals through PD-1 (Figure 2.S2). Following incubation in labelling media containing biotinyl

tyramide, PD-1-APEX2-expressing Jurkat cells were co-cultured with TCR-PD-L1 or TCR-control beads for 0, 2, 5, 10 and 20 min (Figure 2.1b). Addition of $H_2O_2$ to the cell:bead co-cultures during the last minute of each timepoint induced biotinylation of proteins within a 10nm radius of the PD-1 cytoplasmic tail (Figure 2.1a, Figure 2.S1c). Sample fractions were lysed and biotinylated proteins were pulled down using streptavidin beads. Samples were trypsin-digested, treated with tandem mass tag (TMT) labels, pooled and quantified by triple-stage mass spectrometry 3 ($MS^3$) to identify proteins in close proximity to the PD-1 cytoplasmic tail[104].

To quantify the co-localization of PD-1 with top hit proteins over time following PD-L1 ligation compared to TCR stimulation alone, we calculated scaled TMT ratios of identified proteins in each condition. Consistent with previous reports[14,19,30,50], we observed a strong enrichment of phosphatase SHP2 peptides over time following TCR-PD-L1 ligation compared to TCR-control stimulation using both human and murine PD-1 constructs, confirming that SHP2 is recruited to PD-1 following ligation to mediate inhibitory signaling (Figure 2.1c, Figure 2.S3a). Strikingly, we also identified a robust enrichment of peptides from mechanosensitive ion channel PIEZO1 over time following PD-L1 ligation compared to control stimulation, suggesting that PIEZO1 closely associates with PD-1 following ligation (Figure 2.1d, Figure 2.S3b).

We next analyzed the recruitment kinetics of previously reported mediators and targets of PD-1 signaling, including phosphatase SHP1, CD3 subunits, CD28 and ZAP70[14–16]. While we detected significant enrichment of SHP1 over time following PD-1 ligation compared to TCR stimulation, the magnitude of enrichment was dramatically lower than SHP2 or PIEZO1 (Figure 2.1e, Figure 2.S3c). We also did not observe robust recruitment of CD3 subunits, CD28 or ZAP70 (Figure 2.1f-g, Figure 2.S3d-i and Figure 2.S4a-d). Similarly, one-way hierarchical clustering did not reveal a significant correlation among PD-1 and SHP1, CD3 subunits, CD28 or ZAP70 (Figure 2.1h, Figure 2.S4e). It is likely that these proteins constitutively localize with PD-1 during both activation and inhibition at the immune synapse, and therefore, recruitment over a distance is not captured[19]. However, one-way hierarchical clustering revealed a significant correlation among PD-1, SHP2 and PIEZO1, suggesting similar recruitment kinetics of SHP2

and PIEZO1 in response to PD-1 ligation (Figure 2.1h, Figure 2.S4e). These results imply a functional role for PIEZO1 in PD-1-mediated inhibition of T cells that has not yet been explored.

To assess the landscape of protein localization changes following TCR stimulation alone or with PD-1 ligation, we used gene ontology (GO) Term analysis to compare pathways that were enriched in PD-L1 or TCR stimulated conditions. We found that clathrin-mediated endocytosis and membrane trafficking were among the top pathways enriched in TCR-PD-L1 conditions compared to TCR-control conditions, suggesting rearrangement of the plasma membrane and cytoskeleton to alter receptor turnover and prevent stable contact at the immune synapse (Figure 2.1i)[18,95,105]. As anticipated, signaling pathways involved in TCR and immune response activation, as well as actin cytoskeleton organization, were enriched in TCR-control stimulated conditions compared to those treated with TCR-PD-L1 (Figure 2.1i) [9,16,95]. We also calculated the mean slope for each gene across all time points in both TCR-PD-L1-ligated and TCR-control-stimulated conditions to rank the most highly enriched proteins over time. SHP2 and PIEZO1 ranked highest as proteins experiencing change in slope following PD-L1 ligation compared to TCR stimulation alone, along with sorting nexins involved in intracellular trafficking (SNX12), actin polymerizing subunits (ARPC2, TFG) and membrane transporters (SLC34A1, SLC44A1) (Figure 2.1j). As expected, we identified various TCR- and CD28-related genes enriched in the TCR-control-treated samples, including CD28, CD3ζ, ZAP70, VAV3 and PI3K-related proteins (Figure 2.1j)[17]. Collectively, these data highlight the diverse membrane dynamics that occur following TCR stimulation and PD-L1 ligation in T cells, which not only confirm previous findings, but also identify the novel association of PD-1 and PIEZO1 to unveil a previously uncharacterized regulatory mechanism of PD-1-mediated inhibition involving mechanosensation.
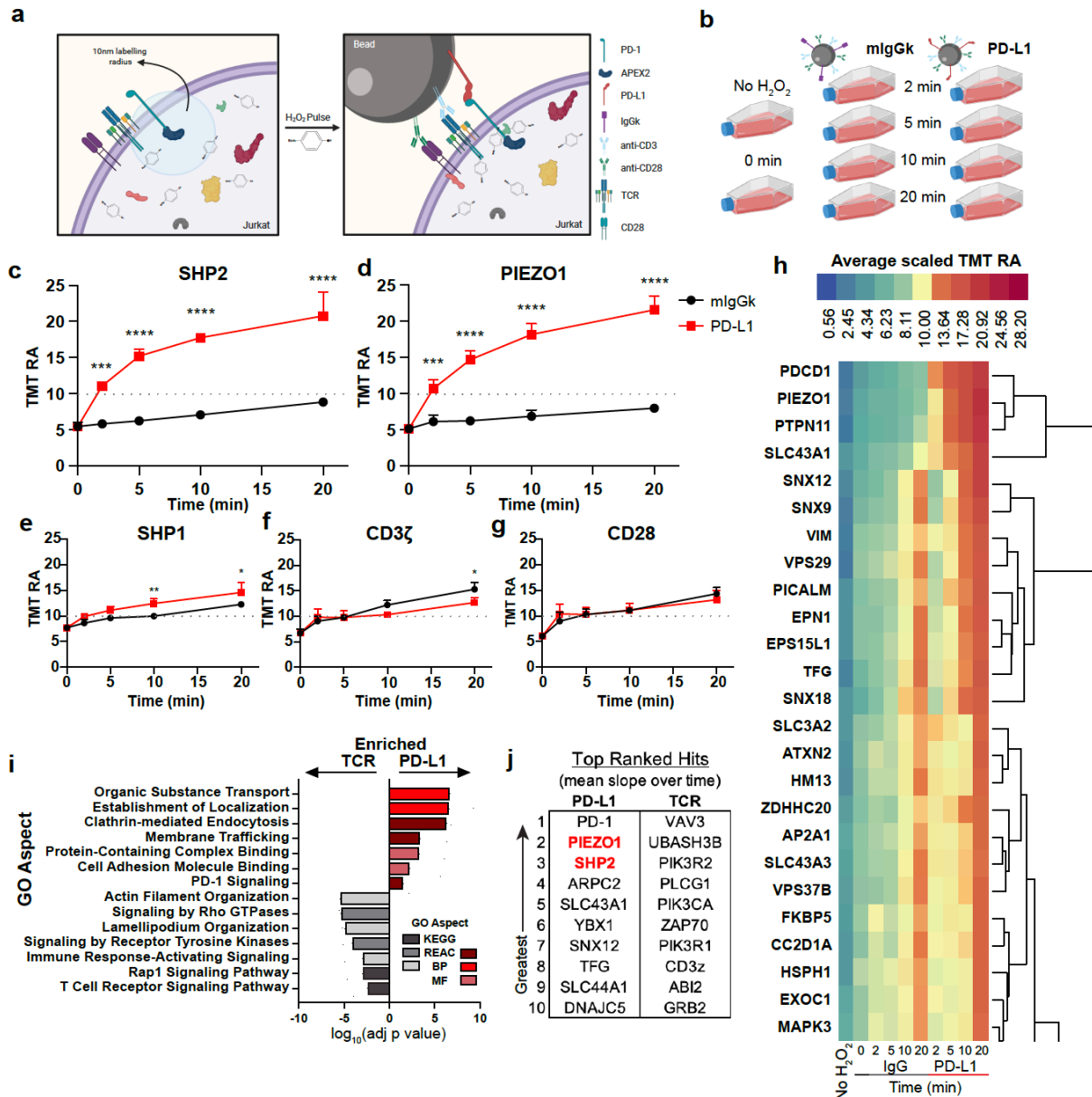
**Figure 2.1: APEX2 proximity labelling identifies PIEZO1 as PD-1 target.** a) Diagram of PD-1-APEX2 proximity labelling dynamics in Jurkat cells treated with TCR-PD-L1- and TCR-control-containing beads. b) Experimental schematic of PD-1-APEX2 proximity labelling time course with bead treatment. TMT ratios over time (min) of c) SHP2, d) PIEZO1, e) SHP1, f) CD3ζ and g) CD28 following stimulation of PD-1-APEX2 with TCR-PD-L1 or TCR-control beads. Data are presented as means from three independent experiments ± SD. Statistical significance was assessed using two-way ANOVA analysis comparing TCR-PD-L1 and TCR-control bead-treated groups. Only significant differences are indicated. * $p<0.05$, ** $p<0.01$, *** $p<0.001$, **** $p<0.0001$. h) Hierarchical one-way clustering of the averaged TMT ratios from the top 25 proteins calculated from three independent experiments. i) Log-adjusted p-values of significantly enriched GO Terms in TCR-PD-L1 or TCR-control conditions identified from three independent experiments and calculated from fold changes comparing TCR-PD-L1 and TCR-control mean slope over time. The top 50 genes were selected for analysis using gProfiler. j) Rank list of the top ten genes identified in TCR-PD-L1 or TCR-control conditions calculated from the mean slope of three independent experiments. Schematics created using BioRender.

18

*PIEZO1 co-immunoprecipitation and trigger peptide analysis*

Since proximity labelling identifies protein associations within a 10nm radius of the APEX2 probe, we sought to determine if PD-1 and PIEZO1 directly interacted following PD-1 ligation. We performed a co-immunoprecipitation (co-IP) of PIEZO1 in PD-1-expressing Jurkat cells to assess direct binders of PIEZO1 following 20 min stimulation with TCR-PD-L1 or TCR-control beads. Two-way hierarchical clustering highlighted distinct differences among TCR-control, TCR-PD-L1, no bead-treated and negative control groups (Figure 2.S5a). We used trigger peptide analysis to identify specific PD-1 and PIEZO1 interaction[106]. The synthetic isotope-labelled peptide LAAFPDER, which maps uniquely to PD-1, was used for triggered quantification of PD-1 in PIEZO1 pulldowns (Figure 2.S5b)[106]. We found that PD-1 was significantly enriched in TCR-PD-L1-treated conditions compared to TCR-control conditions, reaffirming PD-1 and PIEZO1 colocalization following PD-1 ligation (Figure 2.S5b). However, the limited number of observed events suggests that this interaction is likely transient or indirect. For this reason, it is possible that PD-1 mediators regulate cytoskeletal machinery that alter PIEZO1 activation[18,84].

We also assessed significantly enriched proteins associating with PIEZO1 upon PD-1 ligation to determine if specific binding events were induced by PD-1-mediated inhibition. Interestingly, we identified an enrichment of Nedd4-like HECT E3-ligases WWP1 and WWP2 following PD-L1 ligation, suggesting that PD-1-mediated inhibition may induce the proteasomal degradation of PIEZO1 (Figure 2.S5c-e)[107,108]. Additionally, IP of PIEZO1 identified a significant enrichment of RICTOR, a subunit the mTORC2 complex, which phosphorylates AKT and modifies the actin cytoskeleton, in TCR-PD-L1-ligated conditions compared to TCR-control conditions (Figure 2.S5f)[109,110]. These findings may link PD-1-mediated PI3K/AKT inhibition to PIEZO1 function through the non-canonical AKT-mTORC2 pathway. Moreover, we also found an enrichment of CD28 peptides in PD-L1-treated conditions compared to TCR-treated controls. CD28 is a reported PD-1 target that activates the PI3K/AKT pathway as well as cytoskeleton organization upon TCR stimulation and may promote PIEZO1 activity (Figure 2.S5g) [5,16,111]. These data suggest that PD-1 regulates PIEZO1 inhibition and proteasomal degradation, while T cell signaling cascades and cytoskeletal rearrangements driven, in part, by CD28 activate PIEZO1 to promote optimal T cell function.

*PIEZO1 activation drives $Ca^{2+}$-mediated T cell signaling*

Recent studies demonstrate that PIEZO1-driven $Ca^{2+}$ influx in T cells leads to calpain activation and reorganization of cortical F-actin scaffolding, linking PIEZO1 to optimal TCR signaling[90]. PD-1 ligation has been shown to impair F-actin clearing from the cellular interface, reduce $Ca^{2+}$ signaling and abrogate tumor cell killing[18]. Given these opposing functions of PD-1 and PIEZO1, we hypothesized that PD-1 may associate with PIEZO1 to impair optimal TCR signaling and T cell function. To determine the functional relevance of PD-1 and PIEZO1 association, we analyzed PIEZO1 function in CD8+ T cells. We first examined $Ca^{2+}$ flux by staining primary WT murine CD8+ T cells with Fluo-4. As anticipated, treatment of these CD8+ T cells with PIEZO1 agonist Yoda1 resulted in an increase in $Ca^{2+}$ influx over time, while administration of PIEZO1 antagonist GsMTx4 attenuated $Ca^{2+}$ influx, illustrating that indeed PIEZO1 regulates $Ca^{2+}$ influx in CD8+ T cells (Figure 2.S6a-b)[88,112,113]. Co-culture of TCR-PD-L1 beads with CD8+ T cells also showed a decrease in $Ca^{2+}$ signaling, similar to the decrease observed in cells treated with GsMTx4 alone (Figure 2.S6a-b). Treating CD8+ T cells with TCR-PD-L1 beads in the presence of Yoda1 resulted in increased $Ca^{2+}$ influx, suggesting that Yoda1 agonism can override inhibition of $Ca^{2+}$ influx governed by PD-1 ligation (Figure 2.S6a-b). These data suggest that PIEZO1 gating contributes significantly to the influx of $Ca^{2+}$ that regulates subsequent downstream signaling in CD8+ T cells.

We also assessed levels of phosphorylated proteins in common T cell signaling pathways following PIEZO1 modulation using phospho-flow cytometry[3]. We found increased phosphorylated ERK (pERK) levels upon PIEZO1-agonism and decreased pERK levels upon PIEZO1-antagonism, which correlate with reports characterizing ERK activation through $Ca^{2+}$ signaling in T cells (Figure 2.S6c)[114]. These findings were reproducible using Western blotting analysis (Figure 2.S6d). We did not observe significant alterations in the canonical AKT/mTORC1/S6 pathway at early timepoints driven by PIEZO1 agonism or antagonism, further supporting that $Ca^{2+}$-sensitive T cell signaling pathways are affected by PIEZO1 modulation (Figure 2.S6e-f). Phosphorylation of AKT by TCR- and CD28-mediated signal transduction may induce cytoskeletal rearrangements that activate PIEZO1, as described above, rather than PIEZO1-mediated $Ca^{2+}$ influx stimulating AKT signaling.

While our studies focus on PIEZO1 gating through internal cytoskeletal forces, various reports have verified PIEZO1 regulation through outside-in forces, including shear stress, cyclical pressure and membrane deformation[65,68,73,74,76,87,88,101,115]. Specifically, recent studies have demonstrated that alveolar macrophages are capable of cyclical pressure sensing[73]. Since CD8^{+} T cell intravasation from blood cells and migration to various tissues exposes them to similar external forces, we next asked if cyclical hydrostatic pressure could activate PIEZO1 and regulate downstream signaling pathways similar to PIEZO1 agonism and TCR stimulation[59]. CD8^{+} T cells activated with plate-coated CD3/CD28 crosslinking antibodies for 48 h and rested in culture media were exposed to pulses of 40-60mmHg of cyclical hydrostatic pressure for 20 min using previously described methods[73]. Cells were immediately fixed and stained for phospho-flow cytometric analysis. Interestingly, our preliminary studies showed external pressure indeed increased the signaling capabilities of CD8^{+} T cells in ERK, PLC$\gamma$ and S6 pathways based on mean fluorescence intensity (MFI) (Figure 2.S6g-i). While it is possible that additional mechanosensors may play a role in CD8^{+} T cell function, it is likely that PIEZO1 activity contributes to increases in CD8^{+} T cell signaling induced by cyclical pressure sensing, given the activation of similar pathways using PIEZO1 agonist Yoda1 observed in phospho-flow cytometry analysis (Figure 2.S6c-d). Further studies with appropriate controls are necessary for exploring outside-in mechanics on T cells to determine how external forces may regulate T cell biology, as addressed in Chapter 2.3 and Chapter 4.3.

*PD-1 ligation inhibits PIEZO1-mediated Ca$^{2+}$ influx*

Upon TCR stimulation, there is a tightly regulated response to Ca$^{2+}$ influx, with Ca$^{2+}$ release-activate Ca$^{2+}$ (CRAC) channels and voltage gated Ca$^{2+}$ channels being necessary for the TCR signaling cascade[6,114,116–118]. The involvement of multiple Ca$^{2+}$ channels makes it difficult to uncouple their contributions during T cell activation. For this reason, we generated a Jurkat cell line stably expressing an inducible, fluorescent PIEZO1 activity reporter (XLGenEPi) to investigate the role of PIEZO1 in T cell signaling as well as the potential regulation of PIEZO1 by PD-1[119]. The XLGenEPi reporter is expressed using a Tet-On doxycycline system and is comprised of GCaMP, a genetically encoded Ca$^{2+}$ indicator fused to the cytoplasmic tail of PIEZO1 to specifically sense Ca$^{2+}$ influx regulated by PIEZO1[119] (Figure 2.2a and Figure 2.S7a). XLGenEPi

Jurkat cells demonstrated increasing levels of PIEZO1 activity with a dose titration of doxycycline in the presence of Yoda1, ensuring the inducibility of the XLGenEpi construct (Figure 2.S7b).

To assess changes in PIEZO1 activity following PD-1 ligation, we treated PD-1-expressing XLGenEpi Jurkat cells with TCR-control or TCR-PD-L1 beads. We observed a sustained increase in PIEZO1 activity indicated by frequency and mean fluorescence intensity (MFI) of GFP-positive cells following 20 min treatment with TCR-control beads compared to TCR-PD-L1 bead-treated conditions (Figure 2.2b-d). Yoda1 treatment also induced PIEZO1 activity similar to TCR stimulation (Figure 2.2b) but resolved over 30 s, while TCR stimulation maintained PIEZO1 activity at 30 s (Figure 2.2c). These data confirm PD-1-mediated inhibition of PIEZO1 activity using flow cytometry and suggest more prolonged PIEZO1-mediated $Ca^{2+}$ influx following TCR stimulation that may be regulated by persistent actinomyosin contractile forces at the immune synapse[65,90,94,120,121].

To visualize and compare changes in PIEZO1 activity and PD-1 co-localization with PIEZO1 in the presence or absence of PD-1 ligation, PD-1-expressing XLGenEPi Jurkat cells were passed through a flow-cell chamber coated with crosslinking CD3 and CD28 antibodies and either PD-L1 or control $mIgG_{1κ}$ ligand. Using total internal reflection fluorescence (TIRF) time lapse imaging, we found that XLGenEPi Jurkat cells exhibited strong PIEZO1 activity at the ligand-cell interface following 100 s of TCR stimulation that persisted over time for 10 min (600 s), further confirming that TCR stimulation induces PIEZO1 activity (Figure 2.2e). This activity coincided with F-actin ring formation, where PIEZO1 activity appeared to localize around F-actin ring structures and was not inhibited by PD-1 receptor clustering, suggesting that F-actin ring formation at the immune synapse drives PIEZO1 activity (Figure 2.2e)[84,95]. PIEZO1 localization around polymerizing F-actin rings that contract inward may supply enough force to gate PIEZO1 in an open conformation to sustain $Ca^{2+}$ influx for optimal TCR signaling[94,95,121]. We observed a striking decrease PIEZO1 activity over time in the presence of PD-L1 (Figure 2.2f). Cells exposed to anti-CD3/CD28 and PD-L1 ligand began fluorescing at 220 s with less robust activity that remained dim over time compared to TCR-treated conditions (Figure 2.2e-f). Moreover, PIEZO1 activity strongly colocalized with PD-1 receptor clustering at the F-actin ring for 10 min (600 s), implying that PD-1 ligation results in the attenuation of

PIEZO1 activity through association (Figure 2.2f). These data suggest that TCR-induced cytoskeletal rearrangements provide sufficient force to gate PIEZO1 at the immune synapse and this activity is inhibited by PD-1 ligation.

**a**

Extracellular space

Agonism or mechanical stimulus

Cytosol

GCaMP

>1uM

**b**  10 s acquisition

%PIEZO1 Reporter Activity

RPMI (+Ca 2+) | Yoda1 (5uM) | TCR | PD-L1

**c**  30 s acquisition

%PIEZO1 Reporter Activity

RPMI (+Ca 2+) | Yoda1 (5uM) | TCR | PD-L1

**d**  PIEZO1 Reporter MFI

MFI PIEZO1 Reporter Activity

PBS (-Ca 2+) | RPMI (+Ca 2+) | Yoda1 (5uM) | TCR | PD-L1

**e**

Time (s):    0    100    220    340    460    580

anti-CD3/CD28 + mIgGk

PIEZO1 Activity

PD-1

F-Actin

Merge

**f**

Time (s):    0    100    220    340    460    580

anti-CD3/CD28 + PD-L1

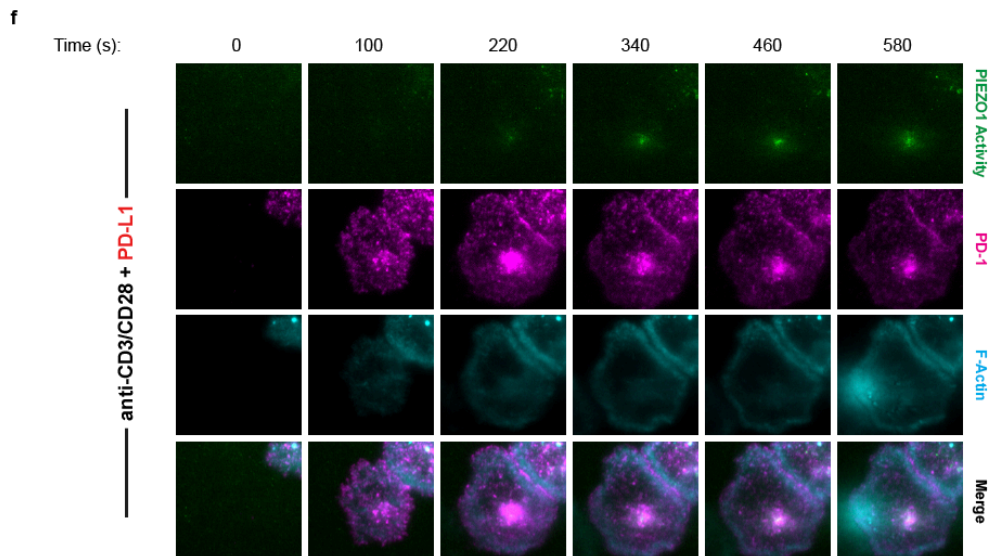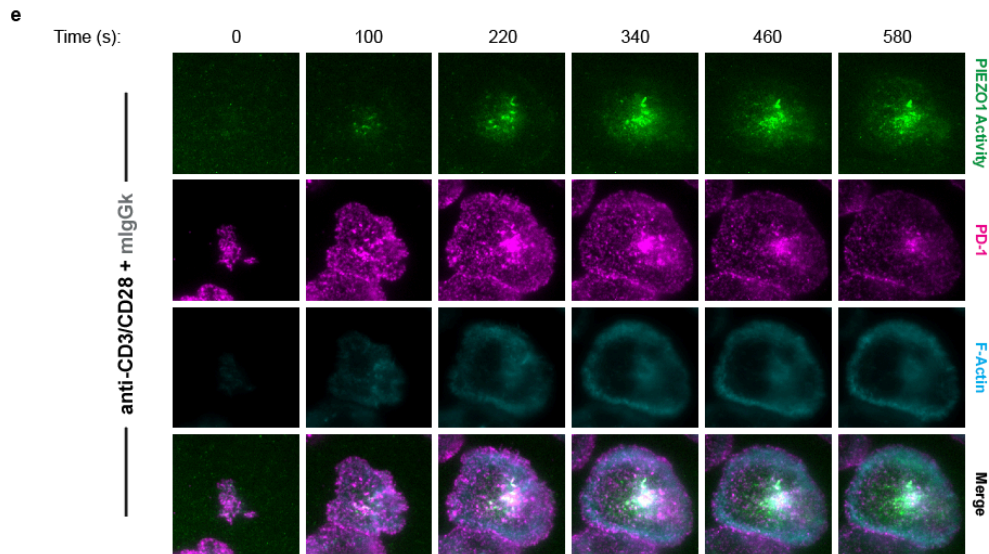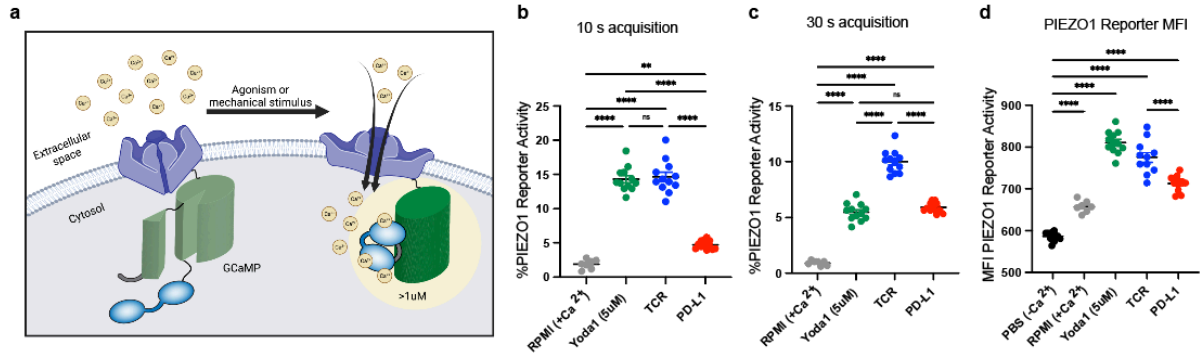PIEZO1 Activity

PD-1

F-Actin

Merge

24

**Figure 2.2: PD-1 inhibits TCR-induced PIEZO1 activity around F-actin rings.** a) Schematic of GFP fluorescence induced by PIEZO1-specific $Ca^{2+}$ reporter XLGenEPi. Flow cytometric analysis of PIEZO1 reporter activity in PD-1-expressing XLGenEPi Jurkats treated with RPMI media, Yoda1 (5μm), TCR-control or TCR-PDL1 beads for b) 10 s and c) 30 s acquisition. d) MFI of XLGenEPi reporter in all conditions following 30 s acquisition. Cells were treated with beads 20 min prior to acquisition and with Yoda1 (5μM) immediately prior to acquisition. Data are presented as means of n=7-12 technical replicates ± SD. Statistical significance was assessed using one-way ANOVA analysis. ns, * p<0.05, ** p<0.01, *** p<0.001, **** p<0.0001. Representative images of XLGenEPi Jurkat (AF488) cells stained with PD-1 (AF647) and F-actin dye (SPY555) and flown through flow cell chambers coated with anti-CD3/CD28 crosslinking antibodies and e) control mIgG$_1$κ ligand or f) PD-L1 to assess PIEZO1 activity. Schematic created using BioRender.

*CD8$^+$ T cell-specific PIEZO1 KO impairs antitumor immunity*

To selectively investigate PD-1 and PIEZO1 function in CD8$^+$ T cells, we developed a tamoxifen-inducible CD8$^+$-specific PIEZO1 KO mouse by crossing *Piezo1$^{flx/flx}$* mice with E8i-Cre-ER$^{T2}$ Rosa26 TD Tomato reporter mice (Figure 2.S8a). Following tamoxifen treatment, we observed ~70% deletion efficiency of PIEZO1 in Cre+ CD8$^+$ T cells compared to Cre- controls, as assessed by RT-qPCR using probes specific for the loxP regions flanking exons 20-23 of PIEZO1 (Figure 2.S8b). Functionally, we observed a significant decrease in PIEZO-1-specific $Ca^{2+}$ influx induced by Yoda1 treatment and visualized with Indo-1 in Cre+ CD8$^+$ T cells compared to Cre- CD8$^+$ T cells following tamoxifen treatment (Figure 2.S8c). In addition, Cre expression indicated by eGFP was only detectable on CD8$^+$ T cells as assessed by flow cytometry compared to CD4$^+$, B cell and myeloid cell subsets, and expression levels were comparable to knockout efficiency as assessed by RT-qPCR (Figure 2.S8b, d-e). *In vitro* stimulation of tamoxifen-treated Cre+ and Cre- E8i-Cre-ER$^{T2}$ *Piezo1$^{flx/flx}$* CD8$^+$ T cells with a titration of crosslinking CD3 and CD28 antibodies showed slight decreases in viability, CD44, granzyme B, and IFNγ/TNFα-double expression, as well as increased expression of CD62L at higher CD3/CD28 stimulation concentrations (Figure 2.S9a,d,e-f,h), suggesting that PIEZO1 KO impairs activation and effector function. We did not observe significant differences in PD-1, CTLA4 and Ki-67 expression or IL-2, IFNγ and TNFα cytokine production between the two groups (Figure 2.S9b-c,f,g,i-k).

Given the increase in CD8$^+$ TIL function observed with PIEZO1 agonism, we hypothesized that loss of PIEZO1 in CD8$^+$ T cells would lead to more rapid tumor growth. Indeed, when tamoxifen-treated E8i-Cre-ER$^{T2}$ *Piezo1$^{flx/flx}$* mice were implanted with MC38 or B16-OVA tumor cells and monitored for tumor growth,

we found loss of PIEZO1 on CD8$^+$ T cells alone was sufficient to drive significantly increased tumor burden in Cre+ mice compared to Cre- controls in both models (Figure 2.3a-c). We observed a significant decrease in CD8$^+$ T cell frequencies in both tumor models (Figure 2.3d,g). In addition, we found an increase in total CD4$^+$ T cell frequencies and lower CD8$^+$/CD4$^+$ T cell ratios in the tumor with no significant changes in CD3$\varepsilon$ frequencies in either model (Figure 2.S10 a-f). We next assessed expression of activation markers and found Cre+ CD8$^+$ TILs from MC38 tumors expressed significantly more CD62L and significantly less PD-1, CTLA4 and CD69 compared to Cre- controls (Figure 2.3e and Figure 2.S10g-i). Cre+ CD8$^+$ TILs from B16-OVA tumors also expressed significantly more CD62L and significantly less CTLA4 and CD69 compared to Cre- controls, but did not show significant differences in PD-1 frequency though it trended similarly (Figure 2.3h and Figure 2.S10j-l). We also examined CD8$^+$ TIL cytotoxicity found that Cre+ CD8$^+$ TILs from B16-OVA tumors expressed significantly less granzyme, while CD8$^+$ TILs from MC38 tumors also expressed less granzyme B, but this trend was not significant (Figure 2.10m, p). Interestingly, PIEZO1 KO CD8$^+$ TILs from MC38 and B16-OVA models consistently retained high expression of Slamf6 and had minimal expression of TIM-3 (Figure 2.3f,i, Figure 2.S10n-o, q-r). These findings suggest that PIEZO1 plays a role in regulating the transitioning of Slamf6 progenitor cells to TIM-3 effector-like CD8$^+$ TILs and regulates exhausted CD8$^+$ T cell subpopulations[122–124]. Assessment of Cre reporters in CD8$^+$ splenocytes on day 15 following tumor implantation showed sustained Cre activity in Cre+ CD8$^+$ T cells, confirming the efficacy of our inducible Cre system (Figure 2.S11a-b). Together, these data indicate that loss of PIEZO1 activity in CD8$^+$ T cells decreases activation and acquisition of effector functions to impair antitumor immunity and promote tumor growth, similar to PD-1-mediated inhibition of T cell activation.

To further investigate PD-1 regulation of PIEZO1, we treated E8i-Cre-ER$^{T2}$ *Piezo1$^{flx/flx}$* Cre+ and Cre- tumor-bearing mice with anti-PD-1 or isotype control (Figure 2.3j). Strikingly, administration of anti-PD-1 blocking mAb on days 14 and 17 did not fully clear or reduce growth of MC38 tumors, which are highly sensitive to PD-1 blockade, in E8i-Cre-ER$^{T2}$ *Piezo1$^{flx/flx}$* Cre+ mice compared to Cre- controls (Figure 2.3k, Figure 2.S12a). Similarly, administration of anti-PD-1 blocking mAb on days 10 and 13 following tumor implantation did not significantly reduce tumor growth in E8i-Cre-ER$^{T2}$ *Piezo1$^{flx/flx}$* Cre+ mice bearing B16-OVA tumors compared to Cre- controls (Figure 2.3l, Figure 2.S12b). PIEZO1 KO in CD8$^+$ T cells significantly impaired

overall survival in both tumor models regardless of PD-1 blockade (Figure 2.4m-n). These data demonstrate that PD-1-mediated inhibition of PIEZO1 in CD8^{+} T cells contributes to immune evasion by tumors and underscore the significance of mechanical force in shaping T cell responses.
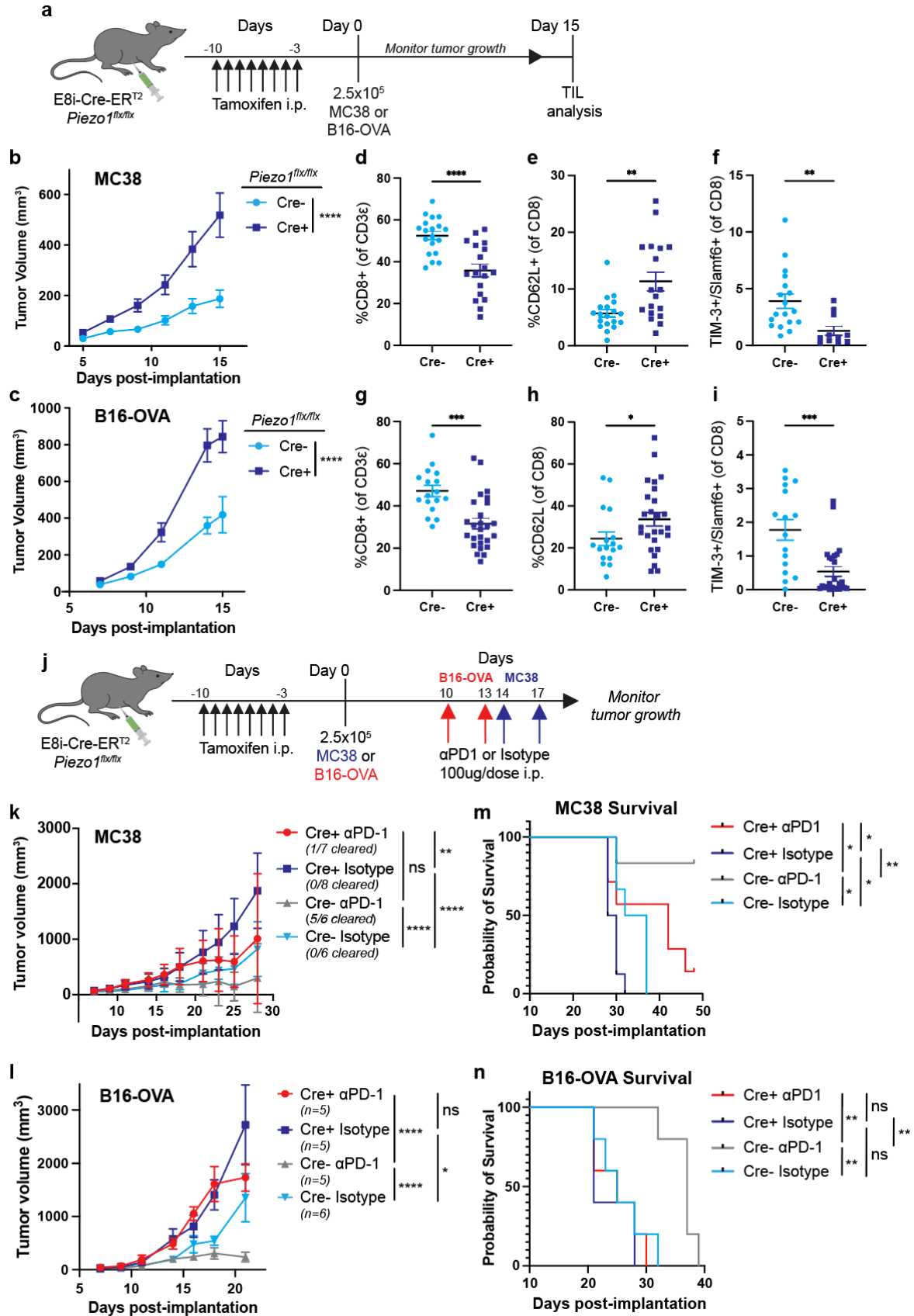
**Figure 2.3: PIEZO1 activity in CD8^{+} T cells regulates antitumor immunity.** a) Schematic of E8i-Cre-ER[T2] *Piezo1[flx/flx]* tumor growth experiment and TIL analysis. Tumor volume ($mm^3$) measured over time (days) for b) MC38 tumors and c) B16-OVA tumors in Cre+ and Cre- E8i-Cre-ER[T2] *Piezo1[flx/flx]* mice. Data are presented as means of n=10-11 for MC38 and n=12-18 for B16-OVA ± SD from two independent experiments for each tumor type including male and female mice. Frequencies of d,g) CD8^{+} TILs and e,h) CD62L frequencies on CD8^{+} TILs isolated from MC38 and B16-OVA tumors on day 15 post-implantation. Ratio of f,l) TIM-3/Slamf6 frequencies on CD8^{+} TILs. Data are presented as means of n=18-26 from three independent experiments ± SD. Statistical significance was measured using Student's unpaired t-test. * $p<0.05$, ** $p<0.01$, *** $p<0.001$, **** $p<0.0001$. Non-parametric t tests were used for graphs that did not exhibit Gaussian distribution. j) Schematic of tumor growth experiment with PD-1 blockade dosing. Tumor volume ($mm^3$) measured over time (days) for k) MC38 and l) B16-OVA tumors in Cre+ and Cre- E8i-Cre-ER[T2] *Piezo1[flx/flx]* mice with corresponding m) MC38 and n) B16-OVA survival analysis. Data are presented as means of n=5-8 ± SD from one experiment for each tumor type. Statistical significance for tumor growth curves was calculated using two-way ANOVA. * $p<0.05$, ** $p<0.01$, *** $p<0.001$, **** $p<0.0001$. Statistical significance of survival curves was measured using Log-rank Mantel Cox test. * $p<0.0332$, ** $p<0.0021$, *** $p<0.002$.

*PIEZO1 KO CD8^{+} TILs are less cytotoxic*

To further assess the mechanisms by which PIEZO1 KO CD8^{+} T cells have impaired antitumor responses, we sorted PIEZO1 KO and WT CD8^{+} TILs at day 15 following implantation of B16-OVA tumors for proteomic analysis. In alignment with our flow cytometry analysis, we found that perforin and granzyme B in addition to other granzymes (granzyme C, D and E), as well as multiple serpin molecules (serpin 6b, 9b) were significantly underrepresented in PIEZO1 KO CD8^{+} TILs compared to WT (Figure 2.S12). Studies have demonstrated the significance of mechanosensation in promoting cytotoxic granule formation and release from CD8^{+} T cells[98,99]. Additionally, Serpin9b has been shown to regulate granzyme B levels in the cytosol[125]. Therefore, our data suggest that the mechanisms driving cytotoxic granule formation, regulation and release may be impaired in PIEZO1 KO CD8^{+} TILs and emphasize that PIEZO1-mediated mechanosensing is required for acquisition of optimal CD8^{+} T cell effector functions[125].

*PIEZO1 agonism improves CD8^{+} T cell antitumor immunity*

Our observed increases in CD8^{+} T cell signaling following *in vitro* PIEZO1 agonism led us to ask whether PIEZO1 activation would enhance antitumor immunity, in contrast to the reduced antitumor immunity seen in CD8^{+}-specific PIEZO1 KO mice. To investigate this question, we implanted MC38 tumors subcutaneously in WT mice and administered Yoda1 (7.5mg/kg) intraperitoneally (i.p.) (Figure 2.4a). While Yoda1 did not consistently lessen tumor burden in WT mice (Figure 2.S14a-b), phenotypic analysis of the immune compartment at day 15 following MC38 tumor implantation revealed increased percentages of CD8^{+} TILs

in Yoda1-treated mice compared to controls (Figure 2.4b). Additionally, Yoda1-treated CD8^{+} TILs expressed more activation and effector molecules, including PD-1, granzyme B and perforin and lower expression of CD62L (Figure 2.4c-f). Interestingly, PIEZO1-agonized CD8^{+} TILs expressed high levels of exhaustion marker TIM-3 and low levels of progenitor stem-like marker Slamf6 compared to controls, again suggesting a role for PIEZO1 in driving an effector-exhausted phenotype (Figure 2.4g and Figure 2S14c-d)[122–124].

Studies have shown that PIEZO1 increases myeloid cell suppressive function in the TME and plays a role in the expansion of FoxP3+ T regulatory (Treg) cells during experimental autoimmune encephalomyelitis (EAE) infection[74,91]. While frequencies of Treg and T conventional (Tcon) cells recovered from the tumor were not significantly different, we found that Yoda1-treated Treg cells expressed more perforin and Tcon cells expressed less perforin compared to control mice indicating that PIEZO1-agonized Treg cells may be more suppressive (Figure 2.S12e-h). We also assessed T cell numbers in the draining lymph node and found that CD8^{+} T cells and Tcon cell numbers were increased and Treg cell numbers were significantly increased (Figure 2.S12i-k). These alterations to Treg cell frequency and cytotoxicity in addition to reported PIEZO1-mediated suppressive functions in myeloid cells likely contribute to the lack of effect of Yoda1 on tumor growth despite observing more cytotoxic and effector-like CD8^{+} TILs. Furthermore, our studies did not show a significant effect on viability or alterations in AKT and ERK signaling in MC38 or B16-OVA tumor cells driven by PIEZO1 agonism, further implicating PIEZO1-mediated effects on the immune compartment (Figure 2.S15a-d). Our evidence strongly suggests that PIEZO1 agonism increases CD8^{+} TIL function and more targeted therapy could perhaps unleash this function for antitumor immunity.
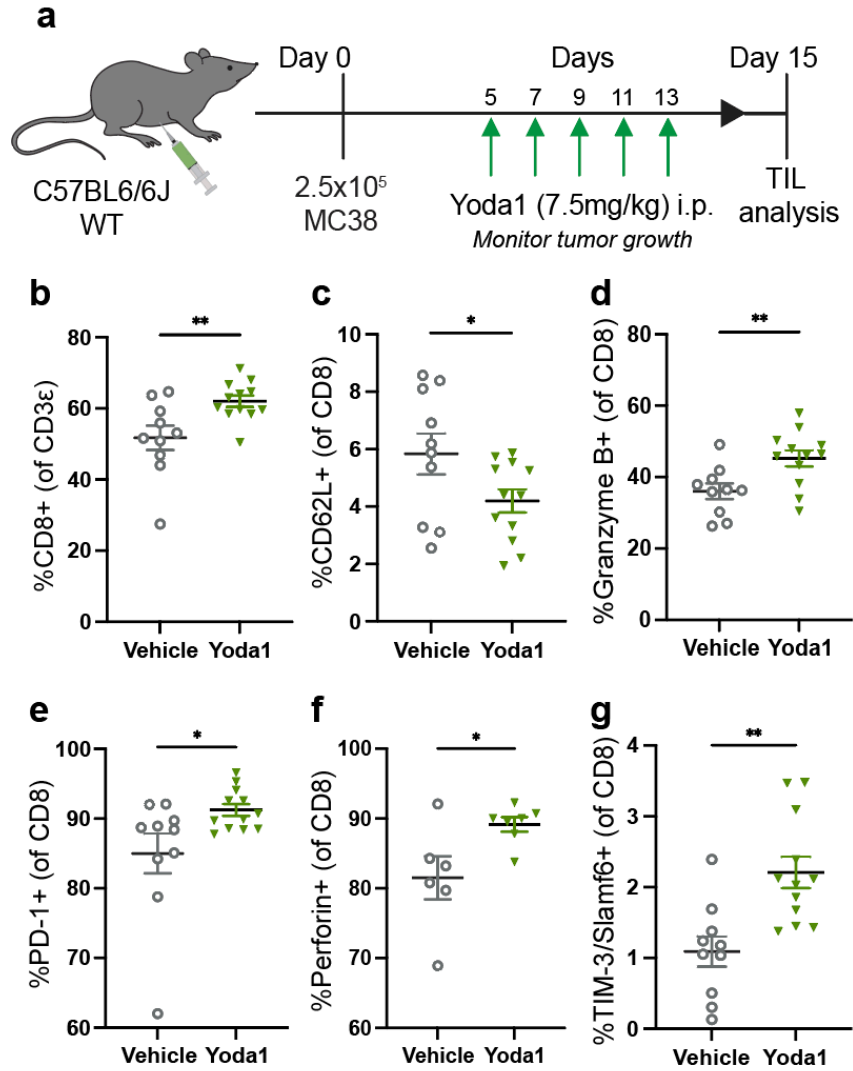
**Figure 2.4: PIEZO1 agonism improves CD8+ TIL function.** a) Schematic of Yoda1 treatment in MC38 tumor bearing WT mice. Frequencies of b) CD8+ T cells, c) CD62L, d) granzyme B, e) PD-1, f) perforin and g) TIM-3/Slamf6 assessed by flow cytometry. Data are presented as means of n=6-12 ± SD from one or two independent experiments. Statistical significance was measured using Student's unpaired t-test. * p<0.05, ** p<0.01, *** p<0.001, **** p<0.0001.

*Therapeutic effect of combined PD-1 blockade and PIEZO1 agonism*

We next asked if the increased CD8⁺ T cell effector function observed in PIEZO1-agonized CD8⁺ TILs would improve the efficacy of PD-1 blockade. To assess the effects of combination treatment with PIEZO1 agonist Yoda1, we chose the B16.F10 tumor model because it is unresponsive to PD-1 blockade (Figure 2.5h-i)[126]. Mice treated with either PD-1 blockade or Yoda1 alone did not show decreased tumor burden. In marked contrast, we observed a significant attenuation in tumor growth when PD-1 blockade and Yoda1 were administered together (Figure 2.5i/k). Moreover, anti-PD-1 and Yoda1 combination treatment significantly improved survival in B16.F10 tumor-bearing mice compared to single and negative controls. These data highlight a potential role for CD8⁺-specific PIEZO1 agonism as an adjuvant for PD-1 therapy in checkpoint blockade-resistant cancers.
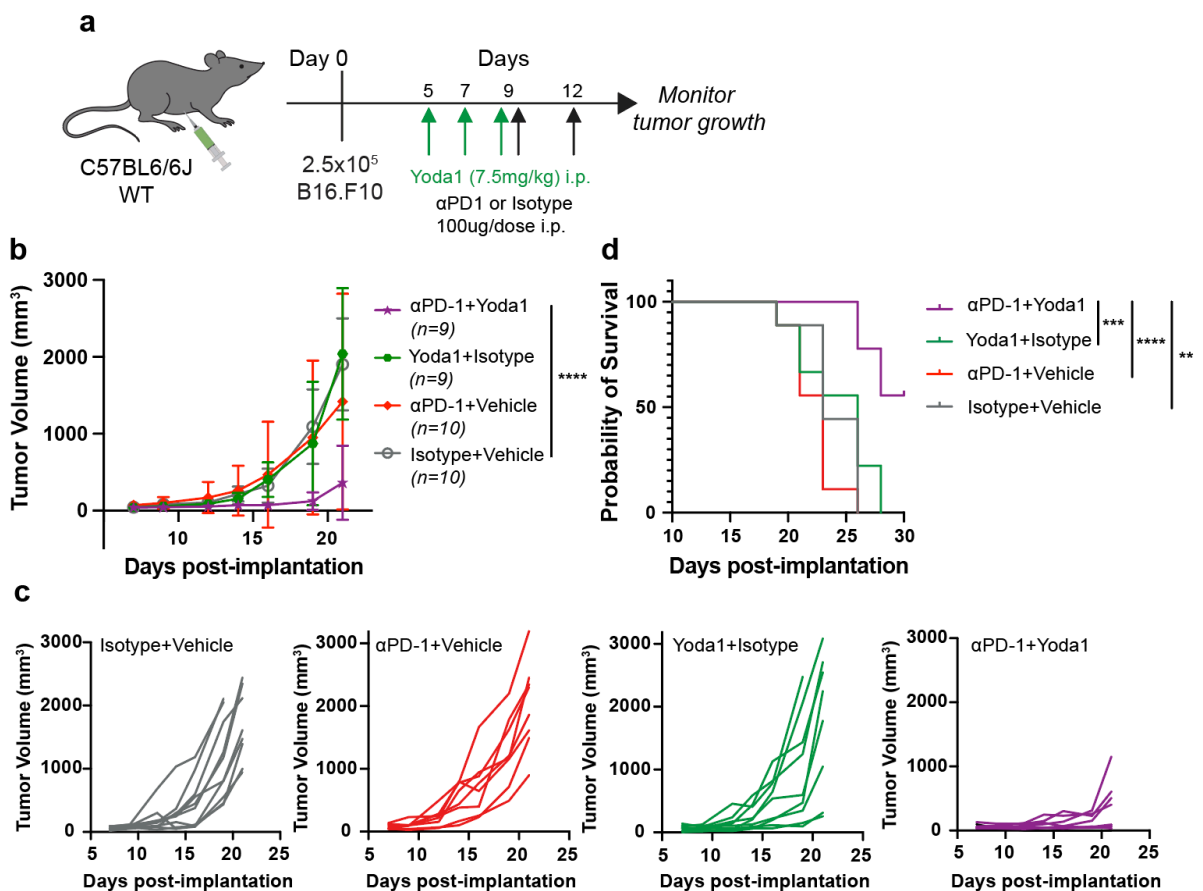
**Figure 2.5: Therapeutic efficacy of PD-1 blockade and PIEZO1 agonism.** a) Schematic of PD-1 blockade and Yoda1 combination dosing in B16.F10 tumor-bearing mice. b) Tumor volume ($mm^3$) measured over time (days) and c) individual tumor growth curves from data depicted in b). d) Corresponding survival analysis. Data are combined from two independent experiments and are presented as means of n=9-10. Statistical significance of tumor growth was measured using 3-way ANOVA. * p<0.05, ** p<0.01, *** p<0.001, **** p<0.0001. Statistical significance of survival curves was measured using Log-rank Mantel Cox test. * p<0.0332, ** p<0.0021, *** p<0.002.

## 2.3 Discussion

PD-1 signaling in T cells counters an elaborate activation program. However, our understanding of the signaling mechanisms by which PD-1 exerts its inhibitory functions is incomplete. Here we identify a novel regulatory function of PD-1 in constraining T cell signals driven by mechanical forces. Specifically, we have shown that PD-1 associates with PIEZO1 at the immunological synapse following PD-1 ligation. This association impairs PIEZO1 activation and subsequent $Ca^{2+}$-mediated signaling that drives T cell activation, acquisition of effector functions and cell fate decisions during cancer pathogenesis. Genetic loss of PIEZO1 in CD8^{+} T cells alone is sufficient to attenuate CD8^{+} TIL-mediated tumor control that cannot be overcome by PD-1 blockade. Conversely, PIEZO1-agonism improves CD8^{+} T cell activation and function in the TME and has significant therapeutic effects when combined with PD-1 blockade to control tumor growth. These findings provide new understanding of molecular changes that occur in T cells upon PD-1 ligation and suggest a role for CD8^{+}-targeted PIEZO1 agonism as a potential avenue for therapeutic intervention in cancer.

The inability of PD-1 blockade to reverse PIEZO-1 mediated tumor growth strongly suggests that PIEZO1 is a primary target of PD-1-mediated inhibition. It is likely that instability at the immune synapse resulting from PIEZO1 loss prevents proper T cell activation and initiation of the TCR signaling cascade[84,90,95,115]. This notion is supported by our studies, which highlight the necessity of PIEZO1 in promoting optimal CD8^{+} T cell function in tumor models. Loss of PIEZO1 on CD8^{+} T cells alone was sufficient to abrogate CD8^{+} TIL-mediated antitumor immunity, resulting in increased tumor growth kinetics (Figure 2.3b-c). Moreover, PIEZO1 KO CD8^{+} TILs did not efficiently traffic to the TME and were less activated and effector-like, suggesting that PIEZO1 plays an important role in T cell activation and acquisition of effector functions (Figure 2.3d-f, g-i and Figure 2.S10). Since PIEZO1 can be gated by cytoskeletal dynamics and actin

retrograde flow relies on $Ca^{2+}$ influx to stabilize the immune synapse, it is likely that loss of PIEZO1 attenuates these functions to result in impaired TCR activation[84,90,95,115,121,127].

Conversely, combining PD-1 blockade with PIEZO1 agonism improved tumor control in PD-1 blockade-unresponsive tumors (Figure 2.4i-k). We observed that PIEZO1 agonism alone improved CD8^{+} T cell infiltration in the tumor (Figure 2.4b). It is possible that administration of Yoda1 increased the number of CD8^{+} T cells in the tumor that subsequently were reinvigorated by PD-1 blockade, resulting in a bolstered immune response that more effectively controlled tumor growth. Since PIEZO1 agonism alone was not sufficient to consistently decrease tumor burden, we hypothesized that PIEZO1 agonism on various immune cell subsets promoted a more immunosuppressive environment that could not be overcome by improved CD8^{+} T cell numbers and function (Figure 2.S14a-b)[74,91]. However, the PD-1 pathway contributes to the immunosuppressive environment in the TME and PD-1 blockade has been shown to reverse this immunosuppression[4,128,129]. In this way, PD-1 blockade in combination with Yoda1 may improve cytotoxic CD8^{+} T cell responses, while also attenuating the immunosuppressive environment in the TME. Because we've demonstrated that PD-1 inhibits PIEZO1 activation, it would be worth investigating PD-1 blockade administration prior to Yoda1 administration. Thus, PD-1 ligation and subsequent inhibition of PIEZO1 would be blocked, allowing for full function of PIEZO1 activity that would be further agonized by Yoda1. Still, these results are encouraging and provide a potential avenue for treating patients that do not respond to PD-1 blockade alone.

Though we have shown a novel role for PD-1 in controlling mechanically-mediated signaling through inhibition of PIEZO1 in CD8^{+} T cells, we have yet to determine the mechanism by which PD-1 ligation results in PIEZO1 inhibition. Interestingly, co-localization of PIEZO1 with Nedd4-like HECT E3 ubiquitin ligases WWP1 and WWP2 significantly increased following PD-1 ligation, suggesting that PD-1 may induce the proteasomal degradation of PIEZO1 (Figure 2.S.5c-e). While no evidence has emerged linking PIEZO1 to WWP1 and WWP2, studies have highlighted a mechanism by which PIEZO2 is downregulated by Nedd4-2 in baroreceptor nodose ganglia neurons to induce hypertension in rats[71]. Moreover, WWP1 and WWP2 have been implicated in the regulation of various immune cell pathways[107,108,130–133]. WWP1 has been

shown to negatively regulate TGFβ signaling through the ubiquitination and degradation of Smad proteins, as well as lung Kruppel-like factor (LKLF), which maintains homeostasis in T cells[107,133]. Conversely, WWP2 targets proteins to promote cell survival, including tumor suppressor PTEN, which negatively regulates AKT signaling and zinc finger transcription factor EGR2, which regulates Fas ligand to promote activation-induced T cell death[130,132]. However, WWP2 has also been shown to promote the proteasomal degradation of TIR-domain–containing adapter-inducing interferon-β (TRIF) to impair TLR3-mediated innate immune responses[131]. Since both WWP1 and WWP2 are expressed in T cells, it is possible that these ubiquitin ligases target PIEZO1 for degradation[107]. Studying these proteins further would provide beneficial insight into the specific mechanism by which PD-1 regulates PIEZO1.

Developing a better understanding of PIEZO1 function in T cells will aid in determining the specific downstream pathways that drive the changes in PIEZO1-modulated CD8^{+} TILs. The crucial functions of CRAC channels and voltage-gated Ca$^{2+}$ channels in T cell activation raise the question of how PIEZO1-mediated Ca$^{2+}$ signaling contributes to T cell function[114,117,118,127]. It is likely that PIEZO1-specific Ca$^{2+}$ microdomains induce unique signaling outcomes in T cells[134]. We believe PIEZO1 gating is regulated by retrograde actin flow at the immune synapse, while other Ca$^{2+}$ channels drive TCR signal transduction through PLCγ[65,94,117,120,121]. Previous reports have demonstrated that PIEZO1-mediated activation of calpain proteases alters F-actin content, which aligns with our findings of PIEZO1 localizing around F-actin rings at the immune synapse[65,90,120]. Moreover, Ca$^{2+}$-mediated calpain activation in T cells has been reported to cleave cytoskeletal tethers binding LFA-1 to allow these integrins to cluster at the immune synapse for optimal signaling[115,135,136]. This particular study found that CRAC channel ORAI1 was not necessary for LFA-1 clustering and suggested the involvement of a mechanosensor, supporting the concept that PIEZO1 may provide the Ca$^{2+}$ influx necessary to regulate these membrane dynamics[135]. Interestingly, our proximity labelling experiments illustrated a significant association of PD-1 with proteins involved in membrane trafficking and endocytosis (Figure 2.1h-j). These findings, along with those discussed in Chapter 3, introduce an additional mechanism by which PD-1 inhibits PIEZO1. PD-1 sequestration of actin cytoskeletal regulatory proteins and proteins that mediate membrane turnover may play a role in impairing actin cytoskeletal dynamics and stability at the immune synapse, thereby attenuating actinomyosin contractile

forces that activate PIEZO1 (Figure 3.3, Chapter 3.4 and Chapter 4.2). Furthermore, PD-1 ligation has been shown to impair cell couplings between CD8^{+} T cells and tumor cells, potentially through inhibition of PIEZO1[18]. Together, our findings suggest that PD-1 ligation not only plays a role in inactivating PIEZO1, but also degrading it.

Additionally, it is unclear how $Ca^{2+}$ influx is sustained over a period of hours to induce specific gene transcriptional machinery following CRAC channel activation[121,127]. Previous studies have alluded to the existence of a positive feedback loop between F-actin polymerization and $Ca^{2+}$, which persists on the order of hours at the immune synapse to maintain TCR signaling[127]. It is likely that persistent actinomyosin contractile forces modulate PIEZO1 to sustain $Ca^{2+}$ influx that leads to transcription of T cell effector genes[95,121,127]. Interestingly, calpain proteases have been reported to degrade $\beta$-catenin in response to $Ca^{2+}$ influx[137–139]. Since $\beta$-catenin is a co-activator for TCF1 and TCF1-target gene expression, including Slamf6, it is possible that PIEZO1-mediated $Ca^{2+}$ influx activates calpain proteases to degrade B-catenin and thereby prevents TCF1 from transcribing target genes that maintain a stem-like progenitor pool of exhausted CD8^{+} T cells, resulting in transition of CD8^{+} T cells to TIM-3+ exhausted subpopulations[140,141]. We observed an enriched Slamf6-expressing progenitor pool in PIEZO1 KO CD8^{+} TILs and an increase in TIM-3-expressing effector-exhausted CD8^{+} TILs in PIEZO1-agonized mice, consistent with this hypothesis. PD-1 maintains the Slamf6-expressing progenitor exhausted CD8^{+} pool in chronic viral infection and our data suggest that PD-1 may inhibit PIEZO1 to maintain stemness[124,142]. This potential signaling axis may explain the changes in Slamf6 and TIM-3 expression upon PIEZO1 modulation but needs to be explored further.

In addition to regulating receptor clustering that induces PIEZO1- and TCR-mediated signal transduction at the immune synapse, the actin cytoskeleton has been reported to potentiate mechanisms that drive lytic granule assembly and release in cytotoxic CD8^{+} T cells. We identified various pathways involved in membrane trafficking and cytoskeletal reorganization in PD-1-APEX2 and PD-1 phospho-peptide pulldown studies (Chapter 3.3) that may be necessary for regulating cytotoxic granule release (Figure 2.1h-j). Furthermore, we observed significantly less perforin, granzyme and serpin peptides in proteomic analysis

of PIEZO1 KO CD8^{+} TILs compared to WT TILs, in line with our flow cytometry data[98,99]. It is possible that PIEZO1-mediated $Ca^{2+}$ influx promotes signaling that induces lytic granule pathway activation. These data strongly suggest that PIEZO1 mechanosensing is involved in mechanisms that regulate the assembly and release of cytotoxic granules.

Given the mechanosensitive nature of PIEZO1, we appreciate that variations of FFL forces may be able to further promote T cell activation and motility independent of antigen recognition[77]. Our studies have focused on force-from-filament or tethered-spring mechanics, where reorganization of the actin cytoskeleton mediated by the TCR signaling cascade provides force from within the cell to open PIEZO1[77,97]. Still, it is worth noting that cyclical pressure and shear stress may have alternative effects on PIEZO1 and subsequent signaling in T cells, which has been clearly demonstrated in other immune cells, including macrophages[73,74,76,77,88,101]. Our preliminary studies exposing CD8^{+} T cells to cyclical hydrostatic pressure demonstrate that external forces provide signaling boosts in CD8^{+} T cells and this requires further analysis.

In summary, we discovered that PD-1 ligation induces the association of PIEZO1 and PD-1 and identified a new mechanism by which PD-1 exerts its inhibitory signals. PIEZO1 is activated upon TCR stimulation, likely by contractile actinomyosin forces at the immune synapse, and is inhibited by PD-1 ligation. Our findings are the first to show that mechanically-mediated signaling influences exhausted CD8^{+} T cell subpopulations and activation competency in CD8^{+} T cells, subsequently affecting cancer pathogenesis. The selective inhibition of PIEZO1 by PD-1 illuminates the significance of the PIEZO1 pathway for regulating T cell function and introduces a novel coinhibitory receptor target class. Further studies are needed to determine the precise mechanisms controlling PD-1 and PIEZO1 association, the specific downstream pathways involved and the effect of FFL forces on this biology. Our studies underscore the importance of mechanics to T cell biology and expand our understanding of the diverse functions of PD-1.

## 2.4 Materials and methods

*Cell lines*

Jurkat E6.1 and human PD-1-expressing Jurkat E6.1 cells (35.8 line transduced with an ORF-T2A/IRES-GFP reporter) (a gift from N. Haining/K. Yates, Dana Farber Cancer Institute) were cultured in RPMI media supplemented with 10% FBS, 1% penicillin/streptomycin, 1% HEPES and 0.1% BME (R10). MC38-OVA (a gift from N. Collins, Dana-Farber Cancer Institute), B16-OVA (a gift from D. Sen, Dana-Farber Cancer Institute), MC38-WT (a gift from D. Vignali, University of Pittsburgh School of Medicine), B16.F10 (a gift from G. Dranoff, Novartis Institutes for Biomedical Research, Cambridge, MA) and 293x (a gift from C. Kadoch, Dana-Farber Cancer Institute) cells were cultured in DMEM supplemented with 10% FBS, 1% penicillin/streptomycin and 20 $\mu$g ml$-1$ gentamicin. MC38-OVA and B16-OVA cells were produced by transduction of parental MC38 and B16.F10 cells with the lentiviral vector TRC-pLX305 (Broad Institute) containing OVA protein.

*PD-L1 bead generation*

M-450 Tosyl-activated magnetic Dynabeads (Invitrogen #14013) were washed using a microcentrifuge tube magnet (Dyna-Mag-2, Thermo Fisher Scientific) in 0.1M sodium phosphate buffer, pH 7.4-8.0. Magnetic beads were then treated with a mixture of human or mouse CD3 crosslinking antibody (BioXcell, human clone OKT3, murine clone 145-2C11), CD28 (BioXcell, human clone 9.3, murine clone 37.51) crosslinking antibody and either recombinant human or murine PD-L1 fusion protein (R&D Systems) or recombinant human or mouse IgG$_1\kappa$ (Southern Biotech) depending on the PD-1 construct used. Various titrations of protein concentrations were tested to determine which ratio generated the most significant inhibition of T cells: 10/90%, 20/80%, 40/60%, 60/40% and 80/20% of TCR components and PD-L1 or IgG$_1\kappa$ respectively were crosslinked to beads using a total of 200$\mu$g of protein per 1mL of beads. Beads were incubated and rotated for 16-24 h at room temperature. Beads were then applied to the Dyna-Mag-2 to remove supernatant and washed in Buffer 2 (PBS$^{-/-}$ supplemented with 0.1% BSA and 2mM EDTA pH 7.4). To deactivate the remaining free tosyl groups on the beads, beads were rotated overnight at room temperature in Buffer 3 (0.2M Tris-HCL supplemented with 0.1% BSA, pH 8.5). Beads were washed 3X more with Buffer 2 and reconstituted at 100 million beads per 1mL of Buffer 2 and stored at 4°C prior to use.

*On-bead protein ratios and cell:bead ratios*

Naïve CD8$^+$ T cells were isolated from spleens of wild type mice using negative selection magnetic-activated cell sorting (MACS) isolation (Miltenyi). Naïve CD8$^+$ T cells were stimulated for 24 h on 96-well U-bottom plates coated with anti-CD3 and anti-CD28 crosslinking antibodies. After 24 h, cells were moved to a new U-bottom plate. PD-L1 or hIgG$_1\kappa$ beads containing various protein ratios outlined above were added to CD8$^+$ T cells at various cell:bead ratios (1:2, 1:4, 1:6) for 48 h. Supernatant was collected 48 h following the addition of beads for cytometric bead array (CBA) analysis (BD Biosciences). After 48 h, CD8$^+$ T cells were stained and run on the BD Symphony for flow cytometric analysis as outlined in Chapter 2.4 *Flow cytometry staining.*

*PD-1-APEX2 plasmid design, cloning and stable expression*

PD-1 sequences were obtained from NCBI and were modified using the codon optimization tool from Integrated DNA Technologies (IDT). APEX2 sequences have been previously described[102]. PD-1-APEX2 fusion sequences contain PD-1 linked to APEX2 on the C-terminal tail by an 8-residue serine-glycine linker (GGSSGGSS) and a FLAG-TAG added to the C-terminal tail of APEX2. PD-1 ITIM and ITSM constructs were generated by substituting PD-1 tyrosine phosphorylation site residues with phenylalanine residues. All human and murine PD-1-APEX2 double-stranded gene fragments (gBlocks) were generated by IDT. Cloning of gBlocks into the pXPR_053 plasmid (Addgene #113591) was completed by GenScript.

To generate stable PD-1-APEX2-expressing Jurkat cell lines, 293x cells were transfected with PD-1-APEX2 fusion plasmids along with PsPax2 and MD2G packaging plasmids suspended in Optimem (Life Technologies #31985-062) and polyethylamine "Max" (PEI, Polysciences #24765-2). Transfection mixtures were added to 293x cells and were supplemented with fresh media after 24 h. Lentivirus was harvested 48 h following media supplementation by ultracentrifugation for 2 h at 71,934.8 RCF at 4°C. Viral titer was calculated using serial dilutions of the viral stock on 293x cells in DMEM complete media containing PEI "Max". A multiplicity of infection of 30 was used to spin transduce Jurkat cells for 2 h at 652 RCF at 37°C. Jurkat cells were stained with human PD-1 surface antibody (BioLegend, clone EH12.2H7, #329936) and

checked for expression using flow cytometry 24 h and 48 h following transduction. Highly expressing PD-1-APEX2 fusion clones were sorted on the BD Aria II. Stocks were frozen for future experiments.

*APEX2 proximity labelling and sample processing*

PD-1-APEX2-expressing Jurkat cells were cultured at a concentration of 1 million cells/mL in labelling media (RPMI supplemented with 10% FBS, 1% penicillin/streptomycin, 1% HEPES, 0.1% BME and 500$\mu$M biotinyl tyramide purchased from Toronto Research Chemicals) for 2 h. TCR-PD-L1 or TCR-control Dynabeads (see Chapter 2.4 *PD-L1 bead generation*) were added to cells at a ratio of 1:4 cells/beads for the specified timepoints along with no bead-treated (0 min) and no hydrogen peroxide-treated controls. Following each timepoint, hydrogen peroxide ($H_2O_2$, Sigma Aldrich) was added at a final concentration of 1mM to each condition for 1 min. The labelling reaction was quenched using 2X quenching buffer (DPBS supplemented with 20mM sodium ascorbate, 10mM trolox and 20mM sodium azide) and cells were spun down immediately at 726 RCF for 2 min. Cells were immediately washed three times with ice-cold 1X quenching buffer and spun down at 726 RCF for 2 min. Following the third 1X quenching wash, cells were washed with 10 mL ice-cold PBS and 1 million cells were taken for Western blotting analysis. Cells were then spun down a final time at 726 RCF for 2 min. All PBS was removed from cell pellets, which were flash-frozen on dry ice and stored at -80°C until processing and streptavidin pulldown.

PD-1-APEX2-expressing Jurkat cell pellets were processed using previously described methods with slight modification[143]. Cell pellets were lysed in filtered 8M urea with 1% SDS at room temperature for 15 min. 55% ice-cold trichloroacetic acid (TCA) was added to lysates at a 1:1 ratio and left on ice for 15 min to precipitate the protein. Lysates were spun down at 20,817 RCF for 15 min at room temperature to prevent urea from crashing out of solution. The supernatant was discarded and protein pellets were washed 4X with ice-cold acetone and spun down at 20,817 RCF for 10 min following each wash. Protein pellets were then air-dried and resuspended in 8M urea lysis buffer supplemented with 1% SDS and 10mM tris(2-carboxyethyl)phosphine (TCEP, Sigma) and 100 mM $NH_4CO_3$. Pellets were water-bath sonicated for 3 cycles of 30 s and vortexed mixed at 37°C for 2 h until the pellets were completely resuspended. Redissolved pellets were checked for an alkaline pH and then spun down at 20,817 RCF for 15 min at room

temperature. Clear supernatants were transferred to new microcentrifuge tubes and freshly prepared

400mM iodoacetamide in 50mM $NH_4CO_3$ was added to each sample at a final concentration of 20mM.

Samples were immediately vortexed and incubated in the dark at room temperature for 25 min. During the

incubation period, streptavidin beads (Pierce) were washed twice with 4M urea and 0.5% SDS. Alkylation

was quenched using a solution of 100mM dithiothreitol (DTT) containing streptavidin beads such that each

sample received 100μL beads and reached a final concentration of 50mM DTT, 4M urea and 0.5% SDS

(1:1). Samples containing streptavidin beads were rotated overnight at 4°C. Samples were briefly spun

down and applied to the Dyna-Mag-2 to remove the supernatant. Beads were washed with 4M urea and

0.5% SDS and transferred to new Eppendorf tubes to decrease background signal. Beads were washed

3X more with 4M urea and 0.5% SDS followed by 3 washes with 4M urea to remove all detergent.


*Mass spectrometry sample preparation*

Streptavidin beads were digested with lysyl endopeptidase (LysC, 2mg/ml, Wako) in 50µl 200mM 3-[4-(2-

hydroxyethyl)piperazin-1-yl]propane-1-sulfonic acid (EPPS) pH 8.5 and 2% acetonitrile at 37°C. Trypsin

(50µl stock with EPPS buffer and a final dilution of 1:100, Promega #V5111) was added for additional digest

over night at 37°C. Beads were removed with a magnetic rack and clear supernatants were transferred to

new tubes. Peptide digest reactions were directly labelled with TMT11plex (Thermo Fisher Scientific

#A34808) or TMT16plex (Thermo Fisher Scientific #A44520) reagents in 200mM EPPS pH8.5, 30%

acetonitrile for 1 h at room temperature. Labeling efficiency was measured by MS of mixed small aliquots

of the labeling reactions and was >95%. Frozen and thawed TMT labeling reactions were quenched with

0.3% hydroxylamine for 15 min at room temperature. Reactions were then mixed, dried in a speed vac

centrifuge to near completion and subjected to alkaline reversed phase fractionation (Thermo Fisher

Scientific #84868) with 12 elution subsequent fractions of 10%, 12.5%, 15%, 17.5%, 20%, 25%, 30%, 35%,

40%, 50%, 65% and 80% acetonitrile. Fraction pairs 1+7, 2+8, 3+9, 4+10, 5+11, 6+12 were mixed, dried

down to completion, desalted with Stage tips and run on Orbitrap Lumos mass spectrometers (Thermo

Fisher Scientific).

*Mass spectrometry analysis*

Data collection followed a synchronous precursor selection (SPS) MS[3] TMT method[144]. Peptides were separated prior to the electrospray ionization with a Proxeon EASY-nLC1200 system over a ~35cm capillary column of 100μm inner diameter packed with Accucore C18 beads (2.6 μm, 150Å, Thermo Fisher Scientific). Service MS[1] scans were performed in the Orbitrap at a resolution of 120,000, mass range 400-1400 Th. After collision induced dissociation (CID, CE=35) and using an isolation window of 0.4 *m/z*, MS[2] was performed in the ion-trap with maximum injection times of 150-400 ms. For MS[3] quantification, precursors were selected following a Top10 method followed by high-energy collision-induced dissociation (HCD, CE=65). Orbitrap MS[3] analysis was done at a resolution of 60,000 at 200Th with varying injection times of up to 650 ms and charge-state dependent variable isolation windows from 0.7 to 1.2 Da as described previously[145]. Peptide-spectrum matches (PSM) were obtained by a SEQUEST (v.28, rev.12) based software, searching a database with respective UniProt mouse and human reference proteomes with added common contaminants and reverse peptide sequences as decoy. After mzXML conversion of spectra, searches used a mass tolerance of 20 p.p.m. for precursors and a fragment-ion tolerance of 0.9 Da. Searches allowed for up to two missed trypsin cleavage sites with dynamic modification of oxidized methionines (+15.9949 Da) and static peptide N-terminal and lysine modifications with TMT11 (+229.1629 Da) or TMT16 (+304.2071 Da). PSM were filtered by linear discriminant analysis with a false discovery rate (FDR) of 1% and a following FDR of 1% for collapsed proteins. MS[1] data were calibrated post search and searched again. TMT signal to noise quantification for peptides was filtered for an MS[2] isolation specificity of 70% or greater and a summed signal to noise of 200 or greater for all TMT channels for each peptide. Details of TMT intensity quantification applied were described previously[145]. Scaled quantification data were analyzed by two-way clustering (Ward's method) using the JMPPro statistical software package and volcano plots were generated using GraphpadPrism8 with statistical significance determined by multiple t-tests without multiple comparison correction and alpha=0.05.

*PIEZO1 co-immunoprecipitation and sample processing*

hPD-1-overexpressing Jurkat cells were treated with TCR-PD-L1 or TCR- control beads for 20 min. Following 20 min, cells were immediately spun down at 726 RCF for 2 min and washed twice with cold

PBS. Cell pellets were flash-frozen on dry ice following the complete removal of PBS. Non-bead treated and negative controls were also prepared and all conditions were prepared in quadruplicate. Cell pellets were lysed in 25mM Tris-HCL pH 7.4, 150mM NaCl and 1% NP40 (lysis buffer) for 15 min on ice. Lysates were spun down at 4°C for 15 min at 20,817 RCF. Supernatants were moved to new Eppendorf tubes, precleared with streptavidin beads (Pierce) and rotated for 1 h at 4°C. Piezo1-biotin conjugated antibody (FabGennix International, #FAM38A-biotin) was added to samples at a 1:250 dilution for 8 h and rotated at 4°C. A non-biotin-conjugated Piezo1 antibody (ProteinTech #15939-1-AP) was added to the negative control samples at a 1:250 dilution and rotated for 8 hours at 4°C. Streptavidin beads were washed twice with lysis buffer and 100μL of streptavidin beads were added to each sample and rotated overnight at 4°C. Eppendorf tubes were applied to the Dyna-Mag-2 to remove the supernatant. Beads were washed with ice-cold PBS and moved to new Eppendorf tubes. Beads were then washed 3X more with ice-cold PBS and processed for mass spectrometry. Peptide LAAFPEDR (New England Peptides) uniquely mapping to PD-1 was used for trigger peptide analysis[106].

*Phospho-flow cytometry time points and antibodies*

Naïve CD8+ T cells were isolated from spleens of wild type mice using negative selection MACS isolation (Miltenyi). Naïve CD8+ T cells were stimulated for 48 h on 96-well U-bottom plates coated with 4μg/mL anti-CD3 and anti-CD28 crosslinking antibodies. Cells were then rested in R10 media in 96-well V-bottom plates for 4 h prior to restimulation. CD3/CD28 IgG control beads or PD-L1 beads were added at a cell:bead ratio of 1:4 or 1:5 for the specific timepoints: 2, 5, 10 and 20 min. Cells were spun down for 20 s up to 800 RCF to pellet cells and remove media. Cell/bead mixtures were immediately fixed in 2% paraformaldehyde (PFA) at room temperature for 10 min. One volume of PBS was added to each well and cells were again spun down at 800 RCF for 2min. Cells were then washed twice with MACS buffer (PBS-/-, 1% FBS, 2mM EDTA) and spun down at 800 RCF for 2min. 90% ice-cold methanol (MeOH) was slowly dropped onto the cells and mixed for permeabilization. MeOH-permeabilized cells were stored in the -80°C freezer prior to use or left on ice for 20 min to complete permeabilization. One volume of MACS buffer was added on top of the MeOH and spun down at 800 RCF for 2min. Wells were washed once more with MACS buffer and stained with pERK (Cell Signaling Technologies (CST), clone 197G2), pS6 (CST, clone D57.2.2E) and pAKT (CST,

clone D9E) diluted 1:50 for 1 h at room temperature in the dark. Stain was washed off with MACS buffer and samples were resuspended and run on the BD LSRII or BD FACSymphony.

*Pressure chamber assay*

Naïve CD8$^+$ T cells were stimulated naïve with 4$\mu$g/mL of crosslinking CD3 and CD28 antibodies for 48 h. Cells were then rested in culture media for 4 h to ensure that no active signaling was occurring. Rested CD8$^+$ T cells were exposed to pressure pulses of 45-60mmHg (~0.06-0.08atm) or static pressure for 20 min in a cell culture incubator at 37°C, 5% CO2 using previous described methods[73]. After 20 min, CD8$^+$ T cells from both conditions were immediately fixed with 2% PFA, permed with MeOH and stained for phospho-flow cytometric analysis (see Chapter 2.4 *Phospho-flow cytometry time points and antibodies)* to assess the effects of pressure on CD8$^+$ T cell signaling.

*Fluo-4 and Indo-1 Ca$^{2+}$ flux assay*

Naïve CD8$^+$ T cells from WT mice or E8i-Cre-ER$^{T2}$ Piezo1$^{flx/flx}$ Cre+ or Cre- mice pretreated with tamoxifen were isolated from spleens using MACS. Purified CD8$^+$ T cells were stimulated on 96-well U-bottom dishes coated with 4$\mu$g/mL of crosslinking murine CD3 and CD28 antibodies for 48 h. Stimulated CD8$^+$ T cells were then rested for 4-12 h in R10 media and moved to a fresh, uncoated 96-well U-bottom plate. WT or E8i-Cre-ER$^{T2}$ Piezo1$^{flx/flx}$ CD8$^+$ T cells were then stained in 1% FBS PBS for 1 h at room temperature with near IR fixable LIVE/DEAD stain (1:600, Thermo Fisher Scientific #L34976) and 1$\mu$M of Fluo-4 (Thermo Fisher Scientific #F-14201) or Indo-1 (Thermo Fisher Scientific #I1226), respectively, as Cre-expressing mice contain an eGFP reporter that would not be compatible with Fluo-4. Cells were then washed twice with 1% FBS PBS and resuspended in R10 media. TCR-PD-L1 or TCR-control beads were added at a ratio of 1:5 cell:bead and Yoda1 was added to samples at a final concentration of 5$\mu$M. Following addition of PIEZO1 agonist or beads for specified timepoints, cells were immediately acquired and analyzed on the BD FACSymphony or BD LSRII. Ca$^{2+}$ influx was assessed by %GFP-positive cells for Fluo-4 dye compared to untreated controls and by the ratio of bound (BUV395) to unbound (BUV496) Ca$^{2+}$ using Indo-1.

*Western blotting*

Enriched CD8^{+} T cells, Jurkat cells or tumor cells were lysed in Pierce RIPA Buffer supplemented with Halt Protease and Phosphatase Inhibitor Cocktail (100X) for 15 min on ice. Whole cell lysates were spun down at 20,817 RCF at 4°C for 15 min. Supernatants were collected and transferred to new Eppendorf tubes and 10μL of each lysate was taken for protein estimation using the Pierce BCA Protein Assay Kit to normalize for protein loading. Cleared lysates were denatured with 4X Laemmli Sample Buffer (BioRad) or 4X NuPAGE LDS (Invitrogen) containing beta mercaptoethanol (BME) and boiled for 5 min at 95°C. 15-40μg of protein per lysate was loaded and run on a NuPAGE 4-12% Bis-Tris protein gel and then transferred onto a nitrocellulose membrane. Ponceau staining was performed to check transfer efficiency and protein loading. Membranes were then blocked for 1 h in TBS supplemented with 1% Tween (TBS-T) and 5% milk or in Licor Intercept Blocking Buffer supplemented with 0.2% Tween at room temperature. Membranes were then incubated with primary antibodies, including pERK (CST, 1:1000, #4370S), pAkt (CST, 1:1000, #4060S), Histone H3 (CST, 1:1000, #9715S), Streptactin-HRP (Bio-Rad, 1:50,000, #1610381), β-Actin (CST, 1:1000, #3700S) and rocked overnight in blocking buffer at 4°C. Membranes were washed 3X in TBS-T buffer and incubated with the respective HRP-linked secondary antibodies (HRP-linked anti-rabbit IgG #7074P2, HRP-linked anti-mouse IgG #7076P2 and HRP-linked anti-rat IgG #7077S, CST, 1:2000) in blocking buffer for 1 h at room temperature. Membranes were then treated with SuperSignal West Pico PLUS Chemiluminescent Substrate (ThermoFisher #34580) and imaged using the Amersham Imager 600. Membranes incubated with fluorescent Licor secondary antibodies were directly imaged on Licor Odyssey CLx following TBS-T washes. When necessary, membranes were stripped with Restore PLUS Western Blot Stripping Buffer (Thermo Scientific #46430) for 15 min at room temperature, blocked and re-probed with primary and secondary antibodies as described above.

*Jurkat XLGenEpi nucleofection and stable clone selection*

The XLGenEPi PIEZO1 reporter plasmid driven by a doxycycline-inducible Tet-on system was a generous gift from the Pantazis lab (Figure 2.S7a). Jurkat cells were co-nucleofected with the XLGenEpi plasmid and pCMV_pBase at a molecular ratio of 1:1 using Lonza's SE Cell line kit (cat. V4XC-2024) and corresponding CL-120 program on Lonza's Amaxa-4D Nucleofector. The pCMV_pBase plasmid is a non-viral vector that

expresses the piggyBac transposase (pBASe) which, when co-transfected, allows for the integration of the XLGenEpi transgene into the genome using two terminal repeat domains flanking the XLGenEPi transgene (Figure 2.S7a)[146]. This integration into the genome allows for the generation of stable XLGenEPi clones that can be selected for using blasticidin (BSD). 2μg of XLGenEpi and equimolecular amounts of pCMV_pBase plasmids were used to nucleofect 1 million Jurkat cells in cuvettes. Cells were rested in complete RPMI media (RPMI supplemented with 10% FBS, 1% penicillin/streptomycin, 1% HEPES, 0.1% BME, 1mM sodium pyruvate and 4.5g/L of glucose) for 24 h following nucleofection. To generate stable clones, XLGenEPi nucleofected cells were selected with 8μg/mL BSD for 7 days. Cells were then rested in complete RPMI media for 24 h and treated with 200 ng/mL doxycycline for 24 h to induce PIEZO1 reporter expression. Selected Jurkat cells were then treated with 5μM Yoda1 and GFP-positive clones were immediately sorted on the BD FACS Aria and cultured to generate stable cell lines.

*Flow cell chamber preparation and TIRF imaging*

6-channel μ-Slide VI Glass Bottom slides (Ibidi #80607) were coated with Poly-D-Lysine for 1 h at room temperature. Excess Poly-D-Lysine was removed from the channel and the channel was washed 4X with PBS. Chambers were then coated with 2μg/mL CD3 and CD28 crosslinking antibodies and 4μg/mL PD-L1 or mIgG$_1$κ overnight at 4°C. Slides were then washed 4X with PBS and 80μL of PBS was left in the flow cell chamber to prevent drying out prior to use.

XLGenEPi Jurkat cells were treated with ImmunoCult Human CD3/CD28 T cell activator (STEMCELL Technologies #10971) for 48 h prior to imaging to induce PD-1 expression. XLGenEPi Jurkat cells were treated with doxycycline (200ng/mL) for 24 h prior to imaging to induce XLGenEPi expression. XLGenEPi Jurkat cells were then stained with F-actin SPY550-FastAct (1:500, Cytoskeleton #CY-SC205) and anti-human PD-1 AF647 (1:50, Biolegend #329910 clone EH12.2H7) for 1 h at 37°C in PBS supplemented with 10% FBS (PBS-F). Cells were washed twice with PBS-F and resuspended at a concentration of 1 million/mL in complete RPMI media.

TIRF imaging was performed using a fully motorized Nikon Ti inverted microscope equipped with a Nikon Ti-TIRF-EM Motorized Illuminator and a Nikon LUN-F Laser Launch with single fiber output (488nm, 90mW;561 nm, 70mW; 640nm, 65mW). To immobilize the sample, 80 $\mu$l of stained XLGenEPi Jurkat cells were flowed into one of the 6 coated $\mu$-Slide channels (Ibidi #80607). Flow was established by capillarity using a Kimwipe. Imaging was performed under static conditions (e.g., not flow). Images were collected using an Apo TIRF 100x/1.49 DIC oil immersion objective lens with Nikon NF immersion oil, adjusting the correction collar to minimize spherical aberration. Images were captured with an Andor Zyla 4.2 Plus sCMOS monochrome camera using the 16-bit dual gain digitizer mode, 540 MHz readout rate and 2x2 pixel binning (resulting pixel size 0.1 um/px) and Nikon Elements Acquisition Software AR 5.02. The TIR angle for each channel was adjusted using fluorescence beads in the same flow chambers as used in the experiments and verified with a control sample. Signal from the different channels was acquired sequentially using a Chroma ZT 405/488/561/640 multi-band pass dichroic mirror mounted on a Nikon TIRF filter cube located in the filter cube turret, and band pass emission filters for XLGenEPi AF488 (Chroma ET525/50m), SPY5550-FastAct (Chroma ET 595/50m) and PD-1 AF647 (Chroma ET 655lp) channels, respectively, located on a Sutter emission filter wheel within the infinity space of the stand. Time-lapse imaging was performed with a time interval of 20 s and total acquisition time of 10 min. A ND16 filter was introduced in the lightpath to reduce irradiation. Imaging conditions were optimized to reduced photobleaching and phototoxicity.

*Fiji analysis for TIRF imaging*

TIRF image analysis was completed using a custom macro built in Fiji/ImageJ. The TIRF images were opened in Fiji and split into the different fluorescent channels. A 500 pixel rolling ball background subtraction was applied to reduce background intensities close to 0. The individual PD-1 and PIEZO1 channels were processed by performing a Tophat/difference of Gaussian filter to emphasize the small puncta. The processed images were segmented by intensity-based thresholding. A close filter followed by a size filter was applied to the thresholded masks to generate the final masks for PD-1 and PIEZO1. The Euclidean distance map of the masks conveys the distance from every point in the background to the objects in the masks. The distances were converted into a pixel intensity where close objects have a higher intensity than

far objects (overlapping objects would be the brightest). This analysis was used to measure the distance from the PD-1 puncta to the PIEZO1 puncta and vice versa. Regions of interest (ROI) were then drawn to demarcate cell boundaries to calculate the parameters on a per cell basis. The mask areas, the intensities of the signal as well as their distance to each other for all timepoint and all ROIs were measured.

*Mice*

Seven- to ten-week-old age-matched female or male mice were used for all *in vivo* experiments and seven- to fourteen-week-old mice were used for CD8^{+} T cell isolation and *in vitro* experimentation. Wild type C57BL/6J mice were purchased from Jackson Laboratories. E8I-Cre-ER[T2] mice were a generous gift from the Vignali lab. Homozygous E8I-Cre-ER[T2] mice were crossed with homozygous Piezo1[flx/flx] mice purchased from Jackson Laboratories (Stock #029213). Mice were crossed until they were fixed for the Piezo1[flx/flx] mutant allele as assessed by Transnetyx, an automated genotyping service. The Piezo1-2 WT probe was used to detect the WT *Piezo1* allele (forward primer: CTGTCCCCTTCCCCATCAAG; reverse primer: GGGTCCAGGGTAGACAACAG). The L1L2-Bact-P MD probe (forward primer: GCTGGCGCCGGAAC; reverse primer: GCGACTATAGAGATATCAACCACTTTGT) was used to detect the L1L2_Bact_P cassette, composed of an FRT site followed by a lacZ sequence and a loxP site, confirming the integration of the floxed *Piezo1* mutant allele. eGFP E8I-Cre-ER[T2] and Rosa26-LSL TD tomato knock-in activity reporters were also quantified by Transnetyx using the eGFP (forward primer: CGTCGTCCTTGAAGAAGATGGT; reverse primer: CACATGAAGCAGCACGACTT) and tdRFP (forward primer: AGATCCACCAGGCCCTGAA; reverse primer: GTCTTGAACTCCACCAGGTAGTG) probes, respectively. Heterozygous Cre mice were bred to generate both Cre+ and Cre- littermates. To induce *Piezo1* deletion, Cre+ and Cre- mice were intraperitoneally injected with 8 doses of 10mg/mL tamoxifen daily. Deletion efficiency was assessed using RT-qPCR with probes spanning Piezo1 exons 20-23 containing the loxP sites, listed below under Chapter 2.4 *RT-qPCR*. Results indicated that Cre+ mice required two copies of the Cre+ allele for ~70% PIEZO1 deletion. Cre+ and Cre- mice Piezo1[flx/flx] mice were then bred separately to ensure the homozygous expression of Cre alleles for efficient gene deletion. All mice were housed in specific pathogen-free conditions and all animal experimentation was performed in accordance with IACUC

regulations and animal care guidelines from the Harvard Medical School Standing Committee on Animals and the National Institute of Health.

*RT-qPCR*

Murine CD8^{+} T cells were isolated from the spleens and inguinal lymph nodes of Cre+ and Cre- naïve mice treated with 10mg/mL tamoxifen for 8 days using CD8^{+} MACS or cell sorting. Isolated CD8^{+} T cells were washed with PBS and spun down at 453 RCF for 5 min. PBS was removed from the cell pellets and cell pellets were frozen at -80°C or immediately processed for RNA. RNA was isolated from purified CD8^{+} T cell pellets using Qiagen's RNAeasy Mini Kit (#74104). RNA was quantified using Qubit RNA HS Assay Kit (#Q32852) and RNA concentration was normalized across samples. Reverse transcription was perform using Superscript VILO cDNA Synthesis Kit (Thermo Fisher Scientific #11-754-050) to generate cDNA. cDNA was diluted and mixed with *Piezo1* specific fluorescein amidites (FAM) Taqman probes (Thermo Fisher Scientific, Assay ID # Mm01241547_g1 and #Mm01241549_m1) and control eukaryotic 18s rRNA FAM probe (Thermo Fisher Scientific, Assay ID #Hs99999901_s1) according to the Fast Advanced Mastermix real time PCR protocol. PCR mixtures were plated in Roche LightCycler 480 96-well plates (#04729692001) and sealed. Plates were run on the Roche LightCycler 480 with a 20 s polymerase activation step at 95°C followed by 40 cycles of 1 s of denaturing at 95°C and 20 s of annealing and extending at 60°C.

*PIEZO1 KO CD8^{+} T cell stimulation and flow cytometry*

E8I-Cre-ER[T2] Cre+ and Cre- mice were treated with 8 doses of 100mg/mL tamoxifen. Naïve CD8^{+} T cells were isolated from spleens of tamoxifen-treated mice using negative selection MACS isolation (Miltenyi). Naïve CD8^{+} T cells were stimulated for 48 h on 96-well U-bottom plates coated with a titration of anti-CD3 and anti-CD28 crosslinking antibodies (0, 0.1, 1.0, 5.0 and 10μg/mL). Supernatant from each sample was collected 48 h following the addition of beads for CBA analysis (BD Biosciences). After 48 h, CD8^{+} T cells were stained following the protocol outlined in Chapter 2.4 *Flow cytometry staining* and run on the BD FACSymphony for flow cytometric analysis.

*Tumor implantation*

Mice were anesthetized with 2.5% 2,2,2-tribromoethanol (Avertin, Sigma-Aldrich catalog no. T48402-25G) and injected in the flank subcutaneously with $2.5 \times 10^5$ MC38, B16.F10 or B16-OVA tumor cells. Once palpable tumors were observed, tumors were measured every other day to calculate tumor volume over time. Tumor volume was calculated using the equation $(L*W^2)/2$ where L denotes tumor length and W denotes tumor width. Mice were monitored for body condition and weight loss. Mice with tumors that exceeded 2000mm$^3$, that were severely ulcerated or that infiltrated the i.p. cavity were sacrificed.

*Tumor infiltrating lymphocyte isolation*

Tumors were harvested at day 15 following implantation and processed for analysis. Extracted tumors were mechanically chopped and treated with collagenase type 1 (Worthington Biochemical, #LS004194) and mixed for 25 min at 37°C. Lymphocytes were enriched using a 40/70% Percoll gradient (see Chapter 3.4 *Tumor Experiments*)

*Flow cytometry staining*

Cells were surface stained with antibodies listed below at a 1:100 dilution (unless otherwise noted) in 96-well V-bottom plates for 45 min in the dark on ice. Samples were washed twice with MACS buffer (PBS-/-, 1% FBS, 2mM EDTA) and fixed for 20 min in the dark at room temperature and permeabilized with FoxP3/Transcription Factor Staining Buffer Set Kit (eBioscience). Cells were stained with intracellular antibodies listed below at a 1:100 dilution (unless otherwise noted) for 1 h in the dark on ice and washed twice with eBioscience Permeabilization Buffer. All washes used 200μL of the specified buffers and spins were performed at 726 RCF for 2 min at 4°C. Fixed and stained samples were run on the BD FACSymphony and analyzed using FlowJo software.

*Antibodies for flow cytometry and sorting*

Flow cytometry analyses were performed on a BD FACSymphony and cell sorting was performed on a BD Aria II. The following fluorescent antibodies were purchased from Biolegend for flow cytometry and cell

sorting: human PD-1 (clone EH12.2H7, #329936) and murine CD45.2 (APC-Cy7, clone 104, #109824), CD8b (Alexa Fluor700, clone 53-6.7, #00730), CD44 (APC, clone IM7, #103012), PD-1 (PE-Cy7, RMP1-30, #109110), CD69 (BV421, H1.2F3, #104528), CD28 (FITC, clone E18, #122008), CD62L (BV605, PerCPCy5.5, clone MEL-14), CD3e (BUV395, PerCpCy55, FITC, clone 145-2C11), Perforin (PE, clone S16009A), Granzyme B (BV421, clone GB11, #515408), CTLA4 (BV605, clone UC10-4B9, #106323), Tim3 (BV711, BV421, clone RMT3-23, #119727) and Slamf6 (PE, APC, 330-AJ). The following fluorescent antibodies were purchased from BD Biosciences: CD4 (BUV496, BUV737, clone GK1.5), LFA1 (BV786, clone M17/4) and Ki67 (PerCpCy55, clone B56). FoxP3 (Alexa Fluor 488, clone FJK-16s, #53-5773-82), LIVE/DEAD Fixable Aqua dead cell stain (1:600, L34957) and LIVE/DEAD Fixable Near-IR dead cell stain (1:600, L34976) were purchased from Thermo Fisher Scientific.

*Proteomic analysis on sorted CD8$^+$ TILs*

Sorted cells were lysed in 200μL of lysis buffer (50mM Tris pH 8.5, 150mM NaCl, 2%SDS) containing protease and PhosStop phosphatase inhibitor (MilliporeSigma, 4906837001) and Complete EDTA-free Protease Inhibitor (Millipore Sigma, 11873580001). Lysates were shredded using QiaShredder (Qiagen, 79656) in a microcentrifuge at 20,817 RCF for 5 min. Proteins were reduced in 1.5mL Eppendorf tubes with 1μL of fresh 1M DTT for 60 min at 37°C with gentle shaking (1000 RPM) using the Eppendorf ThermoMixer C (Orbital Shakers). After cooling samples to room temperature, reduced cysteines were alkylated by adding 20μL of 0.5M ammonium bicarbonate and 10μL of 0.4M iodoacetamide (prepared in 50mM ammonium bicarbonate). Samples were incubated for 25min at room temperature in the dark. The reactions were then quenched by adding 10μL 1M DTT. After alkylation, detergent and other contaminants were removed by SP3 cleanup as described in the phospho-peptide pull-down protocol (Chapter 3.4 *Phospho-peptide pulldowns*) and subsequently digested, labelled, and analyzed as described in Chapter 2.4 *Mass spectrometry analysis* outlined above.

*In vivo PD-1 blockade and Piezo1 agonist treatment*

Two 100μg doses of anti-PD-1 (BioXcell, clone 29F.1A12, #BE0273) or rat IgG2a isotype control (BioXcell, clone 2A3, #BP0089) were administered interperitoneally to mice on days 10 and 13 (B16-OVA model) or

14 and 17 (MC38 model) following tumor implantation. Yoda1 (Tocris, #5586) was reconstituted in DMSO to reach a final stock concentration of 17 mg/mL. Reconstituted Yoda1 was freshly formulated with PBS and sonicated prior to each experiment to obtain a dose of 7.5mg/kg per mouse (250ug/200uL) administered interperitoneally 3-5 times between days 5 and 13.

## 2.5 Acknowledgements

# Chapter 3:

## Differential signaling mechanisms of PD-1 ITIM and ITSM motifs

Juhi Kuchroo, Jessica Buck and Maria Clark led the *in vivo* tumor and corresponding flow cytometry experiments (Figure 3.1). Marian Kalocsay, Gary Bradshaw and Robyn Eisert processed and ran samples for PD-1-APEX2 proximity labelling, phospho-proteomic analysis and phospho-peptide pulldowns (Figure 3.3-Figure 3.9).

## 3.1 Introduction

Following ligation by PD-L1 or PD-L2, PD-1 ITIM and ITSM motifs are phosphorylated and subsequently recruit SH2-domain containing phosphatases SHP1/2, in part, to propagate inhibitory signals that attenuate T cell function[14,15,30,48,147,148]. While the recruitment of SHP1/2 has been well-established in the literature, the specific function of each PD-1 tyrosine phosphorylation motif on T cell inhibition is not clearly understood[14,50]. The vast array of molecular processes attenuated by PD-1 ligation, including cytokine production, $Ca^{2+}$ flux, cytoskeletal rearrangements, cytolosis, migration and metabolic machinery, suggests there are mechanisms in addition to phosphatase recruitment that function to inhibit T cell activation[14–20]. This is supported by findings that suggest SHP2 deficiency in mice does not recapitulate full PD-1 KO[51]. Moreover, the cytoplasmic tail of PD-1 has not been studied for additional signaling motifs or phosphorylation sites that may contribute to its inhibitory function. Given the variable responses of cancer patients treated with PD-1 blockade, it is necessary to determine the signaling mechanisms driving PD-1 function and whether targeting a specific motif may confer therapeutic benefit[24–26,47].

PD-1 is one of over 100 receptors in immune cells and some nonhematopoietic cells that contain ITIM or ITSM sequences[149,150]. The signaling outputs derived from phosphorylation of these motifs vary drastically despite recruitment of similar mediators[3,149,150]. In general, ITIMs, or inhibition motifs, govern inhibitory signaling through the recruitment of SH2-containing phosphatases that dephosphorylate effector proteins that drive activation[3,48,149]. Receptors containing ITSMs, or switch motifs, on the other hand, have been reported to alter their function based on the specific mediators binding to phospho-tyrosine[3,48]. LY108 (Slamf6), 2B4 and other SLAM receptors, for example, bind to signaling lymphocytic activation molecule-associated protein SAP (SH2D1A), which associates with the ITSM to block phosphatase binding and promote positive signaling[3,151]. However, in the absence of SAP, this family of receptors uses their ITSM to bind SHP1/SHIP1 phosphatases that promote negative signaling, signifying that a single receptor can function as both a costimulatory or coinhibitory receptor[3,151]. In addition, the phosphorylation of immune-tyrosine activation motifs, or ITAMS, found on the TCR, B-cell receptor (BCR), and numerous costimulatory receptors, drives activation machinery in immune cell subsets that is subsequently dampened by the ligation of receptors containing ITIM and ITSM sequences[150]. While there is considerable overlap in the types of

motifs comprising the cytoplasmic tails of immunoreceptors to promote signaling, their functions significantly diverge. Moreover, the promiscuity of signaling mediators recruited to the cytoplasmic tail of immunoreceptors makes it difficult to distinguish how specific motifs function to preferentially impact downstream pathways, adding to our lack of clarity. For these reasons, our studies relied on PD-1 mutant mouse models and proteomic methodology to uncouple the function of the ITIM and ITSM, and other potential signaling motifs.

*In vitro* analyses of ITIM and ITSM mutated T cells suggest that the ITSM is the primary signaling motif driving PD-1-mediated inhibition[14,48,148]. These published studies were performed exclusively *in vitro* and only assessed functional impact on total CD4$^+$ T cells[48,148]. To more closely examine the role of each motif in regulating PD-1 inhibitory signals in multiple immune cell subsets, we generated PD-1 mutant mouse strains with a single amino acid change, tyrosine to phenylalanine, in the ITIM and ITSM, to assess how preventing signaling through each motif impacts T cell responses in tumors *in vivo*[14,15,148]. We found that mice harboring this mutation in the ITSM resulted in enhanced CD8$^+$ T cell-mediated tumor clearance, similar to genetic deficiency of PD-1 (KO), with an increase in both CD8$^+$ and CD4$^+$ effector T cell responses. Conversely, mutation of the ITIM did not control tumor burden, similar to responses observed in WT mice, and did not enhance CD8$^+$ nor CD4$^+$ effector T cell responses.  Interestingly, however, ITSM mutant mice do not clear tumors as efficiently as PD-1 KO mice, suggesting that there is residual function controlled by the ITIM or an uncharacterized signaling motif.

Confirming the necessity of the ITSM in regulating cancer pathogenesis *in vivo* lead us to explore various proteomic methods to specifically identify how each motif regulates downstream signaling. Using PD-1 WT, KO, ITIM and ITSM mutant CD8$^+$ T cells for Reverse Phase Protein Array (RPPA) analysis and phospho-flow cytometry, we assessed and validated differences in characterized TCR signaling pathways that are known to be inhibited by PD-1 ligation[17,152]. We then used proximity phospho-proteomics to assess changes in membrane dynamics and protein recruitment to the cytoplasmic tail of PD-1 mutants while correlating this behavior to changes in phosphorylation. To determine if observed protein recruitment resulted in a direct binding interaction with PD-1 ITIM or ITSM mutants, we performed phospho-peptide pulldowns with

peptides corresponding to the ITIM, ITSM and novel phosphorylated serine residues identified on the cytoplasmic tail of PD-1. Finally, we developed *in vivo* PD-1-APEX2 proximity labelling to monitor specific signaling alterations among various immune cell subsets *in vivo* that can be applied to PD-1 mutant constructs. Together, these data not only corroborate previous findings, but elucidate unique roles for the ITIM and ITSM in different disease contexts and identify potentially novel mechanisms of PD-1-mediated function.

## 3.2 Results

*ITIM and ITSM mutant phenotypes in cancer*

Previous studies have found that singly mutating the ITIM or ITSM on PD-1 *in vitro* results in different signaling outputs that regulate specific T cell functions downstream. Multiple studies report that the ITSM motif governs the majority of PD-1-mediated inhibition, while the main function of the ITIM remains largely uncharacterized. We hypothesized that these observed differences would translate to unique pathogenic responses *in vivo* in the context of cancer. We first compared how PD-1 ITIM and ITSM mutant mice controlled tumor growth compared to PD-1 WT and KO mice. Mice were implanted with PD-1 blockade-responsive MC38 tumor cells or less immunogenic B16-OVA melanoma cells and monitored for tumor growth[22]. PD-1 ITSM and KO mice similarly cleared tumors in the B16-OVA model, however, PD-1 KO mice cleared significantly more tumors in the MC38 model compared to ITSM mutant mice (Figure 3.1a-b). Conversely, the ITIM mutant tumor growth phenotype resembled that observed in WT PD-1 mice in both tumor models. Although the ITSM mutation significantly improved overall survival in the MC38 model compared to WT and ITIM mutant mice, survival was still significantly decreased compared to PD-1 KO mice (Figure 3.1c). Similarly, ITSM mutant mice exhibited improved survival compared to PD-1 WT and ITIM mutant mice bearing B16-OVA tumors and this survival was not significantly different compared to PD-1 KO mice (Figure 3.1d). WT and ITIM mutant mice showed similar survival in both MC38 and B16-OVA models (Figure 3.1 c-d). The differences observed in tumor growth and survival between MC38 and B16-OVA ITSM-tumor bearing mice may be due in part to the amount of tumor cells injected for each model ($1 \times 10^6$ MC38 cells and $3 \times 10^5$ B16-OVA cells). The greater number of implanted MC38 tumor cells likely induced more rapid tumor growth that could not be as efficiently controlled by the immune compartment.

While these data suggest that loss of signaling from the ITSM motif alone is sufficient to recapitulate the phenotype of enhanced tumor growth control and survival associated with total PD-1 loss, it is important to note that ITSM mutant mice were not as efficient at controlling tumor growth or enhancing survival compared to PD-1 KO mice. For this reason, it is likely that the ITIM or an uncharacterized signaling motif plays a role in PD-1-mediated inhibition.

*ITSM-mutant CD8+ TILs are more abundant and cytotoxic*

To better characterize the mechanism of tumor clearance, we analyzed TILs *ex vivo* for T cell subset and cytotoxicity markers. We isolated TILs on day 10 post MC38 tumor implantation from PD-1 WT, KO, ITSM and ITIM mutant mice. We observed an increased frequency of CD8+ T cells and reduced frequency of Foxp3+ Treg cells in the tumors of ITSM mutant and KO mice compared to WT and ITIM mutant mice, resulting in an increased CD8+/Treg cell ratio (Figure 3.1e,g-h). The frequency of Foxp3- Tcon cells also was increased in ITSM mutant and KO mice compared to WT and ITIM mice (Figure 3.1f). These data suggest that increased CD8+ TILs and decreased Treg cell numbers in the tumor are driving decreased tumor burden observed in the ITSM mutant mice, similar to PD-1 KO mice.

To characterize the cytotoxic capacity of CD8+ T cells, we examined expression of cytotoxicity-associated markers *ex vivo*. The frequency of perforin-expressing CD8+ TILs isolated from ITSM mutant and PD-1 KO mice was significantly increased compared to WT and ITIM mutant mice (Figure 3.1i). The frequency of granzyme B-expressing CD8+ TILs was significantly elevated in PD-1 KO mice compared to WT, while ITSM and ITIM mutant mice trended toward producing more granzyme B than WT mice, though these results were not significant (Figure 3.1j). We stimulated TILs *in vitro* with CD3/CD28 crosslinking antibodies to assess cytokine production and found increased frequencies of TNF$\alpha$-producing PD-1 KO and ITSM mutant CD8+ TILs compared to WT and ITIM mutant CD8+ TILs (Figure 3.1k). We also observed a trend toward increased frequencies of IFN$\gamma$-producing CD8+ TILs in PD-1 KO and ITSM mutant mice compared to WT and ITIM mutant mice. These data suggest that both ITSM and KO mice control tumor growth and clear tumor more effectively due to an increased presence of highly cytotoxic CD8+ effector T cells.

Complementary studies spearheaded by a previous graduate student in the Sharpe lab further demonstrated that CD8^{+} T cells are the main effectors of tumor-associated phenotypes in ITIM and ITSM mutant mice using antigen-specific CD8^{+} T cell adoptive transfer studies in B16-OVA-bearing mice and CD8^{+} T cell depletion studies in MC38-tumor bearing mice (data not shown, under review). Together, these data corroborate previous *in vitro* work indicating the ITSM is the primary mediator of PD-1 inhibition. Still, differences observed between PD-1 KO and ITSM mutant mice as well as between WT and ITIM mutant mice indicate that further work is needed to define additional mechanisms necessary for optimal PD-1 signaling.
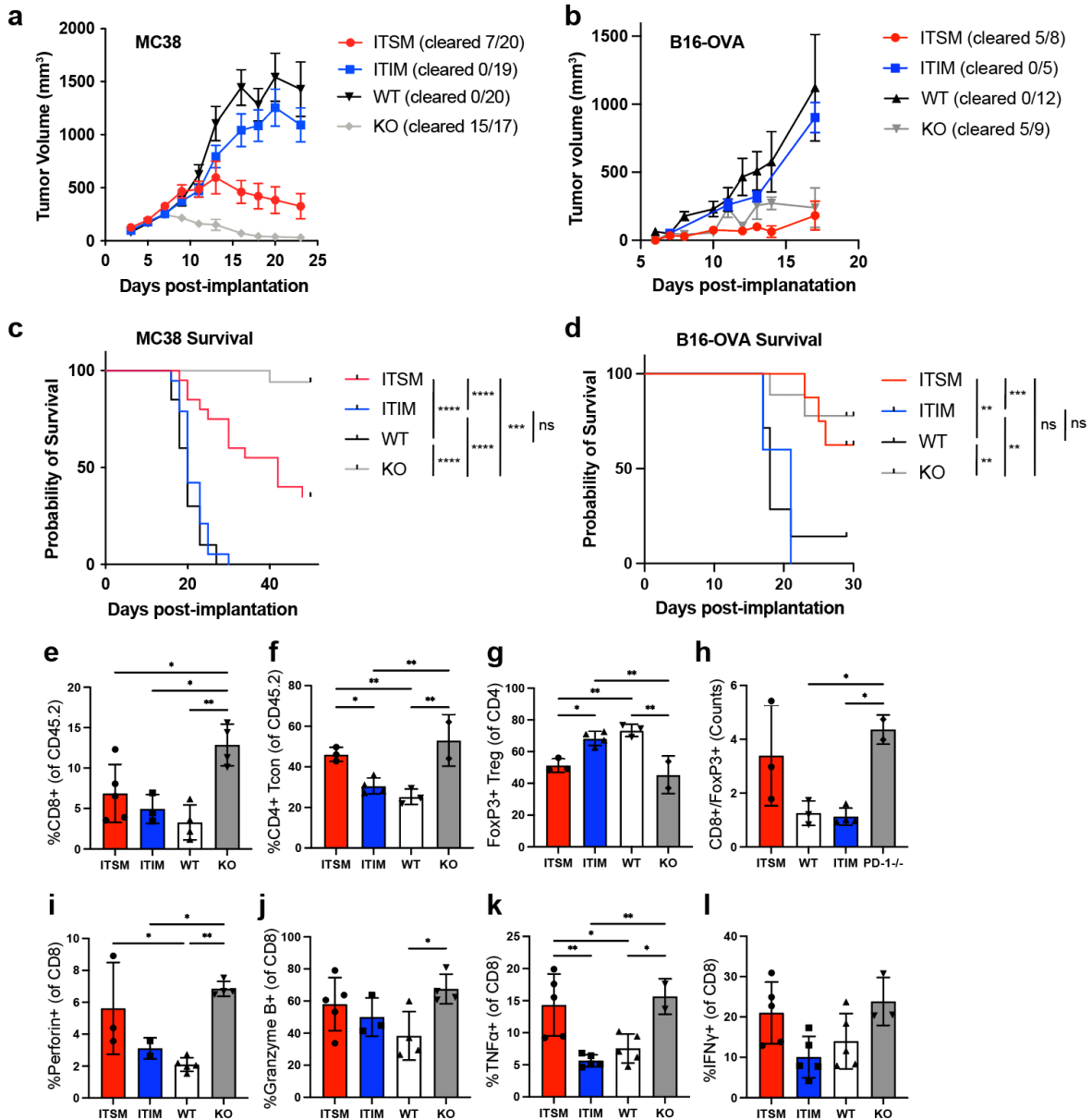
**Figure 3.1: ITIM and ITSM mutant mice differentially respond to cancer.** Tumor growth in PD-1 WT, KO, ITIM and ITSM mutant mice implanted with a) $1\times10^6$ MC38 or b) $3\times10^5$ B16-OVA tumor cells. Data are presented as means of n=5-20 ± SD and tumor clearance is reported for each group. Survival analysis of c) MC38 and d) B16-OVA tumor-bearing mice from tumor experiments displayed in a) and b). Data are presented as means of n=5-20 ± SD and statistical significance was assessed using the Log-rank Mantel Cox test. Frequencies of e) CD8^{+} f) CD4^{+} Tcon and g) FoxP3+ Treg cells and h) CD8^{+}/Treg ratios of TILs isolated from MC38 tumors on day 10 post-implantation. Frequencies of i) perforin and j) granzyme B in CD8^{+} TILs isolated from MC38 tumors on day 10 post-implantation. CD8^{+} TILs stimulated *ex vivo* with crosslinking CD3/CD28 antibodies and assessed for frequencies of k) TNFα and l) IFNγ. Data are presented as means of n=2-5 ± SD. Statistical significance was measured using one-way ANOVA. * p<0.05, ** p<0.01, *** p<0.001, **** p<0.0001. *Data generated by Juhi Kuchroo, MD PhD.*

*TCR-mediated signaling pathways impacted by ITIM and ITSM mutations*

Our *in vivo* tumor studies emphasized a more potent role for the ITSM in mediating PD-1 inhibition compared to the ITIM. To address phenotypic differences observed in ITIM and ITSM mutant mice, we assessed phosphorylation changes in proximal TCR-mediated signaling pathways to determine if specific pathways are targeted by either motif. We initially chose an unbiased approach to identify signaling players impacted by mutation of the ITIM and ITSM. We prepared samples for a Reverse Phase Protein Array (RPPA) assay performed at the MD Anderson Cancer Center[152]. The RPPA core at MD Anderson assesses cell lysates for changes in protein levels of approximately 500 proteins and phospho-proteins involved in signaling cascades[152]. We isolated naïve CD8$^+$ T cells from spleen and lymph nodes and stimulated them overnight in plates coated with CD3/CD28 crosslinking antibodies to induce PD-1 expression. Stimulated CD8$^+$ T cells were then incubated with TCR-PD-L1 beads overnight using methods outlined in Chapter 2.4. Following bead treatment, cells were lysed and sent to the RPPA Core at MD Anderson where antibodies were used to assess relative protein levels.

Preliminary data demonstrated that several of the most significantly altered proteins upon PD-L1 engagement of PD-1 included phosphorylated members of the PI3K-AKT and MEK-ERK pathways. Phosphorylation of S6 and mTOR, which are downstream mediators of AKT signaling, was increased with defective PD-1 signaling in either KO, ITIM or ITSM mutant CD8$^+$ T cells, compared to WT CD8$^+$ T cells that contain a functional PD-1 immunoinhibitory pathway (Figure 3.2a,e). While MAPK phosphorylation was also increased in PD-1 KO, ITIM and ITSM mutants, the increase in ITIM mutant CD8$^+$ T cells was more subtle, suggesting a potential difference in ITIM and ITSM signaling (Figure 3.2b). RPPA analysis also examined two activating phosphorylation sites on AKT. Interestingly, levels of pS473 on AKT were elevated in KO mice, but remain similar in ITSM and WT mice, while levels of pT308 on AKT were elevated in both KO and ITSM mice compared to WT mice (Figure 3.2c-d). These findings suggest that the ITSM may regulate specific phosphorylation sites on AKT that affect the activation of downstream mediators of AKT signaling, including S6 and mTOR. ITIM mutant CD8$^+$ T cells demonstrated decreased phosphorylation in both activating AKT phospho-sites, indicating another potential node of differential signaling between the ITIM and ITSM (Figure 3.2c-d). However, because complete knockout of PD-1 shows the greatest defect

overall in dephosphorylation mediated by PD-1 compared to the ITSM, the role of the ITIM or an uncharacterized signaling motif cannot be excluded. As described above, the similar trends in phosphorylation status of TCR signaling mediators between the KO and ITSM suggest that the majority of regulation is likely via the ITSM motif. In addition, increased phosphorylation of mTOR in ITSM mutant CD8+ T cells compared to PD-1 KO and ITIM CD8+ T cells may suggest that the ITSM primarily regulates mTOR dephosphorylation compared to the ITIM and perhaps a compensatory mechanism is triggered to regulate mTOR dephosphorylation with total PD-1 loss (Figure 3.2e).

We validated the findings from RPPA using phospho-flow cytometry analysis. We stimulated naïve CD8+ T cells with crosslinking CD3/CD28 antibodies. The cells were then rested overnight and restimulated with TCR-PD-L1 beads at short timepoints to capture the fast kinetics of phosphorylation following TCR stimulation and PD-1 ligation. We observed significant changes in phosphorylation status of the different TCR signaling mediators at different timepoints (Figure 3.2f-i). Interestingly, we observed differences in signaling in PD-1 KO CD8+ T cells compared to ITSM mutant T cells in the separate signaling arms of the TCR cascade. There is no increase in ERK phosphorylation in ITSM mutant CD8+ T cells immediately following TCR stimulation, compared to KO CD8+ T cells, suggesting that the ITIM may play a role in regulating ERK phosphorylation early on following TCR and CD28 engagement (Figure 3.2g). In contrast, S6 phosphorylation in PD-1 KO, ITIM and ITSM mutant CD8+ T cells was increased compared to WT CD8+ T cells, as observed in our RPPA analysis (Figure 3.2f). We assessed phosphorylation of ZAP70, a receptor tyrosine kinase that drives TCR-mediated signaling and is dephosphorylated upon PD-1 ligation[15,153]. As expected, we observed significantly more phosphorylation in PD-1 KO cells compared to PD-1 WT, ITIM and ITSM mutant cells, though ITSM mutant cells display more phosphorylation compared to WT, indicating a role for the ITSM in mediating ZAP70 dephosphorylation (Figure 3.2i). Additionally, we did not observe significant differences in AKT-pS473 between ITSM, ITIM and WT CD8+ T cells at early timepoints, similar to our RPPA analysis (Figure 3.2h). Nevertheless, these data imply that the ITSM and ITIM differentially regulate specific pathways downstream of the TCR/CD28 signaling cascade.

Our preliminary analyses highlight the impact of the ITSM and ITIM on specific pathways downstream of PD-1 but require further experimentation to examine distinct activating and inactivating phosphorylation sites on target proteins. We also appreciate that the signaling pathways evaluated in these studies are regulated by a variety of different immunoreceptors and stimuli. Such crosstalk may convolute findings if these pathways are up or downregulated as a compensatory mechanism in response to loss of PD-1 signaling motifs. As a result, we have employed more targeted proteomic methods to further elucidate how the ITIM and ITSM impact downstream signaling pathways by recruiting specific effector proteins.
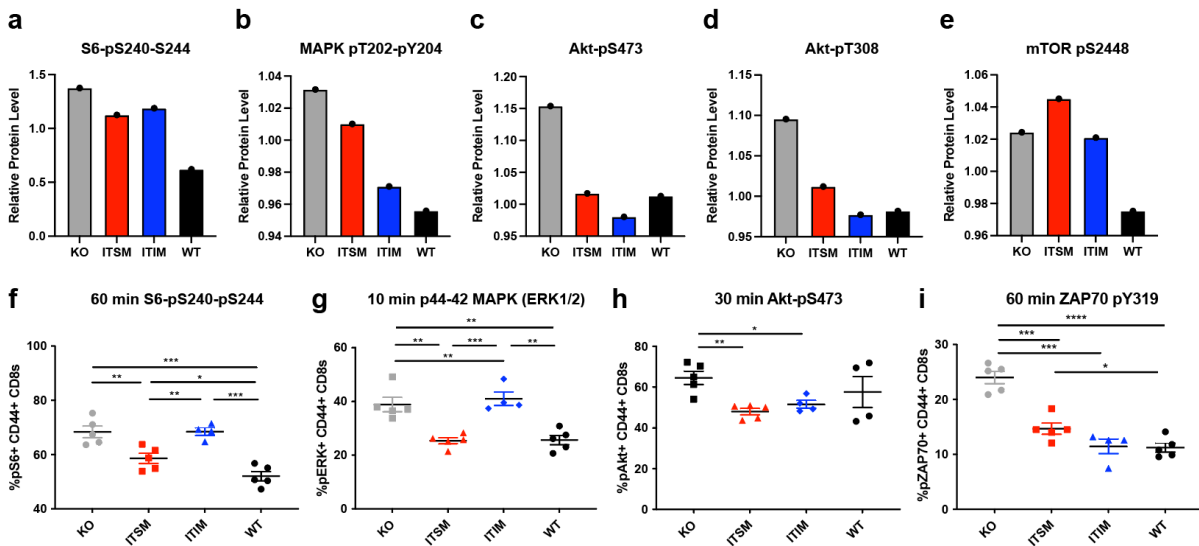


**Figure 3.2: ITIM and ITSM impact on TCR-mediated signaling pathways.** RPPA analysis of murine CD8+ T cells isolated from PD-1 mutant, WT or KO mice and stimulated with TCR-PD-L1-containing beads for 24 h to assess phosphorylation changes in a) S6-pS240-S244, b) MAPK pT202-pY204, c) AKT-pS473, d) AKT-pT308, and e) mTOR-pS2448 pathways. Data are reported as relative protein levels (y-axis) and statistical significance was not calculated on one replicate per condition for pilot experimentation. Frequencies of f) pS6-pS240-pS244, g) p44-42 MAPK, h) pAKT-pS473, and I) ZAP70 pY319 in CD8+ T cells stimulated with PD-L1-containing beads and assessed by phospho-flow cytometry. Data are presented as means of n=4-5 ± SD. Statistical significance was measured using Student's unpaired t-test. * $p<0.05$, ** $p<0.01$, *** $p<0.001$, **** $p<0.0001$.

*PD-1 mutant-APEX2 proximity labelling identifies unique protein recruitment patterns in ITIM and ITSM*

To determine the specific proteins regulating the differential signaling outcomes observed in ITIM and ITSM mutant mice, we designed PD-1 ITIM and ITSM single mutant APEX2-expressing Jurkat cells for proximity labelling analysis, described in Chapter 2.2. We performed a 16-plex proximity labelling experiment assessing 5 and 20 min timepoints to compare PD-1 WT and mutant constructs expressed in Jurkat cells and stimulated with TCR-control or TCR-PD-L1 beads using methods outlined in Chapter 2.4. In alignment with the literature, we found complete ablation of SHP2 recruitment to ITSM-mutated PD-1, while ITIM-mutated PD-1 retained SHP2 association (Figure 3.3a). We also observed that the majority of SHP1 peptides were identified in WT and ITIM-mutant conditions, suggesting that the ITSM likely drives phosphatase recruitment, though the distinct roles of SHP2 and SHP1 in mediating PD-1 inhibitory signals remain unclear (Figure 3.3a-b)[14,48,51].

Our data and previous studies have proven that the ITSM recruits tyrosine phosphatases to attenuate TCR-mediated signaling pathways (Figure 3.3a-b). However, the role of the ITIM has not been elucidated. The ITIM is minimally required for phosphatase recruitment and both motifs are necessary for disrupting stable contacts at the immune synapse[19]. While PD-1 clustering at the immune synapse was not significantly different among PD-1 WT, single mutant and double mutant cells, ITIM and double mutant cells appear to have more diffuse clustering with TCR components at the immune synapse[19]. We assessed TCR components in our proximity labelling experiment to determine if mutation in the ITIM altered colocalization with key immune synapse components. Interestingly, we found that both single ITIM and ITSM mutations exhibited less colocalization with CD28, CD3ε, CD3δ, CD3γ and ZAP70, though mutation in the ITIM showed the greatest decrease in colocalization with T cell activation proteins (Figure 3.2c-g)[15,16]. It is also important to note that colocalization was diminished in both TCR-control and PD-L1-ligated conditions, suggesting that PD-1 clustering at the immune synapse occurs upon TCR stimulation in the presence or absence of PD-1 ligation (Figure 3.2c-g). Still, these data suggest a potential defect in PD-1 clustering at the immune synapse driven primarily by the ITIM motif.

Given our previous findings highlighting a robust recruitment of PIEZO1 to PD-1 over time, we assessed whether this association was regulated by the ITIM or ITSM (Chapter 2.2). Interestingly, we found that ligation of PD-1 induced PIEZO1 recruitment despite mutations in either motif, though recruitment in the WT and ITIM-mutant conditions are slightly lower than the ITSM mutant (Figure 3.3h). These data suggest that the ITIM may play a minor role in PIEZO1 localization or that PD-1-PIEZO1 association is independent of known PD-1 signaling motifs and relies on a novel signaling site. Moreover, we observed robust recruitment of ubiquitin ligase WWP1 in ITIM-mutated cells at baseline and 5 min that significantly decreased at 20 min (Figure 3.3i). These data coincide with our previous findings of PIEZO1 co-IP with WWP1 following PD-1 ligation. Interestingly, the robust enrichment of WWP1 that decreases over time in ITIM mutant conditions indicates a role for the ITSM in recruiting WWP1 even prior to PD-1 ligation. The dissociation of WWP1 proximal to the cytoplasmic tail of PD-1 may be regulated by the ITIM since we do not capture this association in WT and ITSM mutant conditions.

To further investigate a potential function for the ITIM, we assessed recruitment kinetics of proteins that were retained in ITSM-mutated cells but diminished in ITIM-mutated cells. We observed increased recruitment of ubiquitin-ligase Cbl-b and corresponding binding partners UBASH3A (STS-2) and UBASH3B (STS-1) in ITSM-mutated cells driven by PD-1 ligation that was reduced in ITIM-mutated cells (Figure 3.3j-l)[154–156]. Interestingly, Cbl-b and UBASH3A exhibited very similar recruitment kinetics, where association with PD-1 was augmented upon PD-L1 ligation in the ITSM mutant compared to the ITIM, suggesting that the ITIM may recruit these proteins for effector function (Figure 3.3k-l). Alternatively, UBASH3B exhibited the greatest increase in recruitment with TCR stimulation alone in WT cells which was abrogated in ITIM mutant cells (Figure 3.3j). These findings are intriguing in that Cbl-b, UBASH3A and UBASH3B are negative regulators of T cell activation and interact with one another to induce ubiquitin-mediated proteasomal degradation, while UBASH3B also exhibits phosphatase activity[154,155,157,158]. It is possible that recruitment of this complex drives the degradation of TCR effector proteins that are inactivated upon PD-1 ligation.
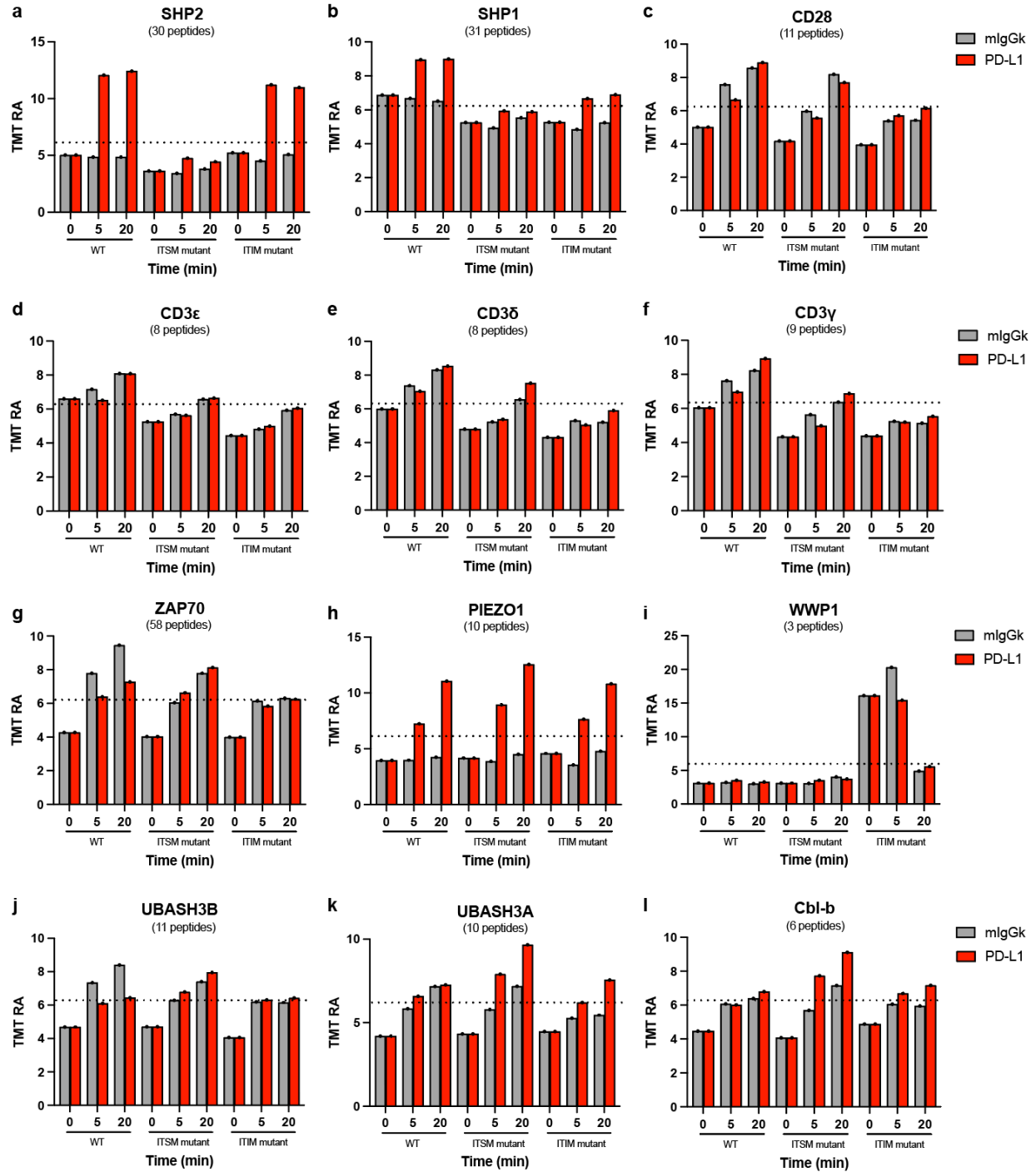
**Figure 3.3: PD-1 mutant APEX2 proximity labelling time course.** TMT ratios (TMT RA, y-axis) of a) SHP2, b) SHP1, c) CD28, d) CD3ε, e) CD3δ, f) CD3γ, g) ZAP70, h) PIEZO1, i) WWP1, j) UBASH3B, k) UBASH3A, and l) Cbl-b treated with TCR-control or PD-L1-containing beads for 5 and 20 min. Data were normalized to total protein and statistical significance was not calculated for one replicate per condition. Dotted line represents the value of TMT ratios when no change in recruitment is observed across conditions.

*PD-1-APEX2 proximity phospho-proteomic analysis*

While proximity labelling highlights colocalization around the APEX2 probe, enzyme activity and pathway activation through post-translational modification are not captured[102,103]. Thus, proteins may be migrating to specific locations, yet we are unable to determine whether or not this localization is due to an activating phosphorylation event. This is specifically important for transmembrane receptor signaling, which is often induced by activating phosphorylation events following ligation to trigger downstream signaling. For this reason, we performed proximity phospho-proteomics to assess changes in phosphorylation, thereby providing additional information about signaling pathways that become activated or inactivated upon PD-1 ligation (manuscript in prep). Differing from global phospho-proteomics performed on entire cell lysates, proximity phospho-proteomics identifies phosphorylation events within an enriched protein population (manuscript in prep). Our PD-1-APEX2 experiments, for example, enrich for proteins that are biotinylated around the APEX2 labeling radius. Using this enriched pool of peptides, we can then perform immobilized affinity chromatography (IMAC), sealed with $C_{18}$ reversed phase chromatography matrix material, that uses positive charges to trap and enrich for negatively charged phosphorylated proteins in multiplexed proteomic samples (Chapter 3.4 Methods, manuscript in prep). This method is complementary to proximity labelling in that only proteins of interest are assessed for phosphorylation changes among different conditions, rather than evaluating unrelated global phosphorylation events. Here, we used proximity phospho-proteomics to correlate protein recruitment behavior with phosphorylation changes in the presence and absence of PD-1 ligation using both murine and human PD-1 constructs. Given that phosphorylation sites are difficult to capture in an enriched protein population, we focused on dephosphorylation events that align with PD-1-mediated inhibition in the literature in addition to assessing novel phosphorylation patterns.

Using proximity phospho-proteomics in our WT human PD-1-APEX2 time course, we detected multiple phosphorylation sites that align with characterized TCR-mediated signaling events inhibited by PD-1 ligation. We observed significant enrichment of SHP2 pY584 over time following PD-1 ligation compared to TCR-control beads, which facilitates binding to adaptor protein GRB2 and confirms PD-1-mediated activation of SHP2 (Figure 3.4a)[14,159]. We also observed decreases in CD3ζ ITAM pY111 and TCR-mediated phosphatidylinositol (3,4,5)-triphosphate (PIP3) pathway proteins PKC pT536 and PLCγ pS1248

upon PD-L1 ligation compared to control stimulation, verifying that PD-1 ligation induces dephosphorylation of components in the TCR signaling cascade (Figure3.4b-d)[15,17,54]. In addition to dephosphorylation of TCR effector proteins, we also noticed decreased phosphorylation of capping protein regulator and myosin 1 linker 2 protein CARMIL2 upon PD-1 ligation compared to TCR-control conditions (Figure 3.4e). CARMIL2 is essential for CD28 costimulation and promotes actin polymerization at the immune synapse through binding of the actin-related protein 2/3 (Arp2/3) complex[160,161]. Loss of function mutations in CARMIL2 results in immunodeficiency marked by a lack of Treg cells, defective CD28 signaling and impaired cytoskeletal dynamics[161]. These findings are intriguing given our studies outlined in Chapter 2 regarding PD-1 regulation of actin cytoskeletal rearrangements and PIEZO1 activity (Figure 2.1). It is possible that PD-1 targets actin cytoskeletal machinery from the Arp2/3/CARMIL2 complex to disrupt PIEZO1 activation and TCR-mediated signaling at the immune synapse.

While we did not capture PD-1 tyrosine phosphorylation sites in this experiment, we did identify a novel serine phosphorylation site on the C-terminal tail of PD-1. We found that PD-1 pSer261 increased immediately upon PD-1 ligation compared to control conditions (Figure 3.4f). When we repeated this experiment with a murine PD-1-APEX2 construct, we again identified PD-1 pSer267 phosphorylation increasing over time following PD-1 ligation compared to TCR controls, which differs slightly from the human residue given differences in human and murine sequence homology (Figure 3.5a). In addition, we were able to capture PD-1 pY-ITIM phosphorylation and a second novel phospho-serine (pS-ITIM) two residues upstream of pY-ITIM (Figure 3.5b-c). Both ITIM-associated phospho-sites were strongly induced following PD-1 ligation compared to TCR-treated controls (Figure 3.5b-c). Encouragingly, PD-1 pulldown experiments in murine EL4 lymphoma cells stimulated with TCR-control or TCR-PDL-1 beads also showed an increased in phospho-serine in PD-L1 treated conditions using Western blot analysis (data not shown). While the precise serine site could not be ascertained in Western blotting analysis, confirmation of serine phosphorylation on PD-1 using an alterative method increased our confidence in the results. These findings imply that PD-1 contains uncharacterized signaling motifs that need to be studied further.

**Figure 3.4: Proximity phospho-proteomics from human PD-1-APEX2 time course.** TMT ratios (TMT RA, y axis) of phosphorylated peptides a) SHP2 pY584, b) CD3ζ pY111, c) PKC pT536, d) PLCγ pS1248, e) CARMIL2 pS1423 and f) PD-1 pS261 identified from proteins enriched in PD-1-APEX2 time course experiments treated with TCR-control or TCR-PD-L1 beads. Data are normalized to endogenously biotinylated acetyl-CoA carboxylase-1 (ACACA) and statistical significance was not calculated for one replicate per condition.

Additional phosphorylation events identified in the murine PD-1-APEX2 time course aligned with findings in the human PD-1-APEX2 time course. We again observed robust increases in SHP2 pY584, as well as its second activating phosphorylation site pY586, which also facilitates binding to GRB2 (Figure 3.5d-e)[159]. We detected decreases in phosphorylation on CD3ζ ITAM, PLCγ and CARMIL2 residues similar to those identified in the human PD-1-APEX2 experiments (Figure 3.5f-h). These findings not only validate previous findings in the literature, but unveil novel phosphorylation sites and signaling mechanisms regulated by PD-1-mediated inhibition[17,161].
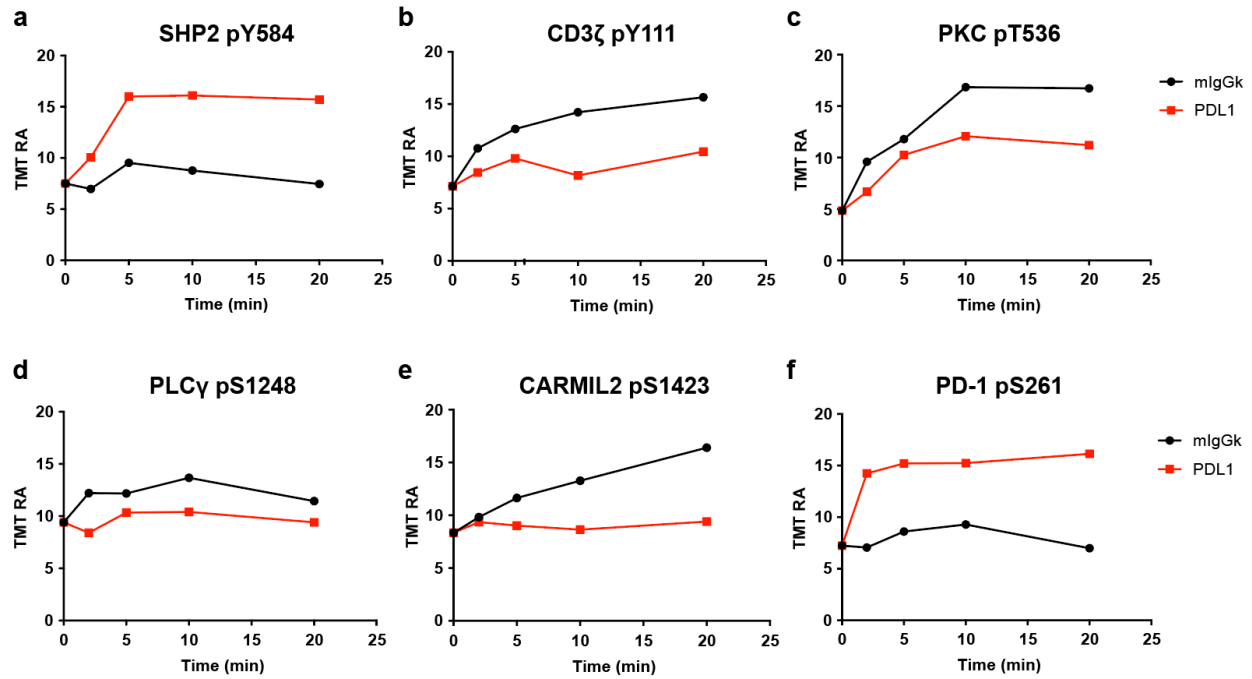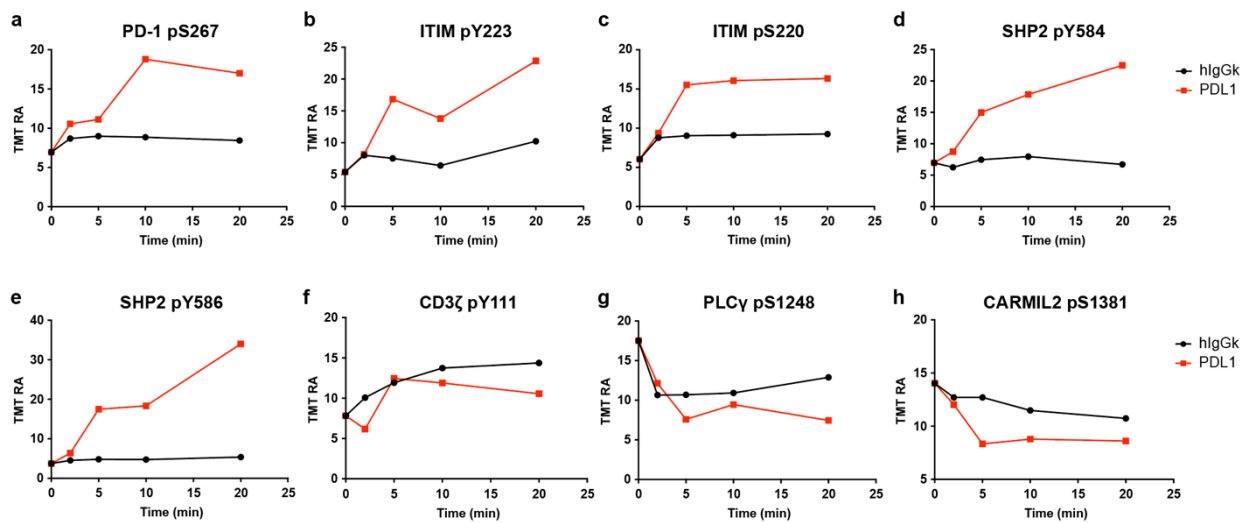


**Figure 3.5: Proximity phospho-proteomics from murine PD-1-APEX2 time course.** TMT ratios (TMT RA, y axis) of phosphorylated peptides a) PD-1 pS267, b) PD-1 ITIM pY223, c) PD-1 ITIM pS220, d) SHP2 pY584, e) SHP2 pY586, f) CD3ζ pY111, g) PLCγ pS1248, and h) CARMIL2 pS1381 identified from proteins enriched in murine PD-1-APEX2 time course experiments treated with TCR-control beads or TCR-PD-L1 beads. Data are normalized to PD-1-APEX2 bait and statistical significance was not calculated for one replicate per condition.

*PD-1 ITIM and ITSM phospho-peptide pulldown analysis*

While APEX2 proximity labelling studies enabled us to better understand membrane dynamics at the immune synapse and molecular changes occurring around the PD-1 cytoplasmic tail, we aimed to look more closely at proteins that specifically bound to phosphorylated sites on PD-1 to identify novel mediators of PD-1 inhibitory signaling. We performed phospho-peptide pulldowns in Jurkat cell lysates using phosphorylated peptide sequences corresponding to tyrosine phosphorylated ITIM (pY-ITIM) and tyrosine phosphorylated ITSM (pY-ITSM) motifs as well as phosphorylated Ser261 (pSer261) and pSer-ITIM identified in proximity phospho-proteomic studies described above with unphosphorylated peptide controls.

As anticipated, we observed a strong enrichment of SHP2, and to a lesser extent SHP1, binding to pY-ITSM that was observed only slightly in pY-ITIM, confirming the role of the ITSM as the primary recruiter of effector phosphatases (Figure 3.6a-b)[14,48]. GRB2 was also most highly enriched in pY-ITSM pulldowns, in agreement with our phospho-proteomic data indicating that SHP2 becomes phosphorylated on GRB2 binding sites (Figure 3.6c and Figure 3.5d-e)[159]. We also observed both pY-ITIM and pS-ITIM interacting with GRB2 compared to unphosphorylated control peptides (Figure 3.3c). While these increases were not significant, it is possible that GRB2 binds additional PD-1 mediators specifically recruited by the ITIM given the binding promiscuity of GRB2[162]. Furthermore, while there is substantial spread in the pY-ITSM replicates, we found that CSK and ZAP70 exhibited similar patterns of binding to pY-ITSM peptides compared to non-phosphorylated peptide controls (Figure 3.6d-e). CSK is a repressive kinase that targets inhibitory phosphorylation sites on TCR effector kinases, such as LCK, which is responsible for activating ZAP70 on CD3$\zeta$ ITAMs[15,153,163,164]. Our findings corroborate previous reports of CSK associating with the pY-ITSM following peptide pulldowns and verifies that the ITSM recruits CSK to target proximal TCR signaling mediators[15]. We also detected minimal binding of phosphorylated ITIM motifs to ZAP70 and CSK, but more replicates are necessary to determine if this association is functional (Figure 3.6d-e). It is possible that CSK phosphorylates LCK to prevent sustained ZAP70 phosphorylation and activation, while recruitment of SHP2 may directly dephosphorylate activated ZAP70[15,153,163].

Finally, we observed a strong enrichment of SH2D1A (SAP) binding to pY-ITSM compared to other phosphorylated and unphosphorylated peptides (Figure 3.6f). Affinity purification mass spectrometry has demonstrated that SH2D1A binds to PD-1 and is believed to block PD-1 function through indirect inhibition of SHP2[50]. These reports are intriguing in that they introduce a negative feedback mechanism that dampens PD-1 inhibition through SHP2 regulation[50]. Overall, our findings strengthen evidence supporting that the ITSM functions as the primary recruiter of inhibitory phosphatases and kinases to dampen TCR signaling which, in turn, are also regulated to counter PD-1-mediated inhibition.
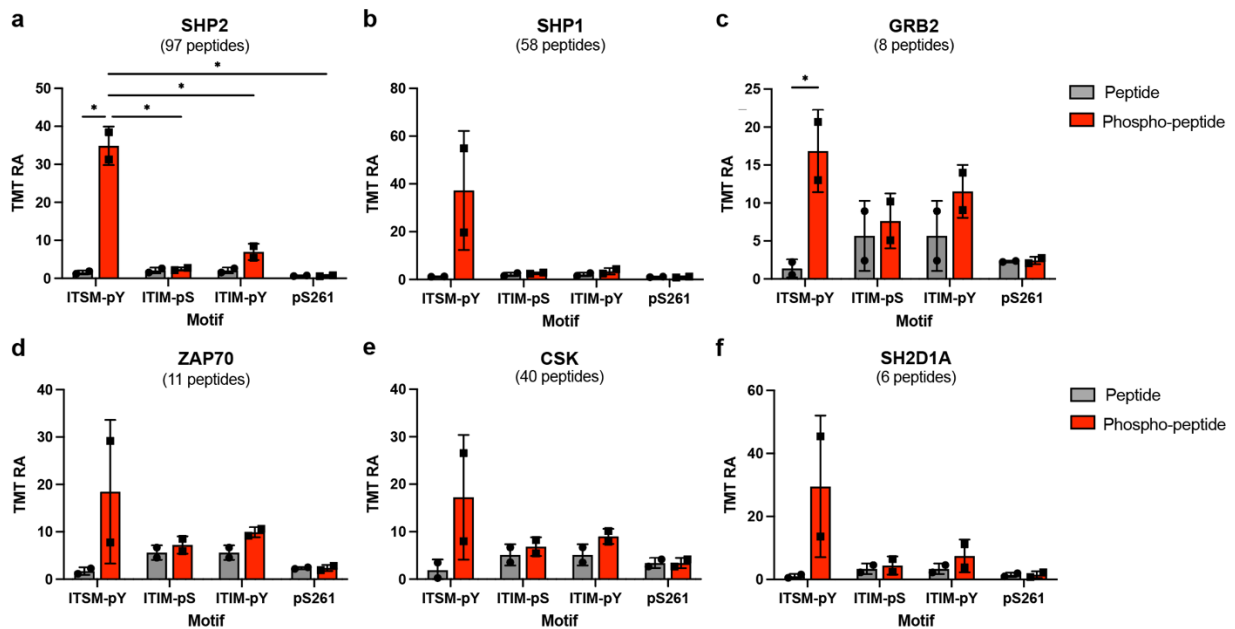


**Figure 3.6: pY-ITSM peptide binds to effector phosphatases and kinases.** TMT ratios (TMT RA, y axis) of a) SHP2, b) SHP1, c) GRB2, d) ZAP70, e) CSK and f) SH2D1A pulled down in Jurkat cell lysates using PD-1 peptides (gray) or phospho-peptides (red). Data are presented as means of n=2 ± SD. Statistical significance was measured using two-way ANOVA. * p<0.05, ** p<0.01, *** p<0.001, **** p<0.0001.

In alignment with our PD-1-mutant APEX2 findings, we observed Cbl-b, UBASH3B and UBASH3A ubiquitin ligase machinery preferentially binding to both pY-ITIM and pS-ITIM compared to unphosphorylated controls (Figure 3.7a-c). Cbl-b and UBASH3A also bound to pY-ITSM, but the large spread between replicates makes these findings difficult to interpret and require additional experimentation (Figure 3.5b-c). Our findings suggest that while the pY-ITSM primarily recruits effector kinases and phosphatases to dampen TCR-mediated signaling, the ITIM may potentially be marking these inactivated proteins for

subsequent proteasomal degradation, unveiling a housekeeping function of PD-1. For this reason, mild phenotypes observed in tumor-bearing ITIM mutant mice may be a result of inefficient degradation of proteins that have already been inactivated by the ITSM (Figure 3.1a-b). In addition, we also found that pY-ITIM, pS-ITIM and to a lesser extent pY-ITSM binds casein kinase-1 (CK1), which is constitutively expressed to maintain NFAT phosphorylation in quiescent T cells (Figure 3.7d)[165]. Perhaps CK1 is recruited to PD-1 to prevent NFAT translocation to the nucleus and subsequent downstream gene transcription of IL-2, though it is unclear which motif preferentially controls this recruitment[17,165].
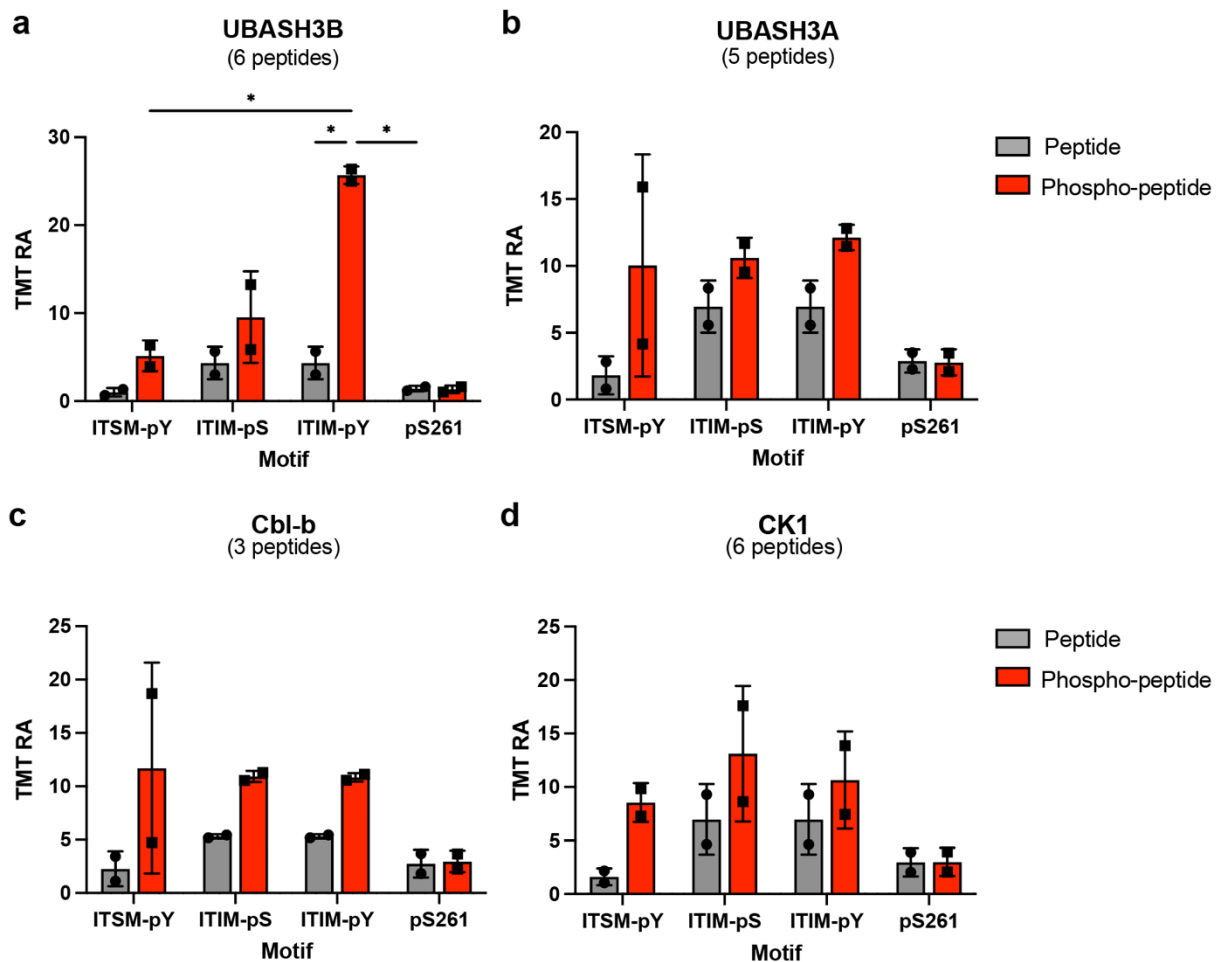


**Figure 3.7: pY-ITIM peptide binds to ubiquitin ligase machinery.** TMT ratios (TMT RA, y axis) of a) UBASH3B, b) UBASH3A, and c) Cbl-b pulled down in Jurkat cell lysates using PD-1 peptides (gray) or phospho-peptides (red). Data are presented as means of n=2 ± SD. Statistical significance was measured using two-way ANOVA. * $p<0.05$, ** $p<0.01$, *** $p<0.001$, **** $p<0.0001$.

Our proximity phospho-proteomic analysis identified two novel serine phosphorylation sites on the cytoplasmic tail of PD-1. The first identified serine is adjacent to the ITIM motif, two residues upstream of the phosphorylated tyrosine (**S**VD**Y**GEL). We hypothesized that the pY-ITIM and pS-ITIM would exhibit considerable overlap in protein recruitment given their proximity within a known signaling motif. While we did observe similar recruitment in ubiquitin ligase machinery with the pY-ITIM compared to the pS-ITIM (Figure 3.7b-c), we also identified proteins that exclusively associated with the pS-ITIM peptide. We found a significant enrichment of WASHC2A and WASHC3 peptides bound to pS-ITIM compared to unphosphorylated controls and other phosphorylated PD-1 motif peptides (Figure 3.8a-b). pY-ITIM peptides also bound these proteins compared to unphosphorylated control peptides, but to a lesser extent, again suggesting redundancy in binding between pY-ITIM and pS-ITIM phospho-sites or dependency of each site on the phosphorylation of the other. Moreover, the pS-ITIM strongly associated with AP-2 complex proteins AP2A1 and AP2B1 compared to unphosphorylated peptide controls and other PD-1 motif phospho-peptides (Figure 3.8c-d). The WASH complex mediates F-actin nucleation to promote optimal TCR signaling and receptor turnover while AP-2 adaptor proteins similarly govern clathrin-mediated endocytosis at the immune synapse[121,166–168]. These findings suggest that the pS-ITIM interferes with actin cytoskeletal dynamics and mechanisms regulating receptor turnover by perhaps sequestering WASH and AP-2 complex proteins to destabilize contact and subsequent signaling at the immune synapse.

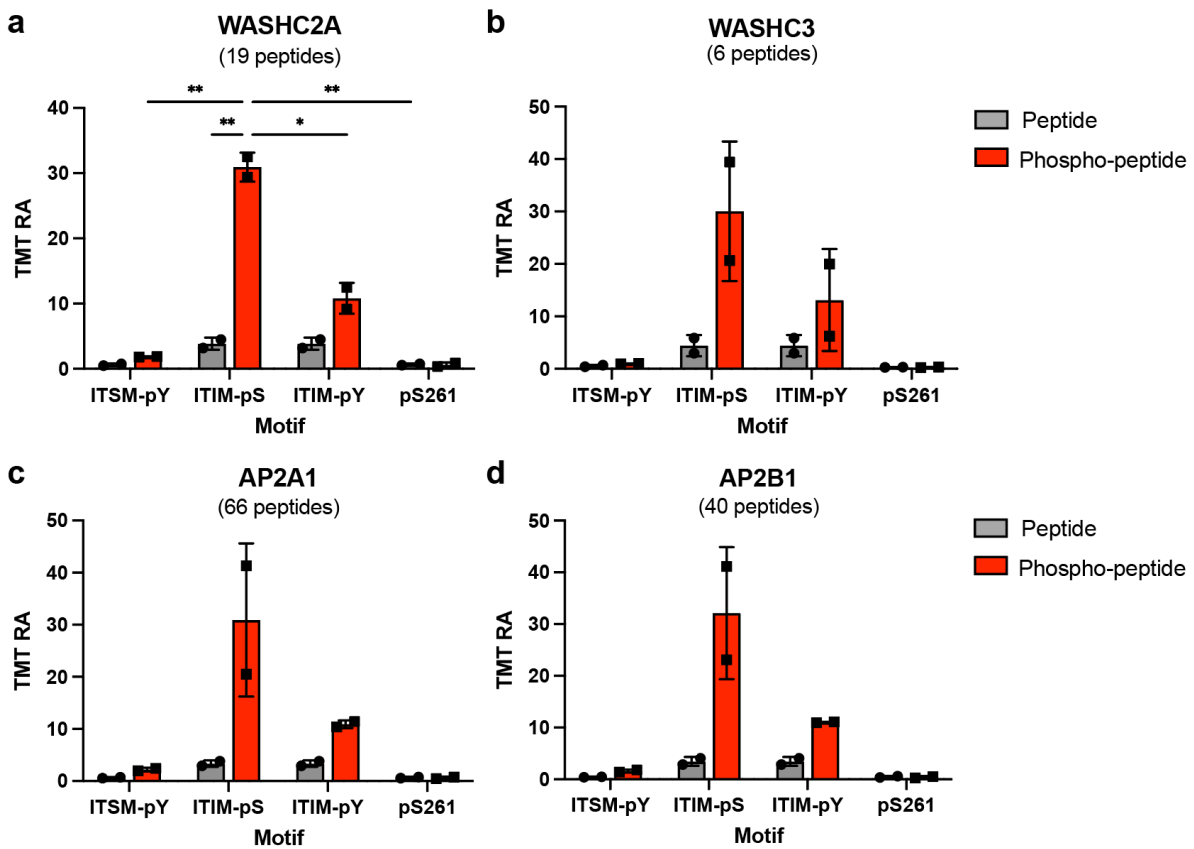**Figure 3.8 pS-ITIM peptide binds to actin remodeling and endocytic proteins.** TMT ratios (TMT RA, y axis) of a) WASHC2A, b) WASHC3, c) AP2A1 and d) AP2B1 pulled down in Jurkat cell lysates using PD-1 peptides (gray) or phospho-peptides (red). Data are presented as means of n=2 ± SD. Statistical significance was measured using two-way ANOVA. * $p<0.05$, ** $p<0.01$, *** $p<0.001$, **** $p<0.0001$.

Lastly, we assessed unique binding partners that showed preference for the second novel phosphorylated serine on PD-1, pSer261. While the majority of pulled down proteins showed limited interaction with either phosphorylated or unphosphorylated Ser261 peptides, we identified two proteins that significantly and exclusively bound the pSer261 peptide: TNKS-1 (poly [ADP-ribose] polymerase tankyrase-1) and PIN1 (peptidyl-prolyl cis-trans isomerase NIMA-interacting 1). TNKS-1 binds to telomeric protein TRF1 and poly-(ADP-ribosyl)ates it, resulting in telomeric elongation when overexpressed[169]. While it is difficult to determine why PD-1 would interact with a poly-(ADP-ribosyl)ate polymerase (PARP), it is also possible that the proline-rich region proximal to Ser261 resembles a tankyrase binding motif (TBM) that induces association with TNKS-1[169,170]. Further studies are necessary to determine whether TNKS-1 binding to pSer261 induces unique PD-1 function or is an experimental artifact. Interestingly, PIN1 has recently been implicated in driving tumor cell proliferation resulting in poor clinical outcome in multiple cancer types, including breast cancer and hepatocellular carcinoma[171,172]. PIN1 binds to phosphorylated serine or threonine residues adjacent to proline where it modifies protein function by promoting cis/trans isomerization of the peptide bond[171–173]. Since Ser261 is adjacent to a proline rich motif, it is possible that PIN1 binds to and sterically modifies PD-1 following serine phosphorylation, thereby altering PD-1 function. Additional studies are also necessary to determine the function of PIN1 in PD-1-mediated signaling.
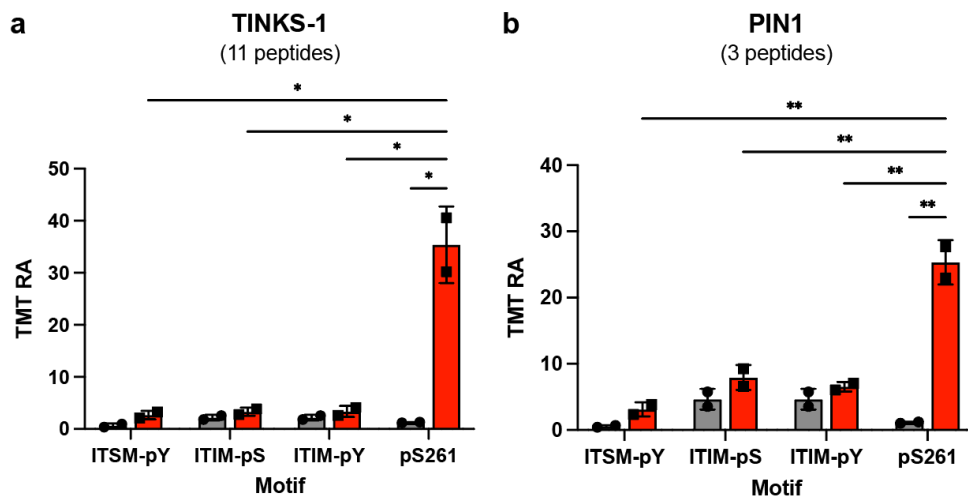


**Figure 3.9: pSer261 peptide demonstrates unique binding activity.** TMT ratios (TMT RA, y axis) of a) TINKS-1 and b) PIN1 pulled down in Jurkat cell lysates using PD-1 peptides (gray) or phospho-peptides (red). Data are presented as means of n=2 ± SD. Statistical significance was measured using two-way ANOVA. * $p < 0.05$, ** $p < 0.01$, *** $p < 0.001$, **** $p < 0.0001$.

*In vivo PD-1-APEX2 proximity labelling using chimeric immune editing (CHIME)*

T cells experience a variety of cell states throughout the course of disease[1]. Specifically, naïve, activated, effector and exhausted subsets exhibit unique T cell responses and functions, which by extension are likely governed by altered signaling events[1,48,147]. Moreover, different immune cell subsets adopt distinct functions during pathogenesis despite signaling through similar immunoreceptors. PD-1 KO on Treg cells, for example, has been shown promote Treg immunosuppressive function demonstrated by ameliorated EAE and diabetes, whereas our studies have shown that PD-1 KO on CD8$^+$ T cells enhances their effector functions in the tumor setting (Figure 3.1)[174]. For this reason, it would be useful to assess PD-1 signaling simultaneously in different immune cell subsets, specifically during disease pathogenesis.

While we have utilized various proteomic methods to understand PD-1 signaling mechanisms, we have mainly relied on *in vitro* methods that do not fully recapitulate the environment experienced by immune cells throughout the course of disease. We appreciate that cell-to-cell communication, for example, between antigen presenting cell (APCs) and T cells, as well as exposure to excreted factors, such as cytokines, chemokines and metabolites, influence signaling patterns *in vivo*[175]. For this reason, we asked whether we could perform proximity labeling experiments in mice expressing PD-1-APEX2 in order to capture PD-1 signaling events *in vivo*. A method designed in the Sharpe lab known as chimeric immune editing (CHIME) provides an *in vivo* murine system to perturb genes in naïve T cells, B cells as well as macrophages and DCs[176]. In this approach, an irradiated mouse is reconstituted with edited Lin- SCA1+ c-Kit+ (LSK) cells from a donor mouse[176]. This method bypasses the pre-activation step necessary for transducing T cells *in vitro* and generates mice expressing specific gene edits only within the immune compartment[176]. Recent work has shown that expressing APEX2 fused to Ca$_V$1.2 channels in mouse hearts allows for efficient biotin labelling in isolated cardiomyocytes, confirming that APEX2 functions *ex vivo* in live tissues[177]. Based on these findings, we hypothesized that utilizing CHIME for over-expression of PD-1-APEX2 in the immune compartment of mice would allow us to investigate PD-1 signaling dynamics during disease.

To test this hypothesis, we first transduced LSK cells from PD-1 KO donor mice with the murine PD-1-APEX2 vector driven by an human phosphoglycerate kinase (PGK) promoter (Figure 2.1S) and injected these PD-1-APEX2 transduced LSK cells into irradiated recipient mice (Figure 3.10a). After 8 weeks of immune compartment reconstitution, the spleens and inguinal lymph nodes (iLNs) of the mice expressing the PD-1-APEX2 vector were harvested and analyzed via flow cytometry (Figure 3.10a). We found that the iLN and the spleen of these mice showed robust expression of PD-1 on all immune compartments surveyed compared to PD-1 KO control mice (Figure 3.10b). After confirming expression of PD-1-APEX2 *in vivo*, we harvested whole spleens from PD-1-APEX2-CHIME mice and incubated them *ex vivo* with biotin phenol media, treated with or without $H_2O_2$ and quenched, as described in Chapter 2.4. We then processed the spleens into single cell suspensions and lysed the cells for Western blotting analysis to assess labelling efficiency. Remarkably, splenocytes treated with $H_2O_2$ displayed significantly more labelling than those without $H_2O_2$ (Figure 3.10c). While these splenocytes were not further processed for mass spectrometry analysis, we believe these methods would be useful in the future for studying immune cells during disease pathogenesis. Specifically, isolating and labelling whole tumors, splenocytes following LCMV infection or the CNS during EAE infection would be very insightful not only for understanding signaling variations in immune cell subsets at different time points, but also for assessing differences in various T cell states. More importantly, *in vivo* proximity labelling would allow for the comparison of particular PD-1 mutant constructs, including PD-1 ITIM and ITSM mutants as well as serine mutants, during disease pathogenesis.



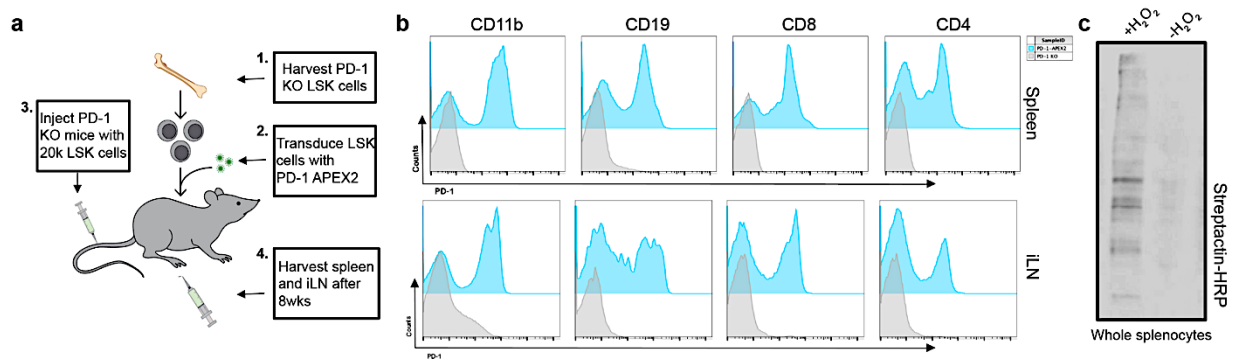**Figure 3.10: *In vivo* PD-1-APEX2 proximity labelling.** a) Schematic of CHIME with PD-1-APEX2 overexpression in PD-1 KO mice. b) Representative PD-1 expression (blue) in the immune compartment of PD-1-APEX2 chimeric spleen and iLN compared to PD-1 KO control mice (gray). c) Western blot analysis of whole splenocytes from PD-1-APEX2-CHIME mice probed with streptactin-HRP to assess labelling efficiency.

**3.3 Discussion**

Our comprehensive analysis of PD-1 mutant *in vivo* models, phosphorylation alterations in TCR-mediated signaling pathways, protein localization dynamics and binding interactions on the cytoplasmic tail of PD-1 have yielded novel insights regarding the specific functions of the ITIM and ITSM, as well as identified uncharacterized phosphorylation sites on PD-1 (Figure 3.11). We have confirmed that the ITSM recruits SHP2 and, to a lesser extent, SHP1 as mediators of PD-1 inhibition that dephosphorylate TCR-related signaling components to attenuate T cell function (Figure 3.3a-b and Figure 3.6a-b). Our data also provide evidence suggesting that the ITIM may be involved in activating T cell degradation machinery as well as receptor localization at the immune synapse, both of which are novel functions for this motif that have not been characterized (Figure 3.3c-g, j-l and Figure 3.7a-c). The distinct functions of the ITIM and ITSM likely explain the differences observed in tumor growth kinetics in ITIM and ITSM mutant mice (Figure 3.1a-b). Moreover, we have identified novel serine phosphorylation sites in the cytoplasmic tail of PD-1 that may retain residual signaling function (Figure 3.8 and Figure 3.9). These findings provide new information about PD-1 signaling mechanisms that could be exploited for therapeutic benefit and extended to ITIM- and ITSM-containing immunoreceptors for which signaling remains unclear.

Our analyses of TCR effector pathways impacted by mutation or loss of PD-1 suggest that each motif preferentially regulates specific signaling proteins (Figure 3.2). However, these phosphorylation events need to be more closely examined since proteins contain multiple activating and inactivating phosphorylation sites that may be preferentially targeted by PD-1-recruited phosphatases and kinases. Specifically, we aim to study AKT-pT308 using phospho-flow cytometry to further confirm our RPPA findings and determine if this phosphorylation site is targeted by the ITSM. Still, these findings highlight distinct signaling outcomes governed by either the ITIM or ITSM, which we have determined translates to differential disease response in PD-1 mutant mice. Decreased tumor burden and increased survival observed in PD-1 ITSM mutant mice comparable to PD-1 KO mice confirms that the ITSM is the predominant regulator of PD-1-mediated inhibition in this setting, which depends on enhanced function of effector T cells (Figure 3.1).
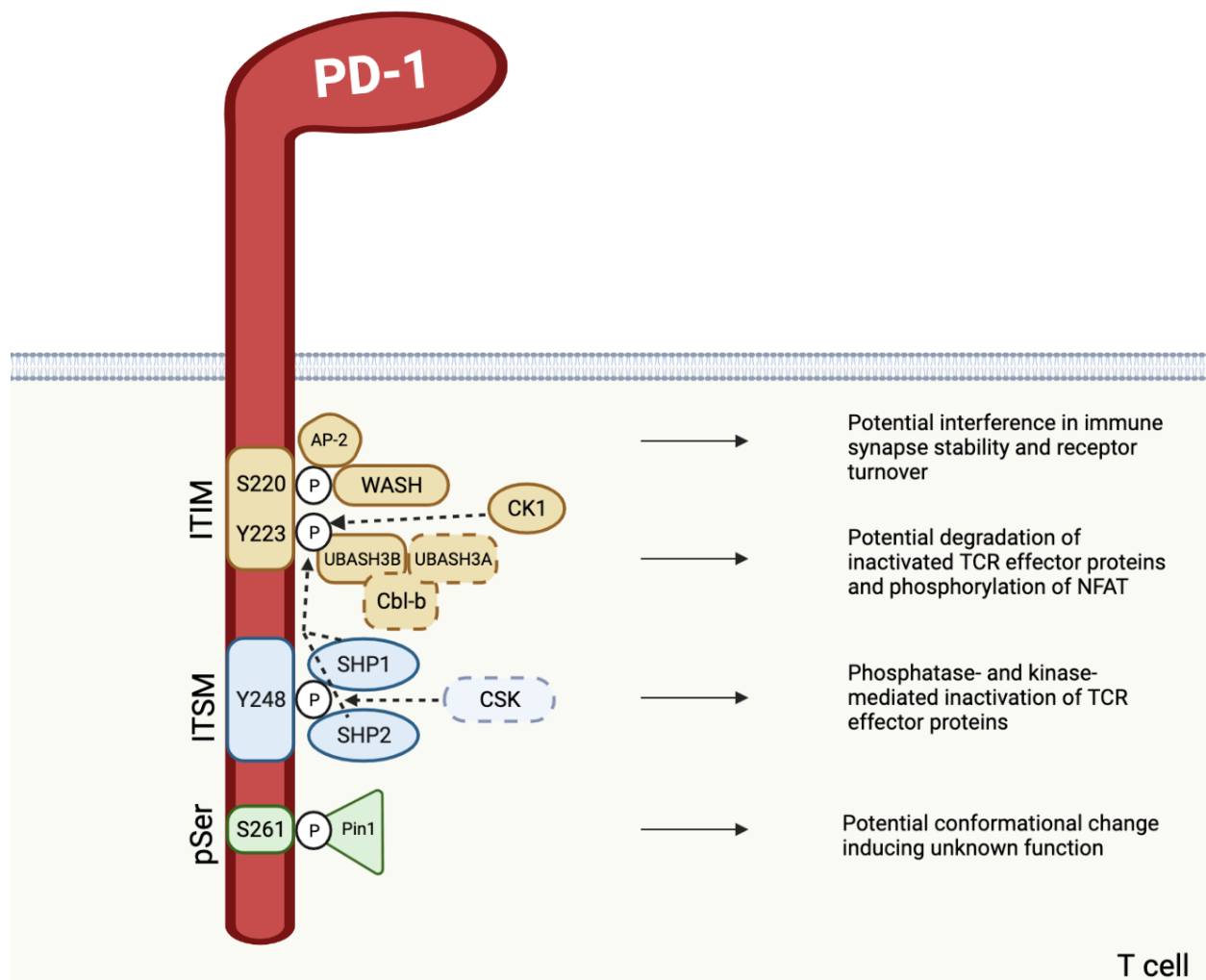
**Figure 3.11: Hypothetical PD-1 signaling model.** a) Schematic depicting the hypothetical functions of each PD-1 signaling motif summarized from data outlined in Chapter 3.2. ITIM and related protein mediators are depicted in yellow, ITSM and related protein mediators are depicted in blue and pSer261 and related protein mediators are depicted in green. Solid lines and arrows originating from proteins depict strong associations with PD-1 while dotted lines and arrows depict less robust associations with PD-1. Descriptions of the potential functions of each PD-1 phospho-site are listed adjacent to the phospho-site in reference. Schematic created using BioRender.

However, ITSM mutant mice do not fully recapitulate phenotypes observed in PD-1 KO mice, signifying a role for the ITIM or other potential signaling motifs. Using both proximity labelling and peptide-pulldown proteomics, we found that the ITIM exclusively associates with proteins involved in ubiquitination and proteasomal degradation. PD-1-mutant-APEX2 proximity labelling revealed diminished recruitment of Cbl-b, UBASH3A and UBASH3B to the ITIM-mutant, while these associations were increased in ITSM-mutant cells upon PD-1 ligation, suggesting that the ITIM governs recruitment of these proteins (Figure 3.3j-l). Additionally, phospho-peptide pulldown experiments identified UBASH3B and, to lesser extent, Cbl-b and UBASH3A binding to phosphorylated ITIM peptides (Figure 3.7a-c). Given these findings, we hypothesize that the ITSM is responsible for inactivating proteins through phosphatase recruitment, while the ITIM recruits proteins that ubiquitinate and degrade target proteins inactivated by the ITSM. Cbl-b is an E3-ligase that negatively regulates T cell activation signals by inducing the proteasomal degradation of Src family kinases, including ZAP70, following the TCR signaling cascade[155,157]. Moreover, mice deficient in Cbl-b have been shown to be resistant to PD-1-mediated suppression while PD-L1 silencing in DCs blocked upregulation of Cbl-b, insinuating that PD-1 may regulate Cbl-b function[178,179]. On the other hand, studies have shown that Cbl-b binds to and induces the proteasomal degradation of PD-1 and furthermore, Cbl-b deficient mice experience more rapid tumor growth[180]. For these reasons, PD-1 and Cbl-b function remains unclear.

In addition, UBASH3B and UBASH3A are both negative regulators of T cell activation and contain a ubiquitin-associated (UBA), c-terminal histidine phosphatase (PGM domain) and SH3 domain, which interacts with Cbl-b. The PGM domain of UBASH3B exhibits greater activity than the PGM domain of UBASH3A and has been linked to ZAP70 dephosphorylation, in line with Cbl-b function[154,155,158]. Interestingly, ZAP70 recruitment is also the most depleted in ITIM mutant cells compared to WT and ITSM mutants, while ZAP70 dephosphorylation is more impaired in ITSM mutant compared to ITIM mutant CD8^{+} T cells (Figure 3.2i and Figure 3.3h). PD-1 ligation induces ZAP70 dephosphorylation, presumably through SHP2 activation, but it is possible that UBASH3B regulates this dephosphorylation and degradation[15,30]. The true mechanism of ZAP70 dephosphorylation upon PD-1 ligation requires further experimentation for

clarification, as ZAP70 may also be indirectly inactivated through CSK inhibition of LCK. Alternatively, UBASH3A is associated with TCR and CD3 subunit turnover as well as endocytic recycling of membrane receptors[156,181]. Our PD-1-APEX2 time course experiments showed an enrichment of pathways involved in membrane trafficking and clathrin-mediated endocytosis in PD-L1-treated, suggesting a potential role for PD-1-mediated UBASH3A function in receptor turnover (Figure 2.1i-j). These mechanisms align with PD-1 pS-ITIM association with WASH and AP-2 complex proteins discussed below. While single deletion of either UBASH protein displays mild phenotypic alterations, deletion of both proteins results in hyperactive T cell responses linked to autoimmunity, suggesting a potential compensatory mechanism in singly deleted mice[158]. Still, the preferential functions of UBASH3B and UBASH3A may account for recruitment differences between the ITIM and ITSM observed in PD-1-mutant proximity labelling experiments (Figure 3.2j-k). Together, these data support a potential role for the ITIM in recruiting ubiquitin-mediated degradation machinery with ZAP70 phosphatase function to attenuate T cell activity (Figure 3.3j-l).

We also observed both ITIM and ITSM phospho-peptides associating with CK1, an inhibitory kinase that promotes NFAT localization in the cytoplasm through phosphorylation[165]. From our results, it is unclear which motif governs this association, further emphasizing the need to repeat these pulldown experiments with more replicates. Still, while the dephosphorylation of PLCγ likely prevents calcineurin-mediated dephosphorylation of NFAT and its subsequent translocation to the nucleus, recruitment of CK1 may simultaneously phosphorylate NFAT molecules that have already been targeted by calcineurin (Figure 3.4d and 3.5g)[17,114]. This proposed mechanism, as well as the multiple mechanisms postulated for ZAP70 dephosphorylation described above, introduce the notion that PD-1 not only prevents further TCR-mediated signaling from occurring but also reverses activation events that have already occurred following TCR-ligation.

This inactivation and degradation model aligns with phenotypic observations of tumor growth in the ITIM- and ITSM-mutant mice described above (Figure 3.1). Inactivation of TCR effector proteins by the ITSM is sufficient to attenuate T cell function[14,15,19,48]. Conversely, when the ITSM is mutated, TCR-effector proteins are not inactivated and therefore, TCR and costimulatory signaling remain intact, resulting in decreased

tumor burden (Figure 3.1a-b). For this reason, degradation machinery recruited by the ITIM is incapable of identifying and marking proteins for degradation if they are not previously inactivated by ITSM effector proteins. Furthermore, tumor-bearing ITIM-mutant mice resemble WT mice since the ITSM continues functioning to inactivate TCR signaling mediators. However, ITIM housekeeping proteins in ITIM-mutant mice may not be sequestered to promote degradation of the inactivated TCR effector proteins. Future studies are necessary to evaluate this hypothetical model. Specifically, proteomic analysis of the ubiquitinome in the presence or absence of PD-1 ligation in ITIM and ITSM mutant mice would unveil changes in protein ubiquitination status potentially governed by the ITIM[182,183]. Additionally, genetic KO studies of Cbl-b and UBASH proteins compared to ITIM mutants would verify the specific regulators of ITIM-mediated signaling.

We also identified a novel phospho-serine upstream of the pY-ITIM (Figure 3.5b). Both the pS-ITIM and pY-ITIM display redundancy in protein binding to Cbl-b and UBASH3A observed in phospho-peptide pulldowns (Figure 3.7b-c), suggesting that these two phosphorylation sites depend on one another for protein binding. Still, the pS-ITIM exclusively bound unique proteins to a greater extent than the pY-ITIM (Figure 3.8). WASH complex and AP-2 adaptor proteins mediate actin cytoskeletal dynamics and receptor turnover at the immune synapse, respectively[121,166–168]. WASHC2A and WASHC3, among additional WASH complex proteins we identified (data not shown), act as components of the WASH complex, which functions to activate the Arp2/3 complex that regulates branched F-actin nucleation to drives receptor internalization, T cell receptor signaling and T cell activation (Figure 3.8a-b)[121,166]. WASH KO in T cells reduces receptor trafficking, proliferation and effector function, similar to PD-1-mediated inhibition[166]. These findings correlate with the dephosphorylation of CARMIL2, which associates with the Arp2/3 complex, upon PD-1 ligation, implying that PD-1 is disrupting actin cytoskeletal rearrangements that drive optimal T cell signaling (Figure 3.4e and Figure 3.5h)[18,95].

Moreover, pS-ITIM strongly associated with AP-2 complex proteins AP2A1 and AP2B1, among additional AP-2 complex proteins we identified (Figure 3.8c-d and data not shown). AP2 adaptor proteins link cargo to the clathrin-coated pit to mediate clathrin-dependent endocytosis in T cells, similar to receptor

internalization driven by the WASH complex[166,168]. In B cells, AP2 adaptor proteins bind to the YxxΘ motif, where x is any amino acid and Θ is a bulky hydrophobic amino acid such as leucine or isoleucine[167]. The ITIM sequence VD**Y**GE**L** also resembles this motif where leucine is the bulky hydrophobic residue adjacent to glycine and glutamic acid. It is possible that phosphorylation of pS-ITIM facilitates binding of pY-ITIM to AP2 complex proteins to induce PD-1 receptor internalization or to interfere with ongoing clathrin-mediated endocytosis at the immune synapse. These findings align with our data identifying membrane trafficking and clathrin-mediated endocytosis pathways enriched in PD-L1-treated APEX2 time course experiments and also in PD-1 mutant APEX2 experiments, where protein recruitment to the ITIM mutant was diminished (Figure 2.1i and Figure 3.2). It is also worth noting that WASH and AP-2 mechanisms resemble TCR inactivation processes mediated by Cbl-b and UBASH3A/B proteins recruited by the pY-ITIM[155,156,178,181].

These pS-ITIM data introduce a second hypothesis for lack of tumor control in ITIM mutant mice. Given the redundancy in protein binding to the pS-ITIM and pY-ITIM, it is possible that double mutation of these residues is required to fully abolish ITIM function, resulting in a stronger T cell activation phenotype compared to that observed in single PD-1 pY-ITIM mutant mice (Figure 3.1a-b). Single mutation in the pY-ITIM in proximity proteomic studies showed diminished recruitment of immune synapse proteins, including TCR components and effectors, to the ITIM, supporting that membrane trafficking machinery may be impaired (Figure 3.3c-h). Simultaneous mutation of the pS-ITIM to a neutral glycine or alanine reside could further abrogate this function, leading to severe disruption of immune synapse formation and inhibition of T cell activation. It would be interesting to assess whether doubly mutated pY-ITIM and pS-ITIM mice are able to control tumor growth better than singly mutated pY-ITIM mice. In addition, proximity-phospho proteomic analysis of pY-ITIM, pS-ITIM and pY-ITSM will be crucial for determining which motif regulates dephosphorylation of actin cytoskeletal proteins, specifically F-actin regulators such as CARMIL2, observed in both of our proximity phospho-proteomic experiments (Figure 3.4f and Figure 3.5h). Together, these data suggest that serine phosphorylation adjacent to the ITIM interferes with actin polymerization and endocytic processes at the immune synapse and this membrane remodeling likely contributes to PIEZO1 activation outlined in Chapter 2.

A second novel serine phosphorylation site discovered using proximity phospho-proteomics also displayed unique binding capabilities in our phospho-peptide pulldown analysis. PD-1 pSer261 had limited binding to the majority of pulled-down proteins, but exclusively bound TNKS-1 and PIN1 compared to other PD-1 phospho-motifs (Figure 3.9). PD-1 pSer261 is adjacent to proline residues, which facilitate the binding of PIN1 to phospho-serine and -threonine residues. Exploring this interaction further may unveil novel PD-1 function as PIN1 is known to facilitate confirmational changes that lead to regulation of protein interaction, catalytic activity, phosphorylation status, subcellular location and protein stability, all of which are affected by PD-1-mediated inhibiton[17,48,171,172]. Further experimentation is also necessary for analyzing the association between TNKS-1 and PD-1, as TNKS-1 is a DNA binding protein that may only associate with the pSer261 peptide by virtue of its similarity to tankyrase binding sites[169,170].

Overall, our findings continue to support the hypothesis that the ITSM recruits effector proteins that dampen TCR- and CD28-mediated signal transduction while the ITIM regulates actin cytoskeletal dynamics, receptor turnover and protein degradation. Moreover, the potential function of the ITIM in controlling clustering at the immune synapse observed in previous studies and our proximity labeling experiments may in fact be governed by the phospho-serine site adjacent to ITIM, which exhibits robust association with membrane trafficking proteins[19]. pSer261 may be also involved in protein recruitment that sterically alters the cytoplasmic tail of PD-1. Whether PIN1 association with PD-1 results in a novel PD-1 function is yet to be determined. To validate the significance of observed trends with large spread between replicates or with single replicates, we aim to repeat these experiments with a larger number of replicates to establish more concrete conclusions.

Technically, we found that our proximity phospho-proteomic results were reproducible across species and confirmed the legitimacy of our bead-based system to drive strong activating and inhibitory signals through TCR/CD28 and PD-1, respectively. Given the accuracy with which proximity phospho-proteomics recapitulated characterized TCR and PD-1 signaling mechanisms, we aim to perform these studies in ITIM and ITSM mutant cell lines, as there would be much utility in determining how the two tyrosine phosphorylation motifs affect signaling in addition to recruitment kinetics. We recognize that key

phosphorylation events were not detected in our preliminary analyses using this novel proteomic method. Global phospho-proteomics requires a significant amount of protein to capture the limited amount of phosphorylation occurring within a cell. As a result, identifying phosphorylation events within a smaller, enriched population of proteins is more difficult. We believe phosphorylation of the PD-1 ITSM, for example, was not captured due to limiting amount of protein input. This is supported by comparing our murine and human proximity phospho-proteomic trials where greater initial input of enriched proteins in the murine trial yielded significantly more phosphorylation events compared to the human trial (487 murine versus 128 human). Still, we believe this technique will be extremely useful for analyzing phosphorylation events over time using various PD-1 mutant constructs.

Finally, we appreciate that our studies have not explained how PD-1 signaling may differ among various immune cell subsets, namely Treg cells. Interestingly, ongoing work in the Sharpe lab has discovered that ITSM mutant mice experience alleviated EAE symptoms compared to PD-1 KO mice, which is unexpected given phenotypic similarities observed in PD-1 KO and ITSM mutant models[184] (manuscript under revision). It is possible that ITSM mutant Tregs are more suppressive than PD-1 KO Treg cells, uncoupling ITSM function from global PD-1 KO[184,185] (manuscript under revision). This notion is supported by work from the Sharpe lab demonstrating that PD-1 deficiency in Treg cells leads to activated Treg cells with potent immunosuppressive function in the context of EAE and diabetes[174].  Since differential signaling outcomes arise on distinct immune cell subsets *in vivo*, PD-1-APEX2 proximity labeling *in vivo* and *ex vivo* may aid in identifying key PD-1 regulatory mechanisms during disease pathogenesis. We have shown that PD-1-APEX2-CHIME mice express PD-1-APEX2 on various immune cell subsets and the APEX2 labelling probe is capable of biotinylating whole splenocytes (Figure 3.10b-c), setting the stage for such experiments. These studies can be performed in numerous disease models to investigate specific signaling events that elucidate PD-1 function in pathogenic organs and tumors containing various immune cell subsets.

In summary, we find that the ITIM and ITSM motifs indeed govern distinct functions in T cells due to their differential control of tumor growth and recruitment of specific signaling mediators (Figure 3.11a). Our *in vivo* studies confirm that the differential functions of the ITIM and ITSM play a significant role in regulating

disease pathogenesis in the context of cancer and ongoing studies are focused on determining the function of the ITSM in Treg cells (manuscript under revision). We believe the ITSM recruits effector phosphatases and kinases that dampen TCR-mediated signaling, while the ITIM governs protein degradation in response to ITSM inactivation of TCR effector proteins. Finally, we have discovered novel serine phosphorylation sites on the cytoplasmic tail of PD-1 that may regulate unique PD-1 functions. In conjunction with pY-ITIM, the pS-ITIM may regulate membrane trafficking and receptor turnover through actin cytoskeletal rearrangements that alter immune synapse formation. PD-1 pSer261 may promote conformational changes driven by PIN1 that regulate uncharacterized PD-1 function, such as protein interaction, subcellular location or protein stability. Together, we believe these findings will continue to inform our understanding of PD-1 function on various immune cell subsets and may translate to targeted immunotherapies in cancer and autoimmunity.

**3.4 Materials and methods**

*Mice*

WT C57BL/6 mice were obtained from The Jackson Laboratory. *WT FoxP3$^{GFP}$* reporter and *Pdcd1$^{-/-}$ FoxP$^{GFP}$* mice have been previously reported. ITSM and ITIM mutant mice were generated by gene targeting in Bruce 4 C57BL/6 ES cells. Constructs were generated such that the tyrosine residue was replaced with a phenylalanine in the ITSM (Y248F) and ITIM (Y223F). The targeting vector contained frt sites on either side of a selection cassette containing neomycin (neo) under control of the PGK. Linearized vector DNA was electroporated into Bruce 4 C57BL/6 ES cells and the resulting neomycin-resistant ES cells screened for the ITSM or ITIM mutation by PCR, Southern blotting and Sanger sequencing. ES cells carrying the ITSM or ITIM mutation were injected into albino B6 blastocysts. Chimeric mice were bred with WT C57BL/6 mice that gave rise to progeny carrying the PD-1 ITSM or ITIM mutation. Progeny were bred with C57BL/6 Flpe mice to remove the neomycin gene, which was flanked by frt sites.

Sanger Sequencing was used to validate the ITSM and ITIM mutant mice. Spleens from PD-1 WT, ITSM and ITIM mutant mice were harvested and DNA extracted using the Qiagen DNeasy kit. A primer pair was

generated (F- GTTCTGTGCCTGGGCAGCT, R- GGTGCTCTCTGTGGAGGGTC) and ordered from Integrated DNA Technologies (IDT) that amplified a 500 bp product including the sites of predicted mutation. The product was amplified using these primers from IDT technology and gel purification was conducted using the QIAquick Gel Extraction kit (Qiagen). Amplified, purified product was sequenced by Sanger Sequencing at the HMS Biopolymer facility.

Mice used in these studies were between 8-12 weeks of age. Age- and sex-matched animals were used for all experiments. All mice were maintained in a pathogen-free facility and used according to Harvard Medical School and NIH guidelines. Harvard Medical School is accredited by the American Association of Laboratory Animal Science.

*Tumor Experiments*

MC38 colorectal carcinoma or B16-OVA melanoma cell lines were used for *in vivo* tumor studies. MC38 cells were cultured in DMEM media with 10% FBS, 1% penicillin/streptomycin and 20 µg/ml gentamicin. B16-OVA cells were cultured in DMEM media with 10% FBS and 1% penicillin/streptomycin. OVA-expressing cells were selected by addition of Puromycin to the media. $1x10^6$ MC38 cells or $3x10^5$ B16-OVA cells, as indicated in text, were injected into mice subcutaneously, and mice were monitored for tumor growth every 2 days starting day 3-5 post tumor injection. Animals were sacrificed if tumor size was >2000mm$^3$, tumors became ulcerated or weight loss was > 20%.

For cellular analysis of TILs, tumors were harvested on day 10 post tumor cell injection. Tissue was digested with collagenase A (Sigma-Aldrich #10103586001) and DNase 1, resuspended in 30% Percoll (diluted in PBS) and underlaid with 70% Percoll to generate a gradient that was centrifuged at 805 RCF for 20 min (no brake). Immune cells were harvested from the interface between 30% and 70% Percoll and resuspended in buffer (PBS with 1 % FBS and 2 mM EDTA) for staining for flow cytometry analyses. Cells were surface stained with CD45.2 (BioLegend clone 104), CD3ε (BD Biosciences clone 145-2C11), CD4 (BioLegend clone RM4-5), and CD8β (BioLegend clone Ly-3) antibodies at a 1:100 dilution and with LIVE/DEAD Fixable Near-IR Dead Cell Stain kit (Thermo Fisher Scientific, 1:600) for 45 min in the dark on

ice. Samples were washed twice with MACS buffer (PBS-/-, 1% FBS, 2mM EDTA) and fixed and permeabilized with FoxP3/Transcription Factor Staining Buffer Set Kit (eBioscience). Cells were stained with FoxP3, granzyme B, perforin, TNF$\alpha$ and IFN$\gamma$ (BioLegend, 1:100) for 1 h in the dark on ice and washed twice with MACS buffer. Fixed and stained samples were run on the BD FACSymphony and analyzed using FlowJo software.

*RPPA Analysis*

Spleens and cervical lymph nodes were harvested from PD-1 WT, KO, ITIM and ITSM mutant mice and naïve CD8$^+$ T cells were isolated using MACS isolation (Miltenyi). Naïve CD8$^+$ T cells were stimulated overnight in RPMI media supplemented with 10% FBS, 1% penicillin/streptomycin, 1% HEPES and 0.1% BME in 6-well plates coated with 4$\mu$g/mL of CD3/CD28 crosslinking antibodies (BioXCell). Stimulated CD8$^+$ T cells isolated from three mice per genotype were pooled, centrifuged at 453 RCF and counted to determine total number of CD8$^+$ T cells per genotype. Cells were then plated at a concentration of 100k cells per well in round bottom 96-well plates. TCR-PD-L1 beads were co-cultured with CD8$^+$ T cells for 24 h at a cell to bead ratio of 1:4 (Chapter 2.4). Following bead treatment, cells were collected and pooled by genotype and bead treatment. Cells were centrifuged at 453 RCF, washed 2X with PBS and lysed in RIPA buffer. Lysates were treated with 4X Laemmli Sample Buffer (Bio-Rad), as suggested by MD Anderson RPPA Core. Protein quantification was performed using BCA assays and this information was provided with the samples when shipped on dry ice to MD Anderson for RPPA analysis, where cell lysates were serially diluted two-fold for 5 dilutions (undiluted, 1:2, 1:4, 1:8; 1:16) and arrayed on nitrocellulose-coated slides in an 11x11 format to produce sample spots. Sample spots were then probed with 422 unique antibodies by a tyramide-based signal amplification approach and visualized by DAB colorimetric reaction to produce stained slides. Stained slides were scanned on a Huron TissueScope scanner to produce 16-bit tiff images and QC tests were performed for each antibody staining. Sample spots in tiff images were identified and their densities quantified by Array-Pro Analyzer. Relative protein levels for each sample were determined by interpolating each dilution curve produced from the densities of the 5-dilution sample spots using a "standard curve" (SuperCurve) for each slide (antibody). SuperCurve is constructed by a script in R, written by Bioinformatics. Relative protein levels are designated as log2 values. All relative protein level

data points were normalized for protein loading and transformed to linear values, which are designated "Normalized Linear." Normalized linear values were used for generating bar graphs.

*Phospho-flow cytometry*

Naïve CD8+ T cells were isolated from spleens of PD-1 WT, KO, ITIM and ITSM mutant mice using negative selection MACS isolation (Miltenyi). Naïve CD8+ T cells were stimulated for 48 h on 96-well U-bottom plates coated with 4$\mu$g/mL anti-CD3 and anti-CD28 crosslinking antibodies. Cells were then rested in RPMI media supplemented with 10% FBS, 1% penicillin/streptomycin, 1% HEPES and 0.1% BME in 96-well V-bottom plates for 4 h prior to restimulation. CD3/CD28 IgG control beads or PD-L1 beads were added at a cell:bead ratio of 1:4 for the specific timepoints: 10, 30 and 60 min. Cells were spun for 20 s at 726 RCF to remove media and cell/bead mixtures were immediately fixed in 2% PFA at room temperature for 10 min. One volume of PBS was added to each well and cells were again centrifuged at 800 RCF for 2 min. Cells were then washed twice with MACS buffer (PBS-/-, 1% FBS, 2mM EDTA) and centrifuged at 800 RCF for 2min. 90% ice-cold methanol was slowly dropped onto the cells and mixed for permeabilization. MeOH-permed cells were stored in the -80 freezer prior to use or left on ice for 20 m to complete permeabilization. One volume of MACS buffer was added on top of the MeOH and centrifuged at 800 RCF for 2min. Wells were washed once more with MACS buffer and stained with pERK (CST, clone 197G2), pS6 (CST, clone D57.2.2E), pAKT (CST, clone D9E) and pZap70 (BD Biosciences clone 69E4) antibodies diluted 1:50 for 1 h at room temperature in the dark. Stain was washed off with MACS buffer and samples were resuspended and run on the BD LSRII or BD FACSymphony.

*PD-1 mutant APEX2 proximity labelling*

ITIM and ITSM PD-1-APEX2 constructs were designed such that tyrosine phosphorylation residues were mutated to phenylalanine to maintain structural integrity of the PD-1 cytoplasmic tails using the same vector as WT PD-1-APEX2 described in Chapter 2.4 (Figure 2.S1a). Cloning was performed by GenScript. Jurkat cells were lentivirally transduced with PD-1 mutant APEX2 constructs as described in Chapter 2.4. PD-1 mutant APEX2-expressing cells were incubated with biotin phenol, treated with mIgG$_1\kappa$ control or PD-L1 beads for 5 and 20 min, labelled with $H_2O_2$ and processed as described in Chapter 2.4.

*Phospho-peptide pulldowns*

Phospho-peptide pulldowns were adapted from previously described methods[186]. Desthiobiotin-tagged peptides containing free N-terminal amine and C-terminal acid were synthesized by New England Peptide with greater than 90% purity. Peptide sequences are as follows:

ITIM (Desthiobiotin-SGSGVPVFSVDYGELDFQW)

pY-ITIM (Desthiobiotin-SGSGVPVFSVD(pY)GELDFQW)

pS-ITIM (Desthiobiotin-SGSGVPVF(pS)VDYGELDFQW)

ITSM (Desthiobiotin-SGSGCVPEQTEYATIVFPS)

pY-ITSM (Desthiobiotin-SGSGCVPEQTE(pY)ATIVFPS)

S-261 (Desthiobiotin-SGSGTIVFPSGMGTS(pS)PARRGSADGPR)

pS-261 (Desthiobiotin-SGSGTIVFPSGMGTSSPARRGSADGPR)


Streptavidin magnetic beads (Pierce, #88817) were rinsed twice with lysis buffer (50mM EPPS pH 7.5 buffer with 150mM NaCl, 1% NP-40, and 1mM DTT). Desthiobiotin-tagged peptides were dissolved in DMSO to obtain 10mg/mL stocks.   Four molar equivalents of peptides or naked desthiobiotin (16mmol) were added to the washed streptavidin beads.  The beads were rotated overnight at 4°C for maximum binding.  The next morning beads were washed 3X with lysis buffer described above followed by three additional washes with lysis buffer containing 1mM sodium orthovanadate and Complete EDTA-free Protease Inhibitor (Millipore Sigma, #11873580001).  The beads were further split for a total of 16 samples with 2 biological replicates for each pull-down condition with 2mmol loading capacity.


While on ice, two Jurkat cell pellets were lysed with 800μL ice cold lysis buffer containing 1mM sodium orthovandate and protease inhibitors for duplicate conditions.  The lysates were shredded by centrifuging through Qiashredder (Qiagen, #79656) at 20,817 RCF for 5 min in a 4°C. A BCA assay was performed to measure protein concentration.  The more concentrated lysate was diluted to protein concentration that was equivalent for both lysates.  Subsequently, 1mg of protein was added to each sample of peptide-loaded streptavidin beads.  The beads were rotated with the lysate overnight at 4°C.  While in the cold room, the

beads were washed twice with 300μL of ice-cold lysis buffer and transferred to new tubes then washed two additional times with lysis buffer. Desthiobiotin-tagged peptides and bound proteins were eluted with 50μL of 4mM biotin in 200mM EPPS pH 8.5 for 10 min at 37°C. This elution step was repeated 2 additional times for a total of 3 washes with a total volume of 150μL. The eluted proteins were reduced with 1.5μL of 0.5M DTT for 30min at 60°C with gentle shaking (1000 RPM) using the Eppendorf ThermoMixer C (Orbital Shakers). The tubes were cooled to room temperature and cysteine residues were alkylated with 15μL 0.2M iodoacetamide for 30min at room temperature in the dark. The alkylation reactions were quenched with 1.5μL of 0.5M DTT.

An SP3 clean-up was performed to remove detergent and remaining alkylation reagents[187]. Briefly, fresh SP3 beads were prepared by combining 400μL of two types of Sera-Mag beads (GE Healthcare, #45152105050250 and #65152105050250) and the storage buffer was removed by magnetic separation. The SP3 beads were rinsed once with 400μL HPLC-grade water and resuspended in 400μL HPLC-grade water. To each sample, 10μL of SP3 beads were added and gently mixed by pipetting. An equal volume of ethanol (150μL) was added to each sample, gently mixed by pipetting, and incubated for 5min at 25 °C with shaking at 1000 RPM. The supernatant was removed and the SP3 beads were washed three times with 540μL of 80% ethanol. While still adhered to the SP3 beads, proteins were digested and further processed as described in the APEX protocol.

*Proximity phospho-proteomics*

Human and murine PD-1-APEX2 proximity labelling time course experiments were performed as described in Chapter 2.4 up to the TMT labelling step. After TMT labeling and quenching, peptides were acidified with formic acid and dried down to near completion in a speed vac. Peptides were then re-suspended in 200 μl 1% formic acid and 0.1% tri-fluoro acetic acid (TFA) and purified via C18 reversed phase chromatography over Sep-Pak cartridges (Waters, #WAT054960). Gravity flow was used to bind peptides C18 matrix, which were washed 3X with a full column volume with 1% formic acid only. Peptides were then eluted in 95% acetonitrile 1% formic acid and dried down to near completion in a speed vac and re-suspended in 50 μl

Fe-NTA binding buffer (0.1% trifluoroacetic acid, 80% acetonitrile; included in High-Select[TM] Fe-NTA Phosphopeptide Enrichment Kit, Thermo Scientific #A32992).

To create a micro Fe-NTA enrichment column, a small C18 matrix plug was inserted into a pipette tip after punching out a small amount of C18 matrix from a C18 Empore[TM] solid phase extraction disk (Sigma-Aldrich, #66883-U), creating a one disk STAGE-tip as widely used in mass spectrometry[188]. The tip was washed and conditioned with 100 µl of neat acetonitrile, followed by addition of Fe-NTA matrix. For this, 10 µl of re-suspended Fe-NTA bead slurry from a High-Select[TM] column (see above) was added into the STAGE-tip. To prevent the beads from drying, bead storage buffer was passed carefully through the micro-enrichment tip by air pressure with a cut-off pipettor tip. Beads were washed by passing 70 µl of Fe-NTA binding buffer through the micro phospho-enrichment tip twice, and re-suspended peptides in Fe-NTA binding buffer were added to Fe-NTA beads with a fine pipette tip. Re-suspension of Fe-NTA beads in the micro enrichment column was repeated every ten minutes for a total binding time of 30 minutes, minimizing contact of peptide solution with the walls of the enrichment tip to improves phospho-peptide enrichment. After 30 min of binding, the peptide solution was passed through the micro enrichment tip into a clean collection tube and collected together with 3 washes with 70 µl Fe-NTA binding buffer, a single wash with 70 µl ultrapure water and 50 µl of neat acetonitrile. The combined flowthrough and washes were dried down in a speed vac to completion for subsequent bench-top fractionation of non-phospho peptides and MS analysis by alkaline reversed phase chromatography (Pierce[TM] High pH Reversed Phase Peptide Fractionation Kit, Thermo Scientific #84868) with a modified elution scheme as described preiously[103].

After binding to Fe-NTA beads, peptides were eluted with 25 µl of Fe-NTA elution buffer (ammonia solution in ultrapure water, pH 11.3; elution buffer provided with High-Select[TM] kit) two times followed by elution with 50 µl neat acetonitrile. Beads turned dark brown after elution. Ammonia and acetonitrile eluates were collected directly in a single glass insert for MS autosampler vials, dried down to completion in a speed vac and dried phospho-peptides were re-suspended in 6µl 1% formic acid for subsequent µHPLC injection and MS analysis.

*Mass spectrometry methods*

Data were collected on an Orbitrap Fusion Lumos instrument (ThermoFisher Scientific) with a Multi Notch MS[3] method using a scan sequence of MS1 orbitrap scans (resolution 120,000; mass range 400-2000 Th), MS[2] scans after collision-induced dissociation (CID, CE=35) in the ion trap with varying injection times[144]. For phospho-peptide analysis, a multi-stage activation method was used with a neutral loss of 97.9763/z. Quantitative information was derived from subsequent MS[3] scans (orbitrap, resolution 50,000 at 200 Th) after high-energy collision induced dissociation (HCD). Peptides were ionized by electrospray after HPLC separation with a MS-coupled Proxeon EASY-nLC 1200 liquid chromatography system (Thermo Fisher Scientific) using 75 $\mu$m inner diameter nanocapillaries with PicoTip emitters (NewObjective # PF360-75-10-CE-5) packed with C18 resin (2.6 $\mu$m, 150Å, Thermo Fisher Scientific). Fractionated peptides were separated over 3 and 4 h gradients with increasing concentrations of acetonitrile from 0% to 95% in 0.125% formic acid. For phospho-peptide analysis, peptides were resuspended in 1% formic acid without acetonitrile prior to nano LC injection and separated over 120 and 60 min gradients with 50% injected each as low amounts of material did not permit efficient fractionation. Injection times for phospho-peptides varied with up to 600ms for MS2 and 1000ms for MS3. A modified ANOVA score ("ModScore") as described previously was used to calculate localization confidence in phosphorylated residue position in the quantified phospho-peptides. MaxModscores of >13 correspond to confident localization of the phosphorylated residue position[189].

*Chimeric immune editing (CHIME) and in vivo proximity labelling*

Femurs, tibias, hips, and spines were isolated from WT C57BL/6 mice donor mice, crushed, and red blood cells were lysed using Ammonium-Chloride-Potassium (ACK) Lysing Buffer (Gibco)-lysed. LSK were enriched with a CD117 MACS isolation kit and then sorted to purity. The LSK cells were spin transduced with murine WT PD-1-APEX2 lentiviral constructs on a Retronectin-coated plate. LSK cells were then transferred intravenously into irradiated WT C57BL/6 mice recipients. Mice were monitored over 8 weeks during the reconstitution of the immune compartment. After 8 weeks, immune cells were isolated from iLNs and spleens of chimeric mice and stained for lineage markers as well as PD-1 to assess PD-1-APEX2 expression. Following confirmation of PD-1-APEX2 expression, whole spleens were harvested from

93

chimeric mice and incubated in biotin phenol media for 2 h. $H_2O_2$ was added to whole spleens for 1 min and quenched with buffers as described in Chapter 2.4. Chimeric spleens not exposed to $H_2O_2$ were used as negative controls. Quenched spleens were processed into single cell suspensions, lysed with RIPA buffer and prepared for Western blotting analysis. Western blots were probed with Streptactin-HRP to assess labelling efficiency.

**Chapter 4:**

**Conclusions and future directions**

**4.1 Summary**

While PD-1 blockade therapy has revolutionized cancer treatment for a myriad of patients, a significant subset of patients does not respond or show long lasting remission[4,23–27]. To date, our understanding of PD-1 signaling remains unclear despite the importance of PD-1 as a therapeutic target[1,17,23,48]. Developing a better understanding of the mechanisms driving PD-1-mediated inhibition may pave the way for the discovery of new therapeutic targets for cancer treatment.

In this thesis, we relied on proteomic methodology to study intracellular signaling mechanisms driving PD-1-mediated inhibition following PD-L1 ligation. We developed an unbiased proximity labelling platform that allowed us to study membrane dynamics and protein localization changes proximal to PD-1 in real time (Figure 2.1a-b)[102,143]. Remarkably, we discovered that PD-1 associates with the mechanosensitive ion channel PIEZO1 over time following PD-1 ligation (Figure 2.1d). We validated the functional relevance of this association using a variety of powerful *in vitro* and *in vivo* tools. Using TIRF live cell imaging and flow cytometry to monitor the activity of a fluorescent PIEZO1 reporter, we determined that PD-1 and PIEZO1 indeed colocalize at the immune synapse and this colocalization results in PIEZO1 inhibition (Figure 2.2e-f). PIEZO1 co-IP experiments showed an increased association between PD-1 and PIEZO1 following PD-L1 ligation using trigger peptide analysis (Figure 2.S5b). We also observed an increase in ubiquitin ligase proteins WWP1 and WWP2 associating with PIEZO1 upon PD-1 ligation, suggesting that PD-1 induces the degradation of PIEZO1 (Figure 2.S5c-e). We then developed a tamoxifen-inducible, CD8^{+} T cell-specific PIEZO1 KO mouse to determine the role of PIEZO1 in controlling tumor growth (Figure 2.3a and Figure 2.S8a-b). We found that PIEZO deficiency in CD8^{+} T cells was sufficient to impair antitumor immunity, resulting in increased tumor growth kinetics and fewer activated and cytotoxic CD8^{+} TILs in the TME (Figure 2.3b-i and Figure 2.S10). This impaired tumor growth could not be reversed by PD-1 blockade (Figure 2.3j-n). Interestingly, mice with PIEZO1 deficient CD8^{+} T cells exhibited high Slamf6 and low TIM-3 expression, while WT mice treated with PIEZO1 agonist displayed higher TIM-3 expression compared to Slamf6, implying that PIEZO1 activity regulates exhausted CD8^{+} T cell subpopulations (Figure 2.3f,i and Figure 2.4g). Conversely, we found that treating WT mice with PIEZO1 agonist *in vivo* improved CD8^{+} T cell effector functionality (Figure 2.4). Remarkably, when mice harboring PD-1 blockade-unresponsive B16.F10

tumors were treated with the PIEZO1 agonist Yoda1 in combination with PD-1 blockade, we observed

improved tumor control and overall survival compared to single therapy or vehicle and isotype controls

(Figure 2.4h-k)[126]. Overall, these findings confirm the legitimacy of proximity labelling in identifying novel

mechanisms for immune cell receptor signaling and new potential therapeutic targets for cancer patients.


While PD-1-APEX2 proximity labelling discovered PIEZO1 as a major target of PD-1-mediated inhibition,

we also sought to identify novel mediators of PD-1 function by determining the distinct functions of tyrosine

phosphorylation motifs on the cytoplasmic tail of PD-1[48]. We generated mice singly mutated in PD-1 ITIM

and ITSM sequences to assess the role of each motif in responding to tumors *in vivo* (Chapter 3.4 *Mice*).

In alignment with previous *in vitro* findings using ITIM and ITSM mutant CD4$^+$ T cells, we found that mice

harboring a mutation in the ITSM governed the majority of PD-1-mediated function, which was marked by

improved tumor clearance, survival and CD8$^+$ T cell function, comparable to PD-1 KO mice (Figure 3.1a-e,

h-l)[14,48,148]. However, mutation in the ITIM motif did not control tumor growth or significantly improve CD8$^+$

T cell function or infiltration in the TME, similar to WT mice (Figure 3.1a-e, h-l). Still, ITSM mutant mice did

not fully recapitulate phenotypes exhibited by PD-1 KO mice (Figure 3.1a,c,e,h-i). For this reason, we

employed various proteomic techniques to define the role of each motif in mediating PD-1 function[102,103,186].

Furthermore, our optimization of *in vivo* and *ex vivo* PD-1-APEX2 proximity labelling may aid in identifying

the source of observed phenotypic differences in various disease contexts (Figure 3.10)[176].


Our assessment of downstream signaling pathways revealed varying phosphorylation outputs in pS6,

pERK, pAKT, mTOR and ZAP70 pathways among PD-1 WT, KO, ITSM and ITIM mutant CD8$^+$ T cells,

suggesting that each motif uniquely regulates specific signaling arms of the TCR cascade (Figure

3.2)[9,14,15,17,30,48,49,148,152]. To determine how these pathways are preferentially regulated by specific

mediators, we performed PD-1-mutant-APEX2 proximity labelling and PD-1 phospho-peptide pulldowns.

We determined that the ITSM strongly recruits SHP2 and to a lesser extent SHP1 and CSK, suggesting

that the ITSM mediates PD-1 function through activation of inhibitory phosphatases and kinases, in line

with previous reports (Figure 3.5a-b and Figure 3.6a-b,e)[14,19,30]. Interestingly, we observed less PD-1

colocalization with TCR components overall in ITIM mutant cells, as well as recruitment of ubiquitin ligase

proteins Cbl-b, UBASH3B and UBASH3A, suggesting that the ITIM may play a role in receptor clustering and protein degradation (Figure 3.3c-h, j-l and Figure 3.7a-c) [19,154,192,155–158,178,181,190,191]. Moreover, using proximity phospho-proteomics, we identified novel phospho-serine sites on the cytoplasmic tail of PD-1 (Figure 3.4f and Figure 3.5a,c). Using phospho-peptide pulldowns to assess the binding behavior of each phospho-serine site, we found that pS-ITIM strongly associated with actin cytoskeletal nucleating WASH proteins and AP-2 adaptor proteins involved in clathrin-mediated endocytosis, suggesting that this phospho-serine adjacent to pY-ITIM may be involved in destabilizing the immune synapse (Figure 3.8a-d)[121,166–168]. In addition, pSer261 associated with PIN1, a prolyl isomerase that may induce conformational changes to confer uncharacterized PD-1 function, such as altering signal transduction, gene transcription or protein stability (Figure 3.9b)[172,173]. Together, these findings not only confirm previous reports in the literature, but strongly suggest that PD-1 retains novel functions, specifically governed by the ITIM and phospho-serine sites, that require further investigation.

In summary, we believe these findings have substantially increased our understanding of PD-1-mediated signaling and strongly encourage future analysis, as many questions about these proposed mechanisms remain. In particular, the mechanism by which PD-1 inhibits PIEZO1 activity and the fate of PIEZO1-mediate $Ca^{2+}$ influx requires further examination. In addition, the specific roles of the PD-1 ITSM, ITIM, pS-ITIM and pSer261 need to be verified and the function of identified PD-1 binding partners requires clarification. Interestingly, the necessity of actin cytoskeletal dynamics and receptor clustering at the immune synapse for PIEZO1 function and recruitment of cytoskeletal-related proteins by PD-1 may provide a motif through which these findings converge[18,90,105,121,127].

## 4.2 Outlook on PD-1 and PIEZO1 function

*PD-1 impairs F-actin cytoskeletal dynamics to inhibit PIEZO1*

Mechanosensors translate force into biological signals[59,62,63,124]. Like all signaling pathways, molecular mechanisms must be in place to positively and negatively regulate these signals to ensure the cell functions properly[193]. For this reason, mechanosensitive signal transduction likely encounters inhibitory machinery to counter its activity[124]. However, these mechanisms are not well established[63,124]. Our studies are the first

to demonstrate an endogenous mechanism by which mechanically-mediated signaling is inhibited by coinhibitory receptor function. We believe PD-1 ligation interferes with actin-cytoskeletal machinery tethering PIEZO1 within the cell membrane, thereby preventing its activation following TCR ligation[18,90,127]. Our proximity labelling experiments identified PD-1 association with endocytic machinery and membrane trafficking proteins, suggesting that PD-1 disrupts receptor clustering and stability at the immune synapse (Figure 2.1i-j)[18,105,168]. This hypothesis is supported by proteins identified in PD-1 phospho-peptide pulldowns. WASH complex and AP-2 adaptor proteins were specifically recruited to the pS-ITIM (Figure 3.8a-d)[121,166–168]. The WASH complex mediates F-actin nucleation to promote optimal TCR signaling and receptor turnover, while AP-2 adaptor proteins similarly govern clathrin-mediated endocytosis at the immune synapse[121,166–168]. It is possible that these proteins are sequestered by PD-1 following PD-L1 ligation to inhibit F-actin polymerization, thereby abolishing the actinomyosin contractile ring that promotes TCR recycling and likely provides force to gate PIEZO1 in an open conformation[84,94,127,194]. The necessary function of the pS-ITIM in regulating cytoskeletal dynamics may also be reflected in PD-1-mutant-proximity labelling experiments, where PIEZO1 recruitment to PD-1 was not significantly impaired with single pY-ITIM or pY-ITSM mutations (Figure 3.3h). Perhaps, the pS-ITIM is required for PIEZO1 recruitment to PD-1.

To assess the role of pS-ITIM in PD-1 signaling, mutation of this serine site to an inactive glycine or alanine residue will be important for characterizing pS-ITIM function in T cells. Generating pS-ITIM singly mutated cells or in combination with a pY-ITIM mutation will determine if the pS-ITIM functions independently of pY-ITIM or is necessary for pY-ITIM function. In addition, to determine the precise mechanism by which PD-1 inhibits PIEZO1, it will be necessary to assess various functions of the actinomyosin cytoskeleton. Genetic KO studies of WASH complex and AP-2 adaptor proteins would determine if loss of these proteins results in phenotypic similarities to PIEZO1 deficiency that cannot be rescued by PD-1 blockade. Proximity phospho-proteomic studies in Jurkat cells examining PD-1 ligation at different time points using PD-1 mutant pY-ITSM, pY-ITIM and pS-ITIM and combination mutant APEX2 constructs may also unveil changes in phosphorylation of cytoskeletal components induced by PD-1 ligation over time. Additionally, experiments using cytoskeletal disrupting agents, including the inhibitor of actin polymerization cytochalasin

D and myosin II inhibitor blebbistatin, in XLGenEPi Jurkat cells in the presence of TCR/CD28 ligation would determine whether actinomyosin contractile forces are responsible for activating PIEZO1[195,196].

*PD-1 recruits ubiquitin ligases to degrade PIEZO1*

Moreover, our findings suggest that PD-1 may induce the proteasomal degradation of PIEZO1 through activation of NEDD4-like HECT E3 ubiquitin-protein ligases WWP1 and WWP2[107,108]. While WWP1 has been shown to negatively regulate T cell activity through degradation of TGFβ signaling components and T cell homeostasis protein LKLF, the outcome of WWP2 ubiquitination is more diverse[107,133]. WWP2 activity promotes cell survival by targeting negative AKT regulator PTEN and EGR2, a transcription factor involved in T cell activation-induced cell death[130,132]. However, WWP2 in macrophages also targets TRIF to attenuate TLR3-mediated innate immune and inflammatory responses[131]. Still, if PIEZO1 is indeed a target of WWP1 and/or WWP2, PIEZO1 degradation would impair T cell activity based on our findings demonstrating PIEZO1 loss in CD8+ T cells impairs functionality (Figure 2.3b-i, Figure 2.S10?).

Interestingly, we have also observed strong association of WWP1 with ITIM mutant cells that was not observed in ITSM mutant cells, but also not observed in PD-1 WT cells. Since we observed an association of pS-ITIM with WWP2 (data not shown), it is possible that the pY-ITIM and pS-ITIM coordinate feedback mechanisms that control the binding of PD-1 ITIM to specific proteins. In addition, WWP1 and WWP2 have been reported to complex with one another to regulate the balance of transcription factor p73 and its isoform to control cell survival[197]. WWP2 alone degraded p73, but this function was switched when phosphatase PPM1G induced complexing between WWP1 and WWP2, promoting the degradation of the p73 isoform[197]. Perhaps the role of WWP1 and WWP2 is mediated by phosphatases SHP1/2 to regulate its targeting of PIEZO1. Nevertheless, the overlap between PD-1 and PIEZO1 associating with WWP1 and WWP2 provides an additional mechanism by which PD-1 may mediate the degradation of PIEZO1.

Repeating PIEZO1 co-IP experiments with proteasome inhibitors and assessing the ubiquitination status of PIEZO1 in the presence or absence of PD-1 ligation would be useful in determining if PD-1 induces PIEZO1 degradation, while also examining the location of potential ubiquitination sites on PIEZO1. In addition,

developing WWP1, WWP2 and WWP1/2 double knockout Jurkat cells lines using nucleofection of Cas9 and optimized sgRNAs would allow for the assessment of PIEZO1 surface expression and ubiquitination in the presence or absence of PD-1 ligation. These experiments would determine if WWP1 and WWP2 E3 ligases are responsible for promoting the proteasomal degradation of PIEZO1, and potentially other TCR-related proteins, and can be repeated in primary murine or human CD8^{+} T cells.  Monitoring phosphorylation of WWP1 and WWP2 following PD-1 ligation in SHP1/2 WT and KO cells would also determine if SHP1/2 regulate WWP1 and WWP2 function. Lastly, since the pS-ITIM has exhibited function in binding cytoskeletal and ubiquitin ligase machinery, it would be telling to evaluate PIEZO1 function and association with PD-1 in a doubly mutated pY-ITIM/pS-ITIM cell line, as described above.

*PIEZO1-mediated Ca$^{2+}$ flux activates calpain proteases to modulate F-actin*

While we have demonstrated that PIEZO1 is a major target of PD-1-mediated inhibition, questions remain regarding the precise role of PIEZO1 activity in CD8^{+} T cells. In particular, why is PIEZO1-induced Ca$^{2+}$ influx necessary for T cell function among numerous CRAC and voltage-gated ion channels expressed in T cells? CRAC channel activation, specifically through ORAI1, is well characterized in T cells and occurs upon TCR ligation through PLC$\gamma$ generation of inositol triphosphate (IP$_3$)[114,116,117,121]. IP$_3$ binds receptors in the  endoplasmic reticulum (ER), which empties Ca$^{2+}$ stores and induces the translocation of stromal interaction molecule 1 (STIM1) to ORAI1, resulting in channel activation and extracellular Ca$^{2+}$ influx[114,116,117,121]. This process occurs in seconds and persists to induce NFAT localization to the nucleus and subsequent gene transcription[121,127]. It is important to note that ORAI channels do not localize at the immune synapse and have been shown to form dense cap-like structures distal to the TCR[198]. Thus, the precise mechanisms by which sustained actin polymerization and Ca$^{2+}$ influx form a positive feedback loop to promote stability at the immune synapse and continued gene transcription are unclear[121,127]. Given our observation that PIEZO1 activity is induced upon TCR and CD28 ligation, it is likely that actinomyosin contractile forces at the immune synapse stimulated by TCR ligation gate PIEZO1 in an open conformation (Figure 2.2e-f)[84,90]. Subsequent Ca$^{2+}$ influx by PIEZO1 in turn activates calpain proteases that continue to modify F-actin to maintain stable contact at the immune synapse through F-actin retrograde flow, which can persist on the order of minutes to hours[64,90,95,121,127]. In this way, PIEZO1-mediated Ca$^{2+}$ influx may

govern cytoskeletal dynamics that stabilize the immune synapse to promote optimal TCR signaling, which promotes PLCγ and CRAC channel activity.

This hypothesis emphasizes the importance of localization for $Ca^{2+}$ transporters and effector proteins such that specific regions of protein localization may determine the differential signaling outputs of $Ca^{2+}$ influx [134]. To confirm that calpains are indeed effectors of PIEZO1-mediated $Ca^{2+}$ influx, calpain activity assays should be performed in PIEZO1 WT and KO CD8^{+} T cells ligated with TCR-control and TCR-PD-L1 beads, as well as PIEZO1 agonist Yoda1. In addition, to uncouple PIEZO1-mediated $Ca^{2+}$ influx from CRAC channel-mediated $Ca^{2+}$ influx, CRAC channel and PLCγ inhibitors, as well as PIEZO1 agonists and antagonists, would serve as useful tools for probing the activity of each pathway under varying stimulation conditions[199]. Readouts for these experiments may include phospho-flow cytometry, $Ca^{2+}$ flux assays with cell permeable $Ca^{2+}$ dyes or Western blotting analysis of phosphorylated proteins (Chapter 2.4). These studies would also determine if PIEZO1-mediated $Ca^{2+}$ influx influences downstream effector pathways in addition to cytoskeletal dynamics, as we observed increases in ERK phosphorylation following PD-1 agonism (Figure 2.S6c-d).

*PIEZO1 activity impacts CD8^{+} T cell fate*

Our studies have revealed alterations in Slamf6 and TIM-3 expression in CD8^{+} TILs depending on the mode of PIEZO1 regulation (Figure 2.3f,I and Figure 2.4g). PIEZO1 KO CD8^{+} TILs exhibited a more progenitor-exhausted phenotype marked by Slamf6 expression, while PIEZO1 agonized CD8^{+} TILs displayed a more terminally exhausted phenotype marked by TIM-3 expression and granzyme B expression[122,123]. The simple explanation for this observation is that PIEZO1 is necessary for T cell activation where it responds to force generated by actin cytoskeletal rearrangements to promote strong coupling between the TCR and MHCI/II at the immune synapse[84,90,95]. For this reason, loss of PIEZO1 may result in suboptimal T cell activation that, in turn, impairs downstream gene transcription for acquisition of effector functions. However, previous reports of calpain function may provide a more specific explanation for differences observed in TCF1-mediated gene transcription[137–139,141]. Calpain proteases have been shown to bind and degrade B-catenin, which is a co-activator of TCF1 genes[137–139,141]. It is possible that PIEZO1-mediated activation of calpain

induces β-catenin degradation, impairing the expression of TCF1 genes, including Slamf6, and promoting TIM-3 upregulation. Alternatively, calpain proteases may not be activated when PIEZO1 function is lacking, thereby allowing for the association of β-catenin with TCF1 to maintain Slamf6 expression. Similarly, PD-1 has been shown to protect an early TCF1+ CD8+ T cell subset in chronic viral infection, suggesting that PD-1-mediated inhibition of PIEZO1, similar to PIEZO1 KO in CD8+ T cells, correlates with increased Slamf6 expression [142].

This hypothesis is also supported by data demonstrating that CRAC channels do not regulate TCF1 gene expression[117], suggesting a unique function for PIEZO1 $Ca^{2+}$ influx. Persistent cytoskeletal forces described above may sustain PIEZO1 activity long enough to modify specific gene transcription[73,124]. Studies examining the localization and expression of β-catenin at the protein level in PIEZO1 WT, KO or PIEZO1-agonized CD8+ T cells would be necessary to determine if PIEZO1 activity induces β-catenin export from the nucleus and degradation. These experiments could also be performed in the presence or absence of calpain inhibitors or with genetic KO of calpains to confirm that calpain activity is indeed necessary for β-catenin degradation[200]. In addition, complementary single cell RNA-sequencing analysis of PIEZO1 WT and KO CD8+ TILs may provide useful information regarding the abundance of transcripts relating to TCF1 gene expression, as well as other alterations in gene expression. It would be interesting to study the kinetics of gene expression throughout the course of disease by harvesting CD8+ TILs from CD8+ PIEZO1 WT and KO mice at various time points, for example on days 5, 10, 15 and 20 following tumor implantation.

*External force may govern unique PIEZO1 activity*

Lastly, many studies have characterized PIEZO1 response to external forces in the absence of intracellular actin cytoskeleton regulation[66,77,79,115,201]. We also observed increases in CD8+ T cell signaling with exposure to cyclical hydrostatic pressure alone (Figure 2.S6g-i). In addition, PIEZO1-agonized CD8+ T cells exhibit increased ERK phosphorylation in the absence of TCR stimulation (Figure 2.S6c-d). Notably, PIEZO1 agonist Yoda1 functions as a gating modifying to wedge PIEZO1 in its open conformation, obviating the need for actin-mediated activation[113]. Therefore, it is important to determine if force-from-lipid translates to unique T cell functions compared to force-from-filament described in this thesis (Figure 1.2)[83].

Exposing PIEZO1 WT and KO CD8^{+} T cells to various sources of external pressure, including, cyclical hydrostatic pressure and shear flow, should be performed to probe this question further. Specific readouts to consider are signaling pathway analysis using phospho-flow cytometry or Western blotting, RNA-sequencing analysis to study transcriptional alterations, cytokine production analyses using CBA assays, immune-cell receptor expression using flow cytometry and metabolic rewiring using the Seahorse metabolic flux assay (Agilent).

## 4.3 Hypothetical model of PD-1 signaling motifs

*PD-1 ITSM recruits SHP1, SHP2 and CSK to mediate inhibitory signaling*

Prior to the signaling studies outlined in this thesis, PD-1 was reported to contain two tyrosine phosphorylation motifs that propagate inhibitory signals as well as a ubiquitin binding motif that regulates PD-1 surface expression and degradation[48,52]. Our data has substantially added to the repertoire of signaling capabilities exhibited by PD-1. We have confirmed that the ITSM chiefly recruits effector phosphatases and kinases to dampen T cell activity. Specifically, SHP2 and to a lesser extent, SHP1 and CSK associate with the ITSM (Figure 3.5a-b and Figure 3.6a-b,e). Our studies suggest that SHP2 is the primary mediator of PD-1 signaling. Still, the function of SHP1 association has not been clarified. It is possible that SHP1 activation is a compensatory mechanism for SHP2. However, its recruitment to the cytoplasmic tail is observed in tandem with SHP2, suggesting that it governs a distinct role. While previous studies have attempted to reconcile the different functions of SHP1 and SHP2 in relation to PD-1-mediated inhibition, no unified model has emerged[14,19].

Studies examining catalytic-dead constructs of SHP2 and SHP1 would be useful in assessing the target proteins associated with each phosphatase. Catalytic-dead constructs lacking phosphatase activity would be less likely to impair T cell viability and function, given the necessity of each phosphatase for T cell function. In particular, phospho-proteomic studies in T cells expressing SHP1/2 mutants in the presence or absence of PD-1 ligation may unveil the particular proteins targeted by each phosphatase. Similarly, a catalytic-dead CSK mutant would aid in determining what proteins are specifically inactivated via phosphorylation following PD-1 ligation. Comparing these results with phospho-proteomic studies

performed on PD-1 ITIM, ITSM and phospho-serine mutants would verify the role of the ITSM in mediating these signaling events.

*Proteomic methodology unveils novel PD-1 function*

While our studies confirmed the necessity of the ITSM in recruiting effector phosphatases SHP1/2 and kinase CSK, we also identified multiple unique binders of the ITIM. These findings introduce various mechanisms by which the ITIM functions on PD-1, which previous studies have been unable to characterize. Moreover, identification of the novel phospho-serine site upstream of the ITIM suggests that this motif is necessary for optimal ITIM function. We found that the pY-ITIM peptide strongly associates with UBASH3B and, to a lesser extent, UBASH3A and Cbl-b, while mutation of the ITIM most notably diminished association with these proteins compared to mutation of the ITSM (Figure 3.3j-l and Figure 3.7a-c). Together, Cbl-b and UBASH3A/B comprise ubiquitin ligase machinery that has been reported to negatively regulate T cell activation signals through proteasomal degradation. Still, mutation in the pY-ITIM alone is not sufficient for reversing PD-1-mediated inhibition. Thus, it is possible that pY-ITIM degrades proteins that are inactivated by pY-ITSM mediators described above, implying that the ITIM depends on ITSM function. This inactivation-degradation hypothesis has been postulated above for PD-1 dual regulation of PIEZO1 where interference in actin cytoskeletal rearrangements inhibits PIEZO1 and recruitment of WWP1 and/or WWP2 promotes the degradation of PIEZO1. To further study this model, proteomic ubiquitin profiling could be used to assess differences in protein ubiquitination between ITIM and ITSM mutant cells treated with a proteasome inhibitor in the presence or absence of PD-1 ligation[182,183]. Demonstrating that ITIM mutant cells lack ubiquitinated proteins observed in WT cells would verify that the ITIM indeed regulates protein degradation.

Our PD-1 mutant proximity labelling studies suggest that overall protein recruitment to PD-1 is attenuated with a mutation in the ITIM (Figure 3.3c-l). It is also important to note that the pY-ITIM peptides bind less efficiently to proteins that strongly associate with pS-ITIM, suggesting that both phosphorylation events are necessary for optimal ITIM function (Figure 3.8). Generating a pY-ITIM and pS-ITIM doubly mutated cell line as well as a singly mutated pS-ITIM cell line would aid in studying receptor clustering dynamics

mediated by PD-1 at the immune synapse, and also would determine if the pS-ITIM functions independently of pY-ITIM. TIRF live cell imaging of PD-1 WT, pY-ITSM, pY-ITIM, pS-ITIM and pY/pS-ITIM mutant cells ligated with CD3 and CD28 crosslinking antibodies in the presence or absence of PD-L1 ligation would illustrate PD-1 clustering dynamics in real time.

PD-1 proximity phospho-proteomics identified the phosphorylation of pSer261 on the cytoplasmic tail of PD-1 following ligation. Subsequent PD-1 phospho-peptide pulldowns of pSer261 identified a strong association of this peptide with PIN1 and TNKS-1 compared to unphosphorylated peptide controls and other PD-1 signaling motifs. While it is difficult to link PD-1 to TNKS-1, a PARP protein, PIN1 has been reported to regulate various mechanisms, including protein stability, degradation, localization and transcription factor activity, that may contribute to PD-1 function[171–173]. In addition, PIN1 has been implicated in driving tumorigenesis in breast and gynecological cancers through the regulation of various signaling pathways[172]. Specifically, PIN1 has been shown to regulate proteins in the AKT and MAPK pathways, which are both inhibited upon PD-1 ligation[17,172]. Whether PIN1 negatively or positively regulates these signaling pathways in T cells has not been determined. For this reason, genetic KO studies of PIN1 in T cells along with complementary studies mutating pSer261 to glycine or alanine on PD-1 could unveil novel PD-1 function. Experiments surveying alterations in signaling pathways, protein stability, gene transcription and cell cycle progression would be necessary for characterizing the function of PIN1 and PD-1 in T cells.

*PD-1 mutant in vivo models highlight distinct PD-1 functions*

We have shown that mice harboring an inactivating mutation in the PD-1 ITSM control tumor growth and promote CD8^{+} T cell function similar to PD-1 KO mice, while ITIM mutant mice phenotypically resemble WT mice (Figure 3.1). Still, noticeable differences between PD-1 KO and ITSM mutant mice and as well subtle differences between ITIM mutant and WT mice are apparent (Figure 3.1). Moreover, PD-1 WT, KO, ITSM and ITIM mutant CD8^{+} T cells exhibit differences in TCR signaling pathway regulation (Figure 3.2). These observations confirm that the ITSM and ITIM control separate PD-1-mediated functions and imply that additional signaling motifs may contribute top PD-1-mediated inhibition. For this reason, ongoing studies in the Sharpe lab will assess phenotypic alterations in ITIM/ITSM doubly mutated mice (DM). DM mice will be

examined in both cancer and autoimmune disease models to assess how these mice respond to disease pathogenesis compared to ITIM and ITSM mutant mice, as well as PD-1 WT and KO controls. PD-1 DM T cells can also be isolated and studied *in vitro* for residual signaling function using phospho-flow cytometry and RPPA analysis in repeated experiments. These analyses will be particularly interesting given our identification of novel phospho-serine sites on the cytoplasmic tail of PD-1. Noteworthy phenotypes observed in PD-1 DM mice can be correlated with complementary studies examining the function of PD-1 phospho-serine sites described above to characterize the unknown functions of PD-1. Moreover, if the PD-1 DM mouse retains residual PD-1 function, it would be interesting to generate a mouse containing mutations in the ITIM and ITSM, as well as pS-ITIM and pSer261 to determine if this mouse more closely recapitulates full PD-1 KO. These mouse models would not only be useful for studying the effects of PD-1 mutation in CD8$^+$ T cells, but in other T cells, as well. In particular, investigating the function of PD-1 mutation in Treg cells would be interesting since ongoing work in the Sharpe lab has demonstrated that ITSM mutant mice experience alleviated EAE symptoms compared to PD-1 KO mice (data not shown.)

In addition, we, along with other groups, have demonstrated the success of *ex vivo* PD-1-APEX2 proximity labelling[177]. We believe utilizing PD-1-APEX2 proximity labelling and incorporating various PD-1 mutations in the APEX2 construct would be useful for studying PD-1 signaling mechanisms in immune cell subsets throughout the course of disease. Since many of the proposed studies above involve genetic KO of identified hit proteins, the CHIME gene editing method could serve as a very useful and efficient tool for determining the physiological relevance, for example, of WWP1 and WWP2 in regulating the degradation of PIEZO1, as well as the function of WASH and AP-2 complex proteins in PD-1-mediated inhibition, obviating the need to generate mouse models[176]. If CHIME experiments prove interesting, genetic mouse models can be considered for further experimentation.

Finally, we recognize that the completed and proposed experiments outlined in this thesis focus primarily on PD-L1 ligation of PD-1. However, PD-L2 is another well-characterized ligand of PD-1[2,33–35]. The differential expression and structure of PD-L2 compared to PD-L1 imply that PD-L2 may regulate distinct mechanisms that drive PD-1-mediated inhibition[2,202]. For this reason, we recommend exploring the *in vitro*

signaling platforms and *in vivo* models described in this thesis to determine if PD-L2 induces unique PD-1 signaling dynamics.

## 4.4 Concluding remarks

As has been emphasized above, further studies are necessary to answer remaining questions about PD-1 signaling. Still, we believe this body of research has made significant strides in improving our understanding of PD-1-mediated inhibition. The data discussed in this thesis highlight four significant implications. First, mechanosensation by PIEZO1 is required for optimal CD8$^+$ T cell function, suggesting that this molecule may serve as a potential target for immunotherapy. Second, PD-1 ligation inhibits PIEZO1 activity, suggesting that T cells, among other cell types, possess novel endogenous mechanisms to counter mechano-mediated signaling. Third, tyrosine and serine phosphorylation sites on the cytoplasmic tail of PD-1 exhibit unique binding behavior, suggesting that uncharacterized signaling mechanisms of PD-1 exist and require further examination. Fourth, proteomic methodology is extremely valuable for studying immune cell receptor signaling and should be applied to receptors for which signaling remains unclear. Overall, the findings in this thesis further clarify the diverse mechanisms by which PD-1 functions to attenuate T cell signaling.

**Bibliography**

1.    Sharpe, A. H. & Pauken, K. E. The diverse functions of the PD1 inhibitory pathway. *Nat. Publ. Gr.* (2017). doi:10.1038/nri.2017.108

2.    Keir, M. E., Butte, M. J., Freeman, G. J. & Sharpe, A. H. PD-1 and Its Ligands in Tolerance and Immunity. *Annu. Rev. Immunol.* **26**, 677–704 (2008).

3.    Chen, L. & Flies, D. B. Molecular mechanisms of T cell co-stimulation and co-inhibition. *Nat. Rev. Immunol.* **13**, 227–242 (2013).

4.    Baumeister, S. H., Freeman, G. J., Dranoff, G. & Sharpe, A. H. Coinhibitory Pathways in Immunotherapy for Cancer. *Annu. Rev. Immunol.* **34**, 539–573 (2016).

5.    Esensten, J. H., Helou, Y. A., Chopra, G., Weiss, A. & Bluestone, J. A. CD28 Costimulation: From Mechanism to Therapy. *Immunity* **44**, 973–988 (2016).

6.    Mueller, D. L., Jenkins, M. K. & Schwartz, R. H. Clonal Expansion Versus Functional Clonal Inactivation: A Costimulatory Signalling Pathway Determines the Outcome of T Cell Antigen Receptor Occupancy. *Annu. Rev. Immunol.* **7**, 445–480 (1989).

7.    Brownlie, R. J. & Zamoyska, R. REVIEWS T cell receptor signalling networks : branched , diversified and bounded. *Nat. Publ. Gr.* **13**, 257–269 (2013).

8.    Merwe, P. A. Van Der & Dushek, O. Mechanisms for T cell receptor triggering. *Nat. Publ. Gr.* **11**, 47–55 (2010).

9.    Acuto, O. & Michel, F. CD28-mediated co-stimulation: a quantitative support for TCR signalling. *Nat. Rev. Immunol.* **3**, 939–951 (2003).

10.   Bretscher, P. & Cohn, M. A Theory of Self-Nonself Discrimination Author ( s ): Peter Bretscher and Melvin Cohn Published by : American Association for the Advancement of Science. *Science.* **169**, 1042–1049 (1970).

11.   June, C. H., Ledbetter, J. A., Gillespie, M. M., Lindsten, T. & Thompson, C. B. T-cell proliferation involving the CD28 pathway is associated with cyclosporine-resistant interleukin 2 gene expression. *Mol. Cell. Biol.* **7**, 4472–4481 (1987).

12.   Schwartz, R. H. T cell anergy. *Annu. Rev. Immunol.* **21**, 305–334 (2003).

13.   Ishida, Y., Agata, Y., Shibahara, K. & Honjo, T. Induced expression of PD-1, a novel member of the immunoglobulin gene superfamily, upon programmed cell death. *EMBO J.* **11**, 3887–95 (1992).

14.   Chemnitz, J. M., Parry, R. V, Nichols, K. E., June, H. & Riley, J. L. SHP-1 and SHP-2 Associate with Immunoreceptor Tyrosine-Based Switch Motif of Programmed Death 1 upon Primary Human T Cell Stimulation, but Only Receptor Ligation Prevents T Cell Activation of. *J. Immunol.* 945–954 (2004). doi:10.4049/jimmunol.173.2.945

15.   Sheppard, K. A. *et al.* PD-1 inhibits T-cell receptor induced phosphorylation of the ZAP70/CD3 signalosome and downstream signaling to PKC. *FEBS Lett.* **574**, 37–41 (2004).

16.   Hui, E. *et al.* T cell costimulatory receptor CD28 is a primary target for PD-1 – mediated inhibition. *Science (80-. ).* **4**, 1428–1433 (2017).

17.    Boussiotis, V. A. Molecular and Biochemical Aspects of the PD-1 Checkpoint Pathway. *N. Engl. J. Med.* **375**, 1767–1778 (2016).

18.    Ambler, R., Edmunds, G., Toti, G., Morgan, D. & Wülfing, C. PD-1 suppresses the maintenance of cell couples between cytotoxic T cells and tumor target cells within the tumor. *Sci. Signal.* **4518**, 443788 (2020).

19.    Yokosuka, T. *et al.* Programmed cell death 1 forms negative costimulatory microclusters that directly inhibit T cell receptor signaling by recruiting phosphatase SHP2. *J. Exp. Med.* **209**, 1201–1217 (2012).

20.    Patsoukis, N. *et al.* PD-1 alters T-cell metabolic reprogramming by inhibiting glycolysis and promoting lipolysis and fatty acid oxidation. *Nat. Commun.* **6**, 1–13 (2015).

21.    Barber, D. L. *et al.* Restoring function in exhausted CD8 T cells during chronic viral infection. *Nature* **439**, 682–687 (2006).

22.    Juneja, V. R. *et al.* PD-L1 on tumor cells is sufficient for immune evasion in immunogenic tumors and inhibits CD8 T cell cytotoxicity. *J. Exp. Med.* **214**, 895–904 (2017).

23.    LaFleur, M. W., Muroyama, Y., Drake, C. G. & Sharpe, A. H. Inhibitors of the PD-1 Pathway in Tumor Therapy. *J. Immunol.* **200**, 375–383 (2018).

24.    Motzer, R. J. *et al.* Nivolumab versus Everolimus in Advanced Renal-Cell Carcinoma. *N. Engl. J. Med.* **373**, 1803–1813 (2015).

25.    Melero, I. *et al.* Evolving synergistic combinations of targeted immunotherapies to combat cancer. *Nat. Rev. Cancer* **15**, 457–72 (2015).

26.    Garon, E. B. *et al.* Pembrolizumab for the Treatment of Non–Small-Cell Lung Cancer. *N. Engl. J. Med.* **372**, 2018–2028 (2015).

27.    Brahmer, J. R. *et al.* Phase I study of single-agent anti-programmed death-1 (MDX-1106) in refractory solid tumors: Safety, clinical activity, pharmacodynamics, and immunologic correlates. *J. Clin. Oncol.* **28**, 3167–3175 (2010).

28.    Smith, C. A., Williams, G. T., Kingston, R., Jenkinson, E. J. & Owen, J. J. T. Antibodies to CD3/T-cell receptor complex induce death by apoptosis in immature T cells in thymic cultures. *Nature* **337**, 181–184 (1989).

29.    Agata, Y. *et al.* Expression of the PD-1 antigen on the surface of stimulated mouse T and B lymphocytes. *Int. Immunol.* **8**, 765–772 (1996).

30.    Okazaki, T., Maeda, A., Nishimura, H., Kurosaki, T. & Honjo, T. PD-1 immunoreceptor inhibits B cell receptor- mediated signaling by recruiting src homology 2-domain-containing tyrosine phosphatase 2 to phosphotyrosine. *Proc. Natl. Acad. Sci.* **98**, 13866–13871 (2001).

31.    Nishimura, H., Nose, M., Hiai, H., Minato, N. & Honjo, T. Development of lupus-like autoimmune diseases by disruption of the PD-1 gene encoding an ITIM motif-carrying immunoreceptor. *Immunity* **11**, 141–151 (1999).

32.    Vibhakar, R., Juan, G., Traganos, F., Darzynkiewicz, Z. & Finger, L. R. Activation-induced expression of human programmed death-1 gene in T- lymphocytes. *Exp. Cell Res.* **232**, 25–28 (1997).

33. Freeman, G. J. *et al.* Engagement of the PD-1 immunoinhibitory receptor by a novel B7 family member leads to negative regulation of lymphocyte activation. *J. Exp. Med.* **192**, 1027–1034 (2000).

34. Latchman, Y. *et al.* PD-L2 is a second ligand for PD-1 and inhibits T cell activation. *Nat. Immunol.* **2**, 261–268 (2001).

35. Tseng, S. Y. *et al.* B7-DC, a new dendritic cell molecule with potent costimulatory properties for T cells. *J. Exp. Med.* **193**, 839–845 (2001).

36. Keir, M. E. *et al.* Tissue expression of PD-L1 mediates peripheral T cell tolerance. *J. Exp. Med.* **203**, 883–895 (2006).

37. Keir, M. E., Latchman, Y. E., Freeman, G. J. & Sharpe, A. H. Programmed Death-1 (PD-1):PD-Ligand 1 Interactions Inhibit TCR-Mediated Positive Selection of Thymocytes. *J. Immunol.* **175**, 7372–7379 (2005).

38. Keir, M. E., Freeman, G. J. & Sharpe, A. H. PD-1 Regulates Self-Reactive CD8 + T Cell Responses to Antigen in Lymph Nodes and Tissues . *J. Immunol.* **179**, 5064–5070 (2007).

39. Leach, D. R., Krummel, M. F. & Allison, J. P. Enhancement of Antitumor Immunity by CTLA-4 Blockade. *Science (80-. ).* **271**, 1734–1736 (1996).

40. Konishi, J. *et al.* B7-H1 expression on non-small cell lung cancer cells and its relationship with tumor-infiltrating lymphocytes and their PD-1 expression. *Clin. Cancer Res.* **10**, 5094–5100 (2004).

41. Hamanishi, J. *et al.* Programmed cell death 1 ligand 1 and tumor-infiltrating CD8+ T lymphocytes are prognostic factors of human ovarian cancer. *Proc. Natl. Acad. Sci. U. S. A.* **104**, 3360–3365 (2007).

42. Nomi, T. *et al.* Clinical significance and therapeutic potential of the programmed death-1 ligand/programmed death-1 pathway in human pancreatic cancer. *Clin. Cancer Res.* **13**, 2151–2157 (2007).

43. Strome, S. E. *et al.* B7-H1 blockade augments adoptive T-cell immunotherapy for squamous cell carcinoma. *Cancer Res.* **63**, 6501–6505 (2003).

44. Tyler, C. Blockade of B7-H1 improves myeloid dendritic cell – mediated antitumor immunity. *Nat. Med.* **9**, 562–567 (2003).

45. Hodi, S. *et al.* Improved Survival with Ipilimumab in Patients with Metastatic Melanoma. *N. Engl. J. Med.* **363**, 711–723 (2010).

46. Ribas, A. Anti-CTLA4 antibody clinical trials in melanoma. *Update Cancer Ther.* **2**, 133–139 (2007).

47. Haanen, J. B. A. G. *et al.* Management of toxicities from immunotherapy: ESMO Clinical Practice Guidelines for diagnosis, treatment and follow-up†. *Ann. Oncol.* **28**, iv119–iv142 (2017).

48. Riley, J. L. PD-1 signaling in primary T-cells. *immunol rev* **229**, 114–125 (2009).

49. Parry, R. V *et al.* CTLA-4 and PD-1 Receptors Inhibit T-Cell Activation by Distinct Mechanisms CTLA-4 and PD-1 Receptors Inhibit T-Cell Activation by Distinct Mechanisms †. *Mol. Cell. Biol.* **25**, 9543–9553 (2005).

50. Peled, M. *et al.* Affinity purification mass spectrometry analysis of PD-1 uncovers SAP as a new checkpoint inhibitor. *Proc. Natl. Acad. Sci.* 201710437 (2017). doi:10.1073/pnas.1710437115

51. Rota, G. *et al.* Shp-2 Is Dispensable for Establishing T Cell Exhaustion and for PD-1 Signaling In Vivo. *Cell Rep.* **23**, 39–49 (2018).

52. Meng, X. *et al.* FBXO38 mediates PD-1 ubiquitination and regulates anti-tumour immunity of T cells. *Nature* 1 (2018). doi:10.1038/s41586-018-0756-0

53. Kamphorst, A. O. *et al.* Rescue of exhausted CD8 T cells by PD-1 – targeted therapies is CD28-dependent. *Science (80-. ).* **355**, 1423–1427 (2017).

54. Patsoukis, N. *et al.* Selective Effects of PD-1 on Akt and Ras Pathways Regulate Molecular Components of the Cell Cycle and Inhibit T Cell Proliferation. *Sci. Signal.* **5**, 1–14 (2012).

55. Patsoukis, N., Li, L., Sari, D., Petkova, V. & Boussiotis, A. PD-1 Increases PTEN Phosphatase Activity While Decreasing PTEN Protein Stability by Inhibiting Casein Kinase 2. *Mol. Cell. Biol.* **33**, 3091–3098 (2013).

56. Quigley, M. *et al.* Transcriptional analysis of HIV-specific CD8+ T cells shows that PD-1 inhibits T cell function by upregulating BATF. *Nat. Med.* **16**, 1147–1151 (2010).

57. Brunner-Weinzierl, M. C. & Rudd, C. E. CTLA-4 and PD-1 control of T-cell motility and migration: Implications for tumor immunotherapy. *Front. Immunol.* **9**, 1–8 (2018).

58. Thurber, G. M., Schmidt, M. M. & Wittrup, K. D. Antibody tumor penetration. *Adv Drug Deliv Rev* **60**, (2008).

59. Huse, M. Mechanical forces in the immune system. *Nat. Rev. Immunol.* **17**, 679–690 (2017).

60. McWhorter, F. Y., Davis, C. T. & Liu, W. F. Physical and mechanical regulation of macrophage phenotype and function. *Cell. Mol. Life Sci.* **72**, 1303–1316 (2015).

61. Hsiai, T. K. *et al.* Monocyte recruitment to endothelial cells in response to oscillatory shear stress. *FASEB J.* **17**, 1648–1657 (2003).

62. Mohammed, D. *et al.* Innovative tools for mechanobiology: Unraveling outside-in and inside-out mechanotransduction. *Front. Bioeng. Biotechnol.* **7**, (2019).

63. Holle, A. W. & Engler, A. J. More than a feeling: Discovering, understanding, and influencing mechanosensing pathways. *Curr. Opin. Biotechnol.* **22**, 648–654 (2011).

64. Aglialoro, F., Hofsink, N., Hofman, M., Brandhorst, N. & van den Akker, E. Inside Out Integrin Activation Mediated by PIEZO1 Signaling in Erythroblasts. *Front. Physiol.* **11**, 1–10 (2020).

65. Nonomura, K. *et al.* Mechanically activated ion channel PIEZO1 is required for lymphatic valve formation. *Proc. Natl. Acad. Sci. U. S. A.* **115**, 12817–12822 (2018).

66. Coste, B. *et al.* Piezo1 and Piezo2 Are Essential Components of Distinct Mechanically Activated Cation Channels. *Science* **330**, 55–60 (2010).

67. García-Añoveros, J. & Corey, D. THE MOLECULES OF MECHANOSENSATION. *Annu. Rev. Neurosci.* **20**, 567–594 (1997).

68. Ranade, S. S. *et al.* Piezo1, a mechanically activated ion channel, is required for vascular development in mice. *Proc. Natl. Acad. Sci. U. S. A.* **111**, 10347–10352 (2014).

69. Wang, L. *et al.* Mechanical sensing protein PIEZO1 regulates bone homeostasis via osteoblast-osteoclast crosstalk. *Nat. Commun.* **11**, 1–12 (2020).

70. Morley, L. C. *et al.* Piezo1 channels are mechanosensors in human fetoplacental endothelial cells. *Mol. Hum. Reprod.* **24**, 510–520 (2018).

71. Huo, L. *et al.* Piezo2 channel in nodose ganglia neurons is essential in controlling hypertension in a pathway regulated directly by Nedd4-2. *Pharmacol. Res.* **164**, 105391 (2021).

72. Nonomura, K. *et al.* Piezo2 senses airway stretch and mediates lung inflation-induced apnoea. *Nature* **541**, 176–181 (2017).

73. Solis, A. G. *et al.* Mechanosensation of cyclical force by PIEZO1 is essential for innate immunity. *Nature* (2019). doi:10.1038/s41586-019-1485-8

74. Aykut, B. *et al.* Targeting Piezo1 unleashes innate immunity against cancer and infectious disease. *Sci. Immunol.* **5**, 1–13 (2020).

75. Ma, S. *et al.* Common PIEZO1 Allele in African Populations Causes RBC Dehydration and Attenuates Plasmodium Infection. *Cell* **173**, 443-455.e12 (2018).

76. Segel, M. *et al.* Niche stiffness underlies the ageing of central nervous system progenitor cells. *Nature* (2019). doi:10.1038/s41586-019-1484-9

77. Lin, Y.-C. *et al.* Force-induced conformational changes in PIEZO1. *Nature* (2019). doi:10.1038/s41586-019-1499-2

78. Wang, L. *et al.* Structure and mechanogating of the mammalian tactile channel PIEZO2. *Nature* (2019). doi:10.1038/s41586-019-1505-8

79. Yang, X. *et al.* Structure deformation and curvature sensing of PIEZO1 in lipid membranes. *Nature* **604**, (2022).

80. Ge, J. *et al.* Architecture of the mammalian mechanosensitive Piezo1 channel. *Nature* **527**, 64–69 (2015).

81. Gnanasambandam, R., Bae, C., Gottlieb, P. A. & Sachs, F. Ionic selectivity and permeation properties of human PIEZO1 channels. *PLoS One* **10**, 1–16 (2015).

82. Cox, C. D. *et al.* Removal of the mechanoprotective influence of the cytoskeleton reveals PIEZO1 is gated by bilayer tension. *Nat. Commun.* **7**, 1–13 (2016).

83. Ridone, P., Vassalli, M. & Martinac, B. Piezo1 mechanosensitive channels: what are they and why are they important. *Biophys. Rev.* **11**, 795–805 (2019).

84. Nourse, J. L. & Pathak, M. M. How cells channel their stress: Interplay between Piezo1 and the cytoskeleton. *Semin. Cell Dev. Biol.* **71**, 3–12 (2017).

85. Swaminathan, V., Alushin, G. M. & Waterman, C. M. Mechanosensation: A Catch Bond That Only Hooks One Way. *Curr. Biol.* **27**, R1158–R1160 (2017).

86. Goychuk, I. & Hänggi, P. Ion channel gating: A first-passage time analysis of the Kramers type. *Proc. Natl. Acad. Sci. U. S. A.* **99**, 3552–3556 (2002).

87. Hennes, A. *et al.* Functional expression of the mechanosensitive PIEZO1 channel in primary endometrial epithelial cells and endometrial organoids. *Sci. Rep.* **9**, 1–14 (2019).

88. Romac, J. M. J., Shahid, R. A., Swain, S. M., Vigna, S. R. & Liddle, R. A. Piezo1 is a mechanically activated ion channel and mediates pressure induced pancreatitis. *Nat. Commun.* **9**, 1–10 (2018).

89. Miyamoto, T. *et al.* Functional role for Piezo1 in stretch-evoked Ca2+ influx and ATP release in Urothelial cell cultures. *J. Biol. Chem.* **289**, 16565–16575 (2014).

90. Liu, C. S. C. *et al.* Cutting Edge: Piezo1 Mechanosensors Optimize Human T Cell Activation. *J. Immunol.* **200**, 1255–1260 (2018).

91. Jairaman, A. *et al.* Piezo1 channels restrain regulatory T cells but are dispensable for effector CD4+ T cell responses. *Sci. Adv.* **7**, (2021).

92. Gardel, M. L., Schneider, I. C., Aratyn-Schaus, Y. & Waterman, C. M. Mechanical integration of actin and adhesion dynamics in cell migration. *Annu. Rev. Cell Dev. Biol.* **26**, 315–333 (2010).

93. Finger, E. B. *et al.* Adhesion through L-selectin requires a threshold hydrodynamic shear. *Nature* **379**, 266–269 (1996).

94. Rossy, J., Laufer, J. M. & Legler, D. F. Role of mechanotransduction and tension in t cell function. *Front. Immunol.* **9**, 1–11 (2018).

95. Kumari, S., Curado, S., Mayya, V. & Dustin, M. L. T cell antigen receptor activation and actin cytoskeleton remodeling. *Biochim. Biophys. Acta - Biomembr.* **1838**, 546–556 (2014).

96. Judokusumo, E., Tabdanov, E., Kumari, S., Dustin, M. L. & Kam, L. C. Mechanosensing in T lymphocyte activation. *Biophys. J.* **102**, L5–L7 (2012).

97. Ma, R. *et al.* DNA probes that store mechanical information reveal transient piconewton forces applied by T cells. *Proc. Natl. Acad. Sci.* **116**, 201904034 (2019).

98. Basu, R. *et al.* Cytotoxic T Cells Use Mechanical Force to Potentiate Target Cell Killing. *Cell* **165**, 100–110 (2016).

99. Tamzalit, F. *et al.* Interfacial actin protrusions mechanically enhance killing by cytotoxic T cells. *Sci. Immunol.* **4**, (2019).

100. Chen, D. S. & Mellman, I. Oncology meets immunology: The cancer-immunity cycle. *Immunity* **39**, 1–10 (2013).

101. Chang, J. E., Buechler, M. B., Gressier, E., Turley, S. J. & Carroll, M. C. Mechanosensing by Peyer's patch stroma regulates lymphocyte migration and mucosal antibody responses. *Nat. Immunol.* **20**, 1506–1516 (2019).

102. Hung, V. *et al.* Spatially resolved proteomic mapping in living cells with the engineered peroxidase APEX2. *Nat. Protoc.* **11**, 456–475 (2016).

103. Paek, J. *et al.* Multidimensional Tracking of GPCR Signaling via Article Multidimensional Tracking of GPCR Signaling via Peroxidase-Catalyzed Proximity Labeling. *Cell* **169**, 338-349.e11 (2017).

104. Ting, L., Rad, R., Gygi, S. P. & Haas, W. MS3 eliminates ratio distortion in isobaric multiplexed quantitative proteomics. *Nat. Methods* **8**, 937–940 (2011).

105. Onnis, A. & Baldari, C. T. Orchestration of Immunological Synapse Assembly by Vesicular Trafficking. *Front. Cell Dev. Biol.* **7**, 1–12 (2019).

106. Yu, Q. *et al.* Sample multiplexing for targeted pathway proteomics in aging mice. *Proc. Natl. Acad. Sci. U. S. A.* **117**, 9723–9732 (2020).

107. Bonnevier, J. L., Zhang, R. & Mueller, D. L. E3 ubiquitin ligases and their control of T cell autoreactivity. *Arthritis Res. Ther.* **7**, 233–242 (2005).

108. Ingham, R. J., Gish, G. & Pawson, T. The Nedd4 family of E3 ubiquitin ligases: Functional diversity within a common modular architecture. *Oncogene* **23**, 1972–1984 (2004).

109. Jacinto, E. *et al.* Mammalian TOR complex 2 controls the actin cytoskeleton and is rapamycin insensitive. *Nat. Cell Biol.* **6**, 1122–1128 (2004).

110. Xu, J. *et al.* mTORC2 regulates mechanically induced cytoskeletal reorganization and lineage selection in marrow derived mesenchymal stem cells. *J. Bone Miner. Res.* **1**, 1–14 (2015).

111. Siokis, A., Robert, P. A., Demetriou, P., Dustin, M. L. & Meyer-Hermann, M. F-Actin-Driven CD28-CD80 Localization in the Immune Synapse. *Cell Rep.* **24**, 1151–1162 (2018).

112. Bae, C., Sachs, F. & Gottlieb, P. A. The mechanosensitive ion channel Piezo1 is inhibited by the peptide GsMTx4. *Biochemistry* **50**, 6295–6300 (2011).

113. Botello-Smith, W. M. *et al.* A mechanism for the activation of the mechanosensitive Piezo1 channel by the small molecule Yoda1. *Nat. Commun.* **10**, (2019).

114. Trebak, M. & Kinet, J. P. Calcium signalling in T cells. *Nat. Rev. Immunol.* **19**, 154–169 (2019).

115. Liu, C. S. C. & Ganguly, D. Mechanical cues for T cell activation: Role of piezo1 mechanosensors. *Crit. Rev. Immunol.* **39**, 15–38 (2019).

116. Feske, S., Skolnik, E. Y. & Prakriya, M. Ion channels and transporters in lymphocyte function and immunity. *Nat. Rev. Immunol.* **12**, 532–547 (2012).

117. Vaeth, M., Kahlfuss, S. & Feske, S. CRAC Channels and Calcium Signaling in T Cell-Mediated Immunity. *Trends Immunol.* **41**, 878–901 (2020).

118. Erdogmus, S. *et al.* Cavβ1 regulates T cell expansion and apoptosis independently of voltage-gated Ca2+ channel function. *Nat. Commun.* **13**, 1–19 (2022).

119. Yaganoglu, S. *et al.* GenEPi: Piezo1-based fluorescent reporter for visualizing mechanical stimuli with high spatiotemporal resolution. *BioRxiv* 1–33 (2019). doi:10.1101/702423

120. Atcha, H. *et al.* Mechanically activated ion channel Piezo1 modulates macrophage polarization and stiffness sensing. *Nat. Commun.* **12**, 1–14 (2021).

121. Babich, A. & Burkhardt, J. K. Coordinate control of cytoskeletal remodeling and calcium mobilization during T-cell activation. *Immunol. Rev.* **256**, 80–94 (2013).

122. Miller, B. C. *et al.* Subsets of exhausted CD8+ T cells differentially mediate tumor control and respond to checkpoint blockade. *Nat. Immunol.* **20**, 326–336 (2019).

123. LaFleur, M. W. *et al.* PTPN2 regulates the generation of exhausted CD8+ T cell subpopulations and restrains tumor immunity. *Nat. Immunol.* **20**, 1335–1347 (2019).

124. Hannezo, E. & Heisenberg, C. P. Mechanochemical Feedback Loops in Development and Disease. *Cell* **178**, 12–25 (2019).

125.   Mangan, M. S. J. *et al.* A novel serpin regulatory mechanism : SerpinB9 is reversibly inhibited by vicinal disulfide bond formation in the reactive center loop. *J. Biol. Chem.* **291**, 3626–3638 (2016).

126.   Kleffel, S. *et al.* Melanoma Cell-Intrinsic PD-1 Receptor Functions Promote Tumor Growth. *Cell* **162**, 1242–1256 (2015).

127.   Joseph, N., Reicher, B. & Barda-Saad, M. The calcium feedback loop and T cell activation: How cytoskeleton networks control intracellular calcium flux. *Biochim. Biophys. Acta - Biomembr.* **1838**, 557–568 (2014).

128.   Yu, G. T. *et al.* PD-1 blockade attenuates immunosuppressive myeloid cells due to inhibition of CD47/SIRPa axis in HPV negative head and neck squamous cell carcinoma. *Oncotarget* **6**, 42067–42080 (2015).

129.   Terme, M. *et al.* IL-18 induces PD-1-dependent immunosuppression in cancer. *Cancer Res.* **71**, 5393–5399 (2011).

130.   Chen, A. *et al.* The HECT-Type E3 Ubiquitin Ligase AIP2 Inhibits Activation-Induced T-Cell Death by Catalyzing EGR2 Ubiquitination. *Mol. Cell. Biol.* **29**, 5348–5356 (2009).

131.   Yang, Y. *et al.* E3 ligase WWP2 negatively regulates TLR3-mediated innate immune response by targeting TRIF for ubiquitination and degradation. *Proc. Natl. Acad. Sci. U. S. A.* **110**, 5115–5120 (2013).

132.   Maddika, S. *et al.* WWP2 is an E3 ubiquitin ligase for PTEN. *Nat. Cell Biol.* **13**, 728–733 (2011).

133.   Zhi, X. & Chen, C. WWP1: A versatile ubiquitin E3 ligase in signaling and diseases. *Cell. Mol. Life Sci.* **69**, 1425–1434 (2012).

134.   Wolf, I. M. A. & Guse, A. H. Ca2+ microdomains in T-lymphocytes. *Front. Oncol.* **7**, 1–11 (2017).

135.   Svensson, L. *et al.* Calpain 2 controls turnover of LFA-1 adhesions on migrating T lymphocytes. *PLoS One* **5**, (2010).

136.   Stewart, M. P., Mcdowall, A. & Hogg, N. LFA-1–mediated Adhesion Is Regulated by Cytoskeletal Restraint and by a Ca 2. *J. Cell Biol.* **140**, 699–707 (1998).

137.   Li, G. & Iyengar, R. Calpain as an effector of the Gq signaling pathway for inhibition of Wnt/β-catenin-regulated cell proliferation. *Proc. Natl. Acad. Sci. U. S. A.* **99**, 13254–13259 (2002).

138.   Konze, S. A. *et al.* Cleavage of e-cadherin and-catenin by calpain affects wnt signaling and spheroid formation in suspension cultures of human pluripotent stem cells. *Mol. Cell. Proteomics* **13**, 990–1007 (2014).

139.   Benetti, R. *et al.* The calpain system is involved in the constitutive regulation of β-catenin signaling functions. *J. Biol. Chem.* **280**, 22070–22080 (2005).

140.   Ma, J., Wang, R., Fang, X. & Sun, Z. β-catenin/TCF-1 pathway in T cell development and differentiation. *J. Neuroimmune Pharmacol.* **7**, 750–762 (2012).

141.   Yu, Q., Sharma, A. & Sen, J. M. TCF1 and β-catenin regulate T cell development and function. *Immunol. Res.* **47**, 45–55 (2010).

142.   Chen, Z. *et al.* TCF-1-Centered Transcriptional Network Drives an Effector versus Exhausted CD8 T Cell-Fate Decision. *Immunity* **51**, 840-855.e5 (2019).

143. Kalocsay, M. APEX Peroxidase-Catalyzed Proximity Labeling and Multiplexed Quantitative Proteomics. in *Proximity Labeling: Methods and Protocols* (eds. Sunbul, M. & Jäschke, A.) 41–55 (Springer New York, 2019). doi:10.1007/978-1-4939-9537-0_4

144. McAlister, G. C. *et al.* MultiNotch MS3 enables accurate, sensitive, and multiplexed detection of differential expression across cancer cell line proteomes. *Anal. Chem.* **86**, 7150–7158 (2014).

145. Paulo, J. A. *et al.* Quantitative mass spectrometry-based multiplexing compares the abundance of 5000 S. cerevisiae proteins across 10 carbon sources. *J. Proteomics* **148**, 85–93 (2016).

146. Chen, X. *et al.* Sustained high level transgene expression in mammalian cells mediated by the optimized piggyBac transposon system. *Genes Dis.* **2**, 96–105 (2015).

147. Boussiotis, V. A., Chatterjee, P. & Li, L. Biochemical Signaling of PD-1 on T Cells and Its Functional Implications. *Cancer J.* **20**, 265–271 (2014).

148. Chemnitz, J. M., Lanfranco, A. R., Braunstein, I. & Riley, J. L. B and T Lymphocyte Attenuator-Mediated Signal Transduction Provides a Potent Inhibitory Signal to Primary Human CD4 T Cells That Can Be Initiated by Multiple Phosphotyrosine Motifs. *J. Immunol.* **176**, 6603–6614 (2006).

149. Staub, E., Rosenthal, A. & Hinzmann, B. Systematic identification of immunoreceptor tyrosine-based inhibitory motifs in the human proteome. *Cell. Signal.* **16**, 435–456 (2004).

150. Billadeau, D. D. & Leibson, P. J. ITAMs versus ITIMs: Striking a balance during cell regulation. *J. Clin. Invest.* **109**, 161–168 (2002).

151. Cannons, J. L., Tangye, S. G. & Schwartzberg, P. L. SLAM family receptors and SAP adaptors in immunity. *Annu. Rev. Immunol.* **29**, 665–705 (2011).

152. Akbani, R. *et al.* Realizing the promise of reverse phase protein arrays for clinical, translational, and basic research: A workshop report the RPPA (Reverse Phase Protein Array) Society. *Mol. Cell. Proteomics* **13**, 1625–1643 (2014).

153. Wang, H. *et al.* ZAP-70: an essential kinase in T-cell signaling. *Cold Spring Harb. Perspect. Biol.* **2**, 1–17 (2010).

154. Carpino, N. *et al.* Regulation of ZAP-70 Activation and TCR Signaling by Two Related Proteins, Sts-1 and Sts-2. *Immunity* **20**, 37–46 (2004).

155. Rao, N., Dodge, I. & Band, H. The Cbl family of ubiquitin ligases: critical negative regulators of tyrosine kinase signaling in the immune system. *J. Leukoc. Biol.* **71**, 753–63 (2002).

156. Raguz, J., Wagner, S., Dikic, I. & Hoeller, D. Suppressor of T-cell receptor signalling 1 and 2 differentially regulate endocytosis and signalling of receptor tyrosine kinases. *FEBS Lett.* **581**, 4767–4772 (2007).

157. Lutz-Nicoladoni, C., Wolf, D. & Sopper, S. Modulation of immune cell functions by the E3 ligase CBL-b. *Front. Oncol.* **5**, 1–14 (2015).

158. San Luis, B., Sondgeroth, B., Nassar, N. & Carpino, N. Sts-2 is a phosphatase that negatively regulates Zeta-associated Protein (ZAP)-70 and T cell receptor signaling pathways. *J. Biol. Chem.* **286**, 15943–15954 (2011).

159. Bennett, A. M., Tang, T. L., Sugimoto, S., Walsh, C. T. & Neel, B. G. Protein-tyrosine-phosphatase SHPTP2 couples platelet-derived growth factor receptor β to Ras. *Proc. Natl. Acad. Sci. U. S. A.* **91**, 7335–7339 (1994).

160. Stark, B. C., Lanier, M. H. & Cooper, J. A. CARMIL family proteins as multidomain regulators of actin-based motility. *Mol. Biol. Cell* **28**, 1713–1723 (2017).

161. Schober, T. *et al.* A human immunodeficiency syndrome caused by mutations in CARMIL2. *Nat. Commun.* **8**, (2017).

162. Gong, Q. *et al.* Disruption of T cell signaling networks and development by Grb2 haploid insufficiency. *Nat. Immunol.* **2**, 29–36 (2001).

163. Dustin, M. L. & Davis, S. J. TCR signaling: The barrier within. *Nat. Immunol.* **15**, 136–137 (2014).

164. Tan, Y. X. *et al.* Inhibition of the kinase Csk in thymocytes reveals a requirement for actin remodeling in the initiation of full TCR signaling. *Nat. Immunol.* **15**, 186–194 (2014).

165. Finlay, D. & Cantrell, D. The coordination of T-cell function by serine/threonine kinases. *Cold Spring Harb. Perspect. Biol.* **3**, 1–10 (2011).

166. Piotrowski, J. T., Gomez, T. S., Schoon, R. A., Mangalam, A. K. & Billadeau, D. D. WASH Knockout T Cells Demonstrate Defective Receptor Trafficking, Proliferation, and Effector Function. *Mol. Cell. Biol.* **33**, 958–973 (2013).

167. Busman-Sahay, K., Drake, L., Sitaram, A., Marks, M. & Drake, J. R. Cis and Trans Regulatory Mechanisms Control AP2-Mediated B Cell Receptor Endocytosis via Select Tyrosine-Based Motifs. *PLoS One* **8**, (2013).

168. Lu, X. *et al.* AP2 Adaptor Complex-Dependent Internalization of CD5: Differential Regulation in T and B Cells. *J. Immunol.* **168**, 5612–5620 (2002).

169. Seimiya, H., Muramatsu, Y., Smith, S. & Tsuruo, T. Functional Subdomain in the Ankyrin Domain of Tankyrase 1 Required for Poly(ADP-Ribosyl)ation of TRF1 and Telomere Elongation. *Mol. Cell. Biol.* **24**, 1944–1955 (2004).

170. DaRosa, P. A., Klevit, R. E. & Xu, W. Structural basis for tankyrase-RNF146 interaction reveals noncanonical tankyrase-binding motifs. *Protein Sci.* **27**, 1057–1067 (2018).

171. Kim, G., Kim, J. Y. & Choi, H. S. Peptidyl-prolyl cis/trans isomerase NIMA-interacting 1 as a therapeutic target in hepatocellular carcinoma. *Biol. Pharm. Bull.* **38**, 975–979 (2015).

172. Kim, G., Bhattarai, P. Y. & Choi, H. S. Peptidyl-prolyl cis/trans isomerase NIMA-interacting 1 as a molecular target in breast cancer: a therapeutic perspective of gynecological cancer. *Arch. Pharm. Res.* **42**, 128–139 (2019).

173. Pu, W., Zheng, Y. & Peng, Y. Prolyl Isomerase Pin1 in Human Cancer: Function, Mechanism, and Significance. *Front. Cell Dev. Biol.* **8**, 1–11 (2020).

174. Tan, C. L. *et al.* PD-1 restraint of regulatory T cell suppressive activity is critical for immune tolerance. *J. Exp. Med.* **218**, 1–17 (2020).

175. Daneshpour, H. & Youk, H. Modeling cell–cell communication for immune systems across space and time. *Curr. Opin. Syst. Biol.* **18**, 44–52 (2019).

176. LaFleur, M. W. *et al.* A CRISPR-Cas9 delivery system for in vivo screening of genes in the immune system. *Nat. Commun.* **10**, 1–10 (2019).

177. Liu, G. *et al.* Mechanism of adrenergic CaV1.2 stimulation revealed by proximity proteomics. *Nature* **577**, 695–700 (2020).

178. Fujiwara, M., Anstadt, E. J. & Clark, R. B. Cbl-b deficiency mediates resistance to programmed death-ligand 1/programmed death-1 regulation. *Front. Immunol.* **8**, 1–12 (2017).

179. Karwacz, K. *et al.* PD-L1 co-stimulation contributes to ligand-induced T cell receptor down-modulation on CD8 + T cells. *EMBO Mol. Med.* **3**, 581–592 (2011).

180. Lyle, C. *et al.* c-Cbl targets PD-1 in immune cells for proteasomal degradation and modulates colorectal tumor growth. *Sci. Rep.* **9**, 1–14 (2019).

181. Ge, Y., Paisie, T. K., Chen, S. & Concannon, P. UBASH3A Regulates the Synthesis and Dynamics of TCR–CD3 Complexes. *J. Immunol.* **203**, 2827–2836 (2019).

182. Kim, W. *et al.* Systematic and quantitative assessment of the ubiquitin-modified proteome. *Mol. Cell* **44**, 325–340 (2011).

183. Udeshi, N. D. *et al.* Rapid and deep-scale ubiquitylation profiling for biology and translational research. *Nat. Commun.* **11**, 1–11 (2020).

184. Kroner, A. *et al.* Accelerated course of experimental autoimmune encephalomyelitis in PD-1-deficient central nervous system myelin mutants. *Am. J. Pathol.* **174**, 2290–2299 (2009).

185. Dominguez-Villar, M., Baecher-Allan, C. M. & Hafler, D. A. Identification of T helper type 1-"like, Foxp3 + regulatory T cells in human autoimmune disease. *Nat. Med.* **17**, 673–675 (2011).

186. Tinti, M. *et al.* The SH2 Domain Interaction Landscape. *Cell Rep.* **3**, 1293–1305 (2013).

187. Hughes, C. S. *et al.* Single-pot, solid-phase-enhanced sample preparation for proteomics experiments. *Nat. Protoc.* **14**, 68–85 (2019).

188. Rappsilber, J., Ishihama, Y. & Mann, M. Stop And Go Extraction tips for matrix-assisted laser desorption/ionization, nanoelectrospray, and LC/MS sample pretreatment in proteomics. *Anal. Chem.* **75**, 663–670 (2003).

189. Li, J. *et al.* TMTpro reagents: a set of isobaric labeling mass tags enables simultaneous proteome-wide measurements across 16 samples. *Nat. Methods* **17**, (2020).

190. Yao, Y. *et al.* Ubash3b promotes TPA-mediated suppression of leukemogenesis through accelerated downregulation of PKCδ protein. *Biochimie* **184**, 8–17 (2021).

191. Cutler, J. A. *et al.* Integrative phosphoproteome and interactome analysis of the role of Ubash3b in BCR-ABL signaling. *Leukemia* **34**, 301–305 (2020).

192. Luis, B. S. & Carpino, N. Insights into the suppressor of T-cell receptor (TCR) signaling-1 (Sts-1)-mediated regulation of TCR signaling through the use of novel substrate-trapping Sts-1 phosphatase variants. *FEBS J.* **281**, 696–707 (2014).

193. Lemmon, M. A., Freed, D. M., Schlessinger, J. & Kiyatkin, A. The Dark Side of Cell Signaling: Positive Roles for Negative Regulators. *Cell* **164**, 1172–1184 (2016).

194. Kumari, S. *et al.* T lymphocyte myosin IIA is required for maturation of the immunological synapse. *Front. Immunol.* **3**, 1–13 (2012).

195. Casella, J., Flannagan, M. & Lin, S. Cytochalasin D inhibits actin polymerization and induces depolymerization of actin filaments formed during platelet shape change. *Nature* **293**, 302–305 (1981).

196. Kovács, M., Tóth, J., Hetényi, C., Málnási-Csizmadia, A. & Seller, J. R. Mechanism of blebbistatin inhibition of myosin II. *J. Biol. Chem.* **279**, 35557–35563 (2004).

197. Chaudhary, N. & Maddika, S. WWP2-WWP1 Ubiquitin Ligase Complex Coordinated by PPM1G Maintains the Balance between Cellular p73 and ΔNp73 Levels. *Mol. Cell. Biol.* **34**, 3754–3764 (2014).

198. Barr, V. A. *et al.* Dynamic Movement of the Calcium Sensor STIM1 and the Calcium Channel Orai1 in Activated T-Cells: Puncta and Distal Caps. *Mol. Biol. Cell* **19**, 2802–2817 (2008).

199. Liang, X., Zhang, N., Pan, H., Xie, J. & Han, W. Development of Store-Operated Calcium Entry-Targeted Compounds in Cancer. *Front. Pharmacol.* **12**, 1–18 (2021).

200. Donkor, I. O. An update on the therapeutic potential of calpain inhibitors: a patent review. *Expert Opin. Ther. Pat.* **30**, 659–676 (2020).

201. Lewis, A. H. & Grandl, J. Inactivation Kinetics and Mechanical Gating of Piezo1 Ion Channels Depend on Subdomains within the Cap. *Cell Rep.* **30**, 870-880.e2 (2020).

202. Zhang, X. *et al.* Structural and Functional Analysis of the Costimulatory Receptor Programmed Death-1. *Immunity* **20**, 337–347 (2004).

# Appendix

## Supplemental materials to accompany Chapter 2
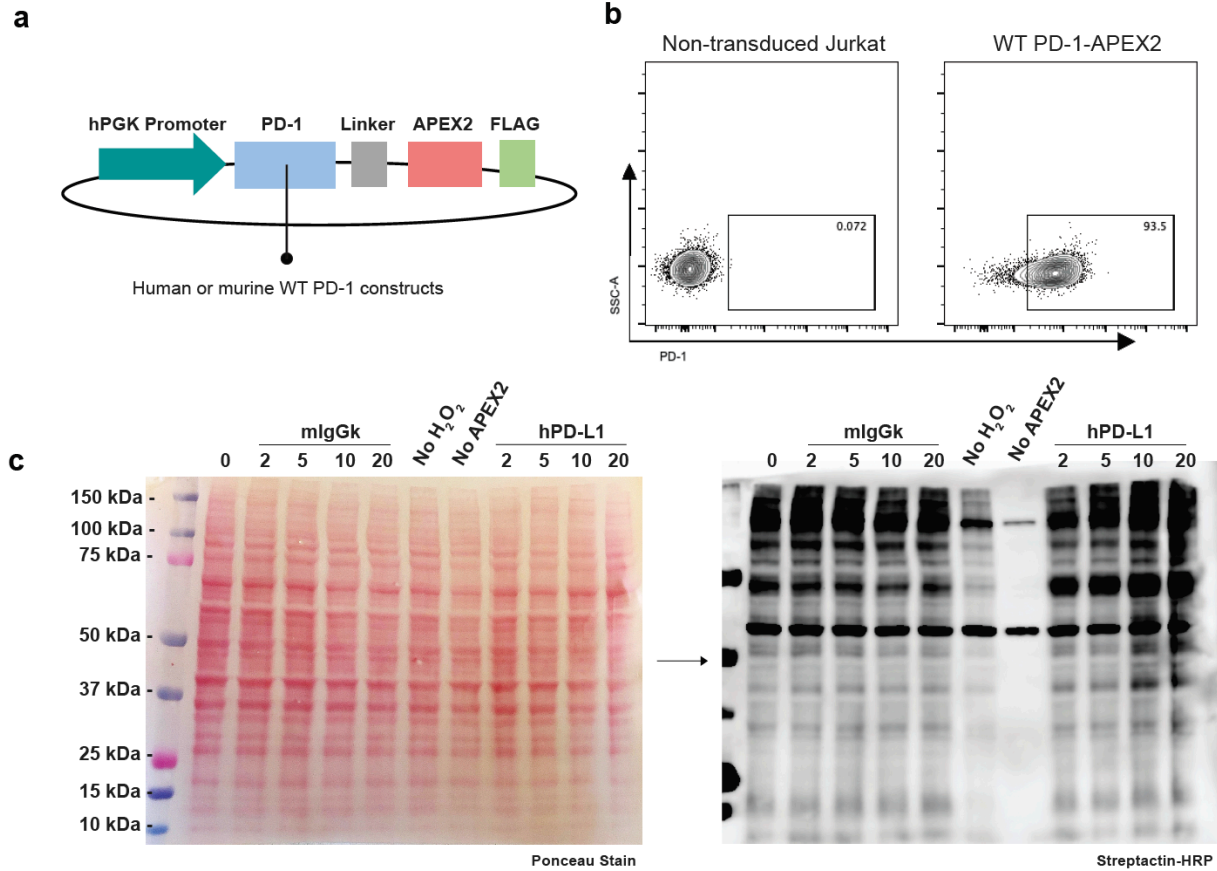
**Figure 2.S1: PD-1-APEX2 construct design and cell line optimization.** a) Design of human and murine PD-1-APEX2 constructs. hPGK denotes the human phosphoglycerate kinase promoter. b) PD-1-APEX2 expression in Jurkat cells measured by flow cytometry compared to unstimulated, non-lentivirally transduced Jurkat cells. c) Labelling efficiency of PD-1-APEX2 probe via Western blot stained with Ponceau to assess protein loading and probed with streptactin-HRP.
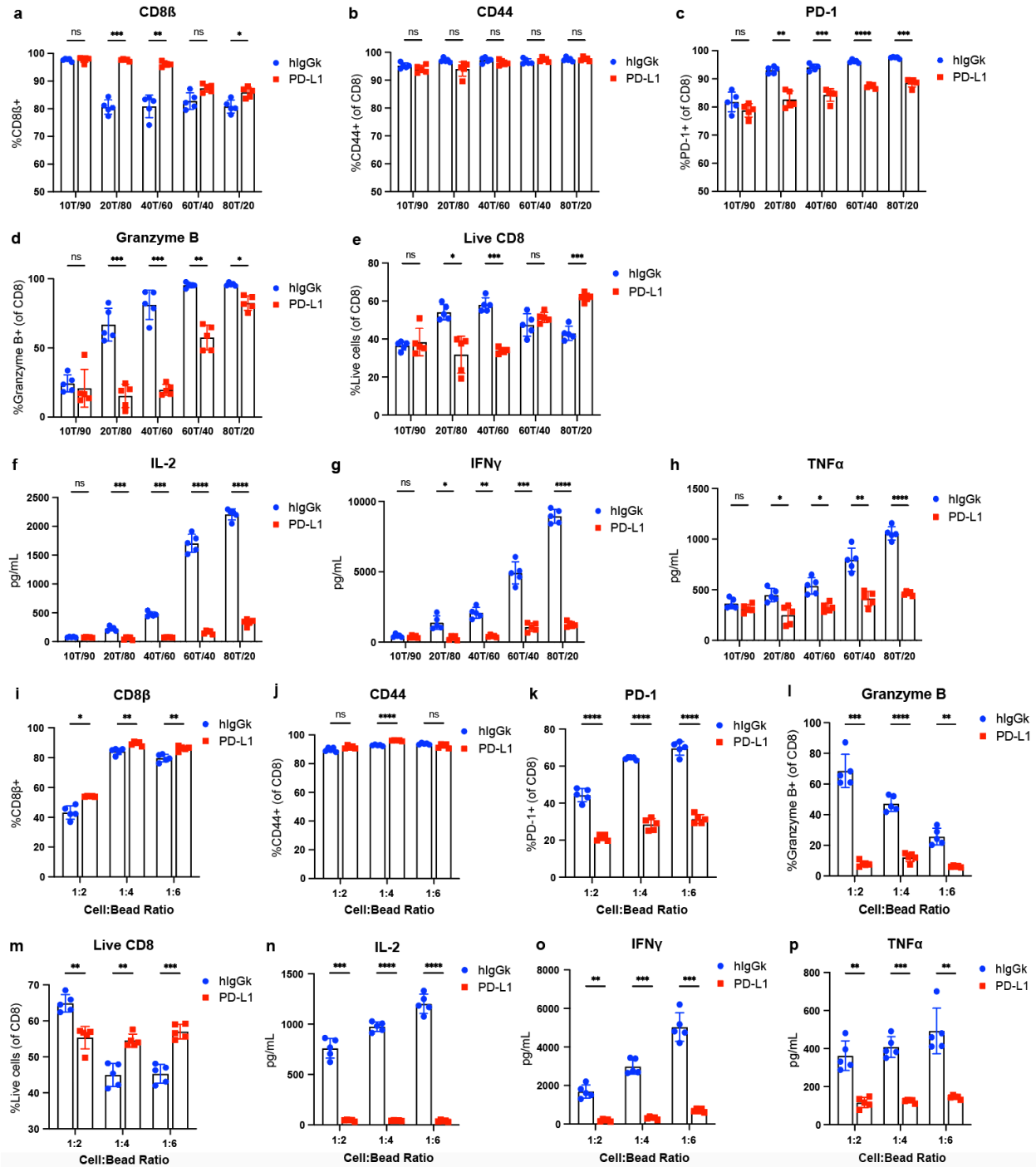
**Figure 2.S2: PD-L1-TCR and TCR-control Dynabead optimization.** Tosyl-activated Dynabeads coated with various ratios of crosslinking-CD3/CD28 antibodies and recombinant murine PD-L1 or human IgG$_1$κ (hIgG$_1$κ) control ligand (x-axis) were incubated with murine CD8$^+$ T cells for 48 h to assess expression of a) CD8β, b) CD44, c) PD-1, d) granzyme B, and percentage of e) live cells via flow cytometry. Cell culture supernatants were collected to assess concentrations of excreted cytokines f) IL-2, g) IFNγ and h) TNFα using CBA assay. The x-axis denotes specified protein ratios where "T" represents the combined percentage of TCR components CD3 and CD28 while the latter number represents percentage of murine PD-L1 or hIgG$_1$κ on the beads.

123

**(Figure 2.S2 Continued)** Increasing concentrations of beads coated with 60% PD-L1 and 40% TCR components selected from the previous assay were incubated with primary murine CD8$^+$ T cells for 48 h to assess expression of i) CD8$\beta$, j) CD44, k) PD-1, l) granzyme B and percentage of m) live cells via flow cytometry. Cell culture supernatants were collected to assess levels of excreted cytokines n) IL-2, o) IFN$\gamma$, p) TNF$\alpha$ using CBA assay. Data are presented as means of n=5 biological replicates ± SD. Statistical significance was assessed between control and PD-L1 groups using two-way ANOVA analysis. ns, * p<0.05, ** p<0.01, *** p<0.001, **** p<0.0001.
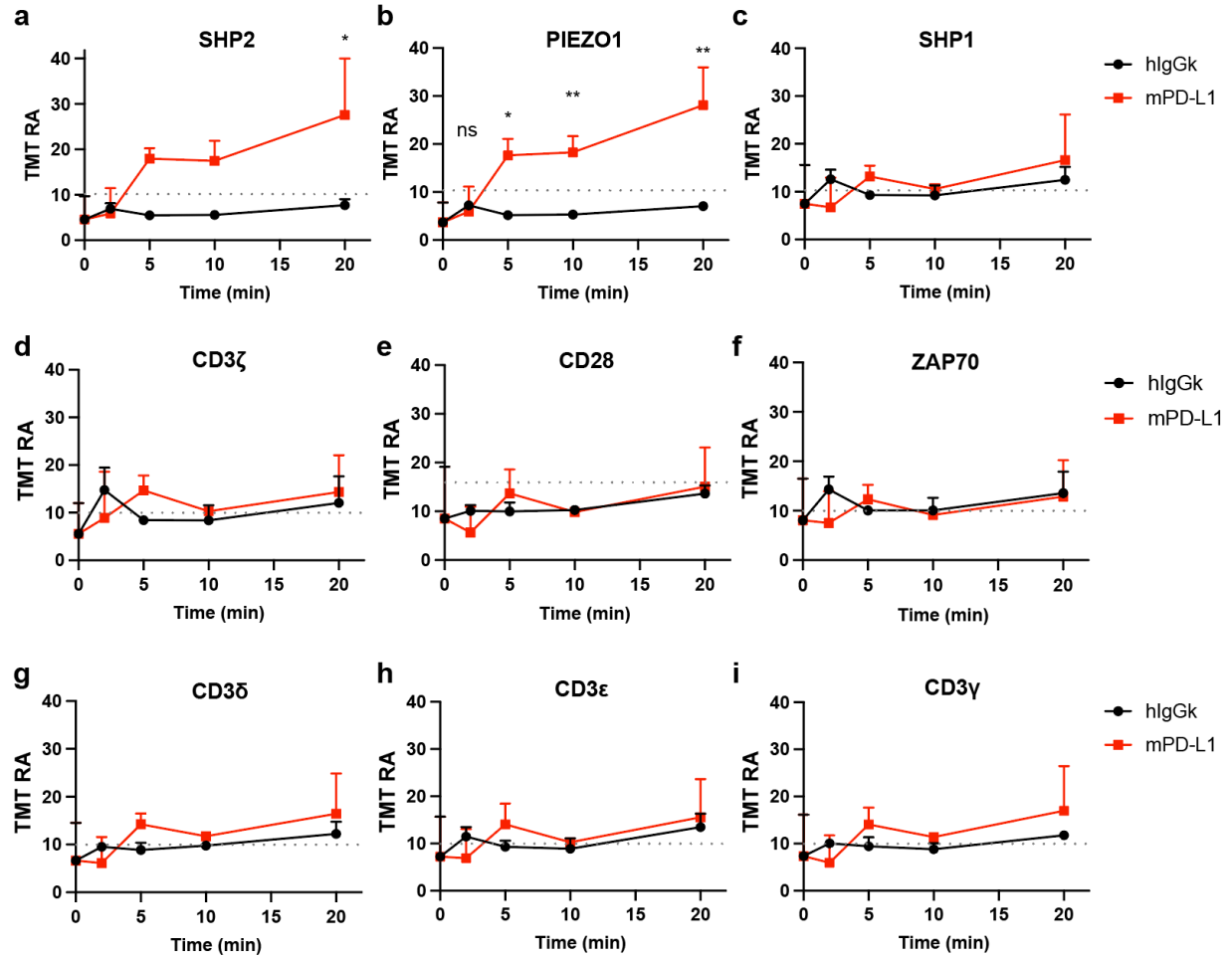
**Figure 2.S3: APEX2 proximity labelling identifies PIEZO1 as target of murine PD-1.** TMT ratios over time (min) of a) SHP2, b) PIEZO1, c) SHP1, d) CD3$\zeta$, e) CD28, f) ZAP70, g) CD3$\delta$, h) CD3$\epsilon$ and i) CD3$\gamma$ following stimulation of murine PD-1-APEX2 with murine PD-L1 (mPD-L1) or control hIgG$_1\kappa$ beads. Data are represented as means ± SD from two independent experiments using two-way ANOVA analysis comparing PD-L1 and control hIgG$_1\kappa$ bead-treated groups. Only significant differences are indicated. * $p < 0.05$, ** $p < 0.01$, *** $p < 0.001$, **** $p < 0.0001$.
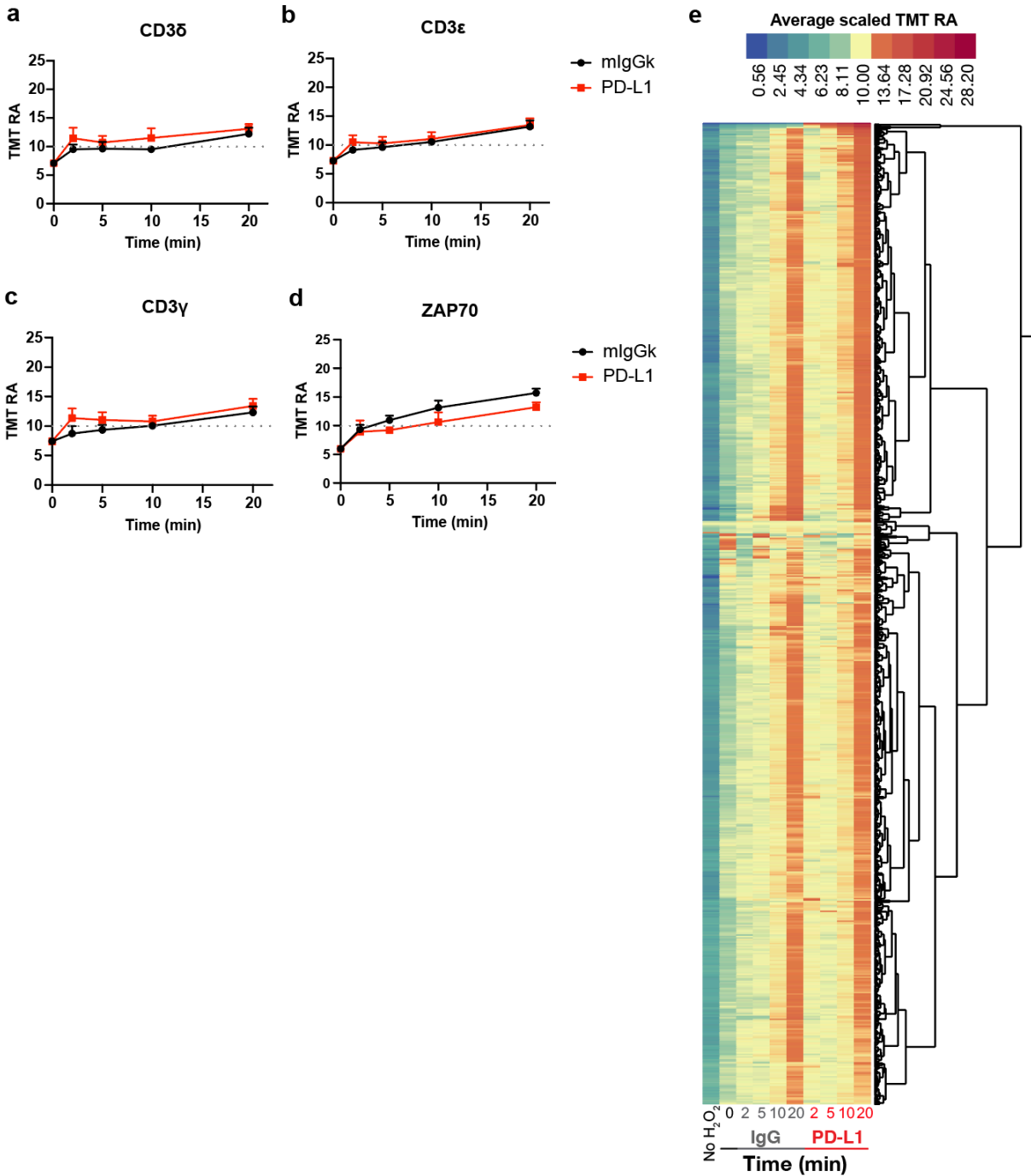
**Figure 2.S4: Additional PD-1-APEX2 findings**. TMT ratios over time (min) of a) CD3$\delta$, b) CD3$\varepsilon$, c) CD3$\gamma$ and d) ZAP70 following stimulation of PD-1-APEX2 with TCR-PD-L1 or TCR-control mIgG$_{1\kappa}$ beads. Data are presented as means from three independent experiments ± SD. Statistical significance was assessed using two-way ANOVA analysis comparing TCR-PD-L1 and TCR-control mIgG$_{1\kappa}$ bead-treated groups. Only significant differences are indicated. * p<0.05, ** p<0.01, *** p<0.001, **** p<0.0001. e) Hierarchical one-way clustering of the averaged TMT ratios of all identified proteins calculated from three independent experiments.
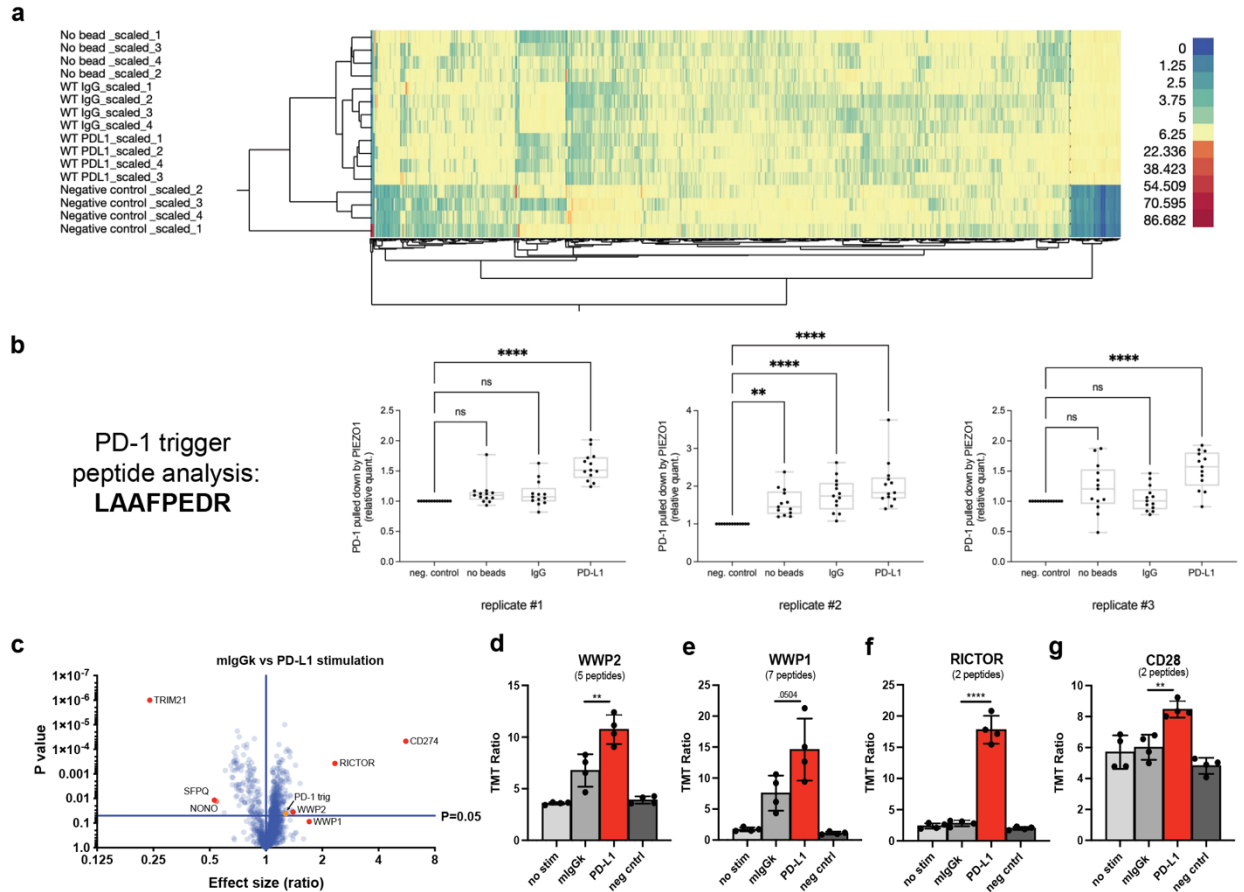
**Figure 2.S5: PIEZO1 IP and PD-1 trigger peptide analysis.** a) Two-way hierarchical clustering of PIEZO1 IP conditions in quadruplicate using ACACA normalized values. b) PD-1 peptide sequence used for triggering and peptide quantifications from three replicates in each condition. Samples were normalized to negative control. Data are presented as means of n=13 ± SD. Statistical significance was assessed using one-way ANOVA analysis. c) Volcano plot depicting p value versus effect size between PD-L1-TCR and TCR-control conditions from PIEZO1 IP. Data presented as means of n=4 ± SD. Statistical significance was assessed using Student's multiple unpaired t tests. Scaled TMT ratios of d) WWP2, e) WWP1, f) RICTOR and g) CD28. Data are represented means of n=4 ± SD. Statistical significance was assessed between TCR-PD-L1 and TCR-control conditions using Student's unpaired t test. ns, * p<0.05, ** p<0.01, *** p<0.001, **** p<0.0001.
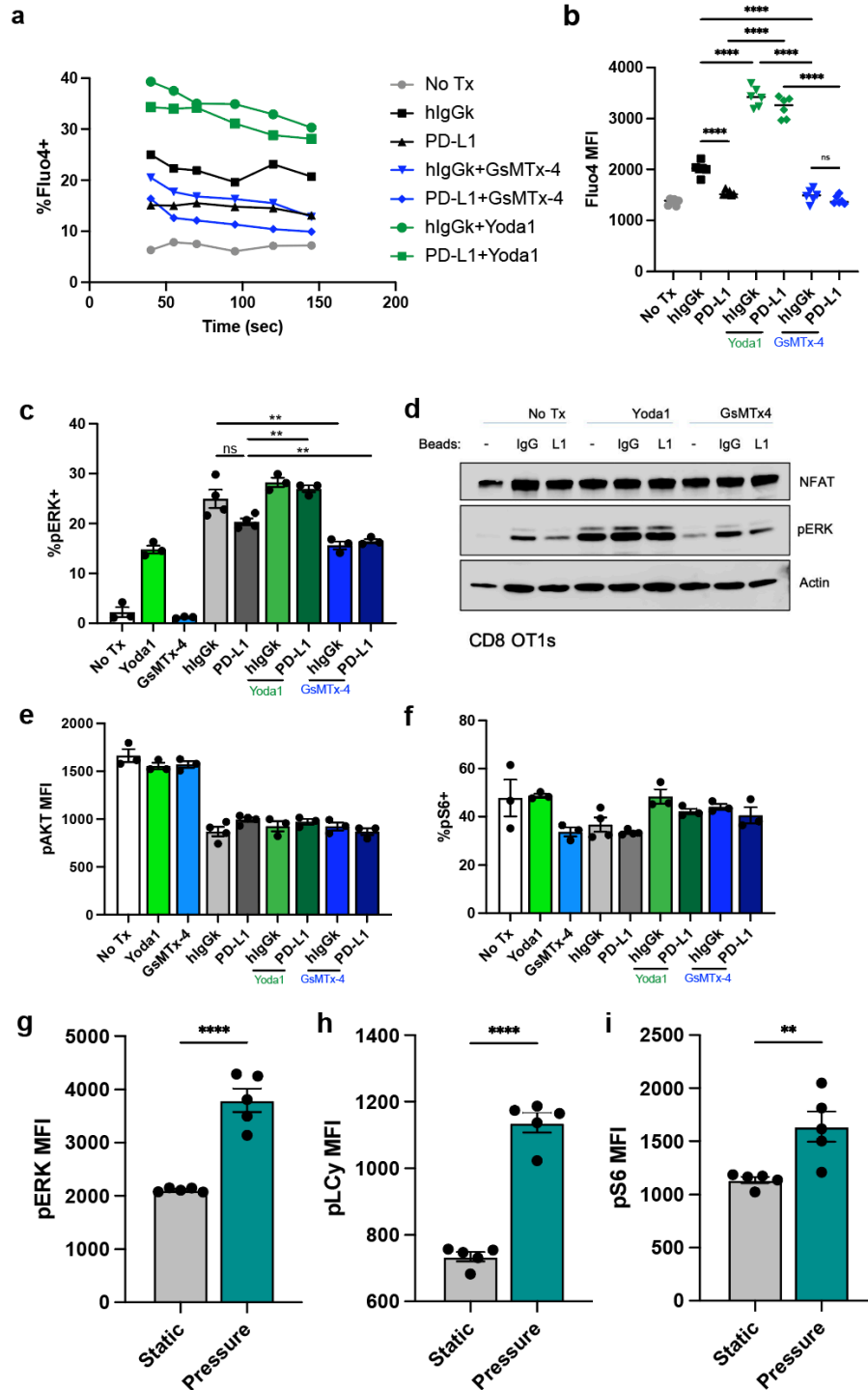
**Figure 2.S6: PIEZO1 modulation alters CD8$^+$ T cell Ca$^{2+}$ influx and signaling.** Murine CD8$^+$ T cells stained with Fluo-4 and restimulated with TCR-PD-L1 or TCR-control beads in the presence or absence of PIEZO1 agonist Yoda1 (5$\mu$M) or antagonist GsMTx-4 (2.5 $\mu$M) and assessed for a) percentage of bound Ca$^{2+}$ over time (s) and b) mean fluorescence intensity (MFI). Data presented as means of n=6 timepoints ± SD. Statistical significance was assessed using one-way ANOVA analysis. Frequencies of c) pERK, e) pAKT after 10 min and f) pS6 after 30 min analyzed using phospho-flow cytometry. Data presented as means of n=3-4 biological replicates ± SD. Statistical significance was measured using Student's unpaired t test.

128

**(Figure 2.S6 Continued)** Western blotting analysis of OT1 CD8$^+$ T cells pretreated for 5 min with 5uM DMSO, Yoda1 or GsMTx-4 and restimulated for 20 min with PD-L1 or control beads to assess protein levels of pERK and NFAT using $\beta$-actin as loading control. MFI of g) pERK, h) pLC$\gamma$ and i) pS6 following 20 min exposure to static or cyclical hydrostatic pressure and analyzed using phospho-flow cytometry. Data are presented as means of n=5 ± SD. Statistical significance was measured using Student's unpaired t test. ns, * p<0.05, ** p<0.01, *** p<0.001, **** p<0.0001.
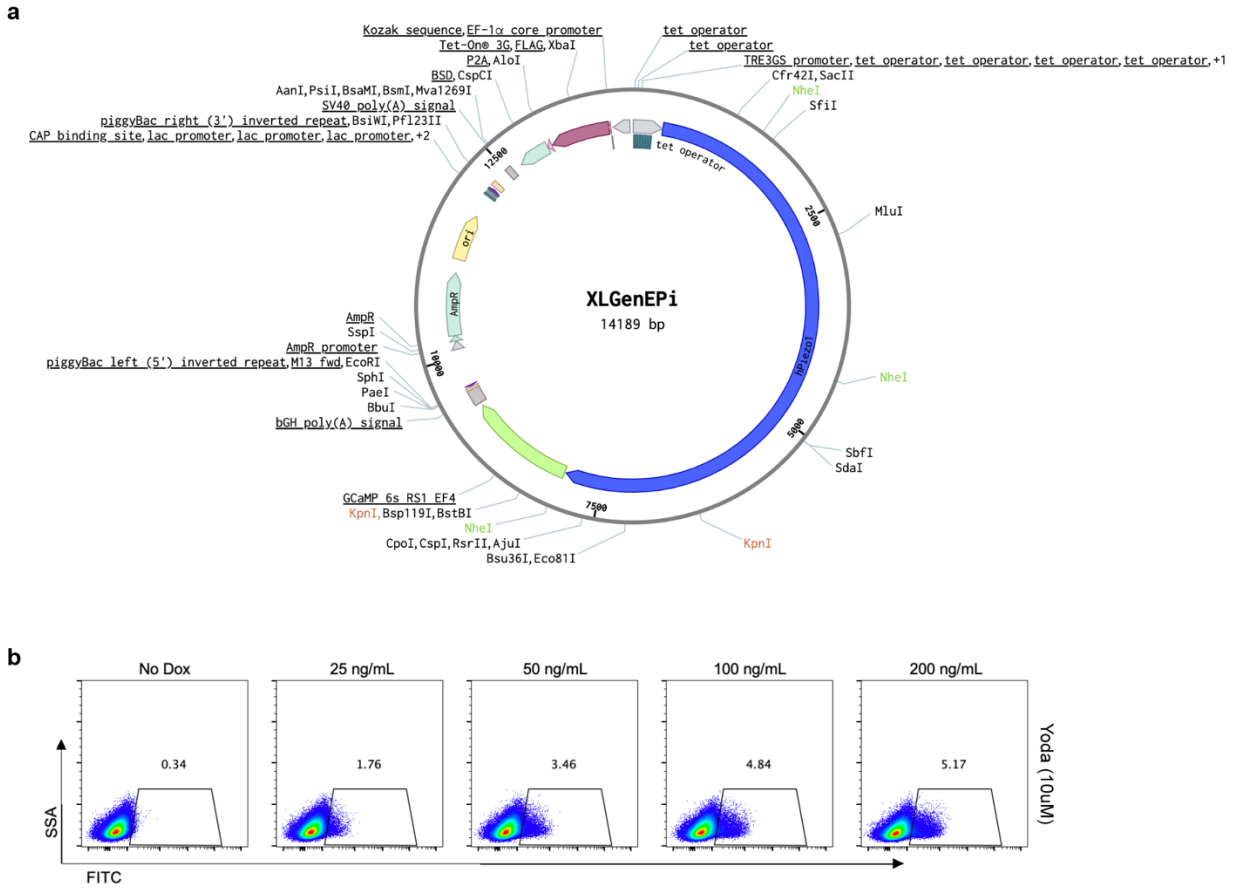
**Figure 2.S7: XLGenEPi inducible expression in Jurkat cells.** a) XLGenEPi plasmid map. b) Electroporated and blasticidin-selected XLGenEPi Jurkat cells incubated with a dose titration of doxycycline (25-200ng/mL) for 24 h and treated with $10\mu$M Yoda1 immediately prior to flow cytometric analysis. Number on plots indicates frequency.
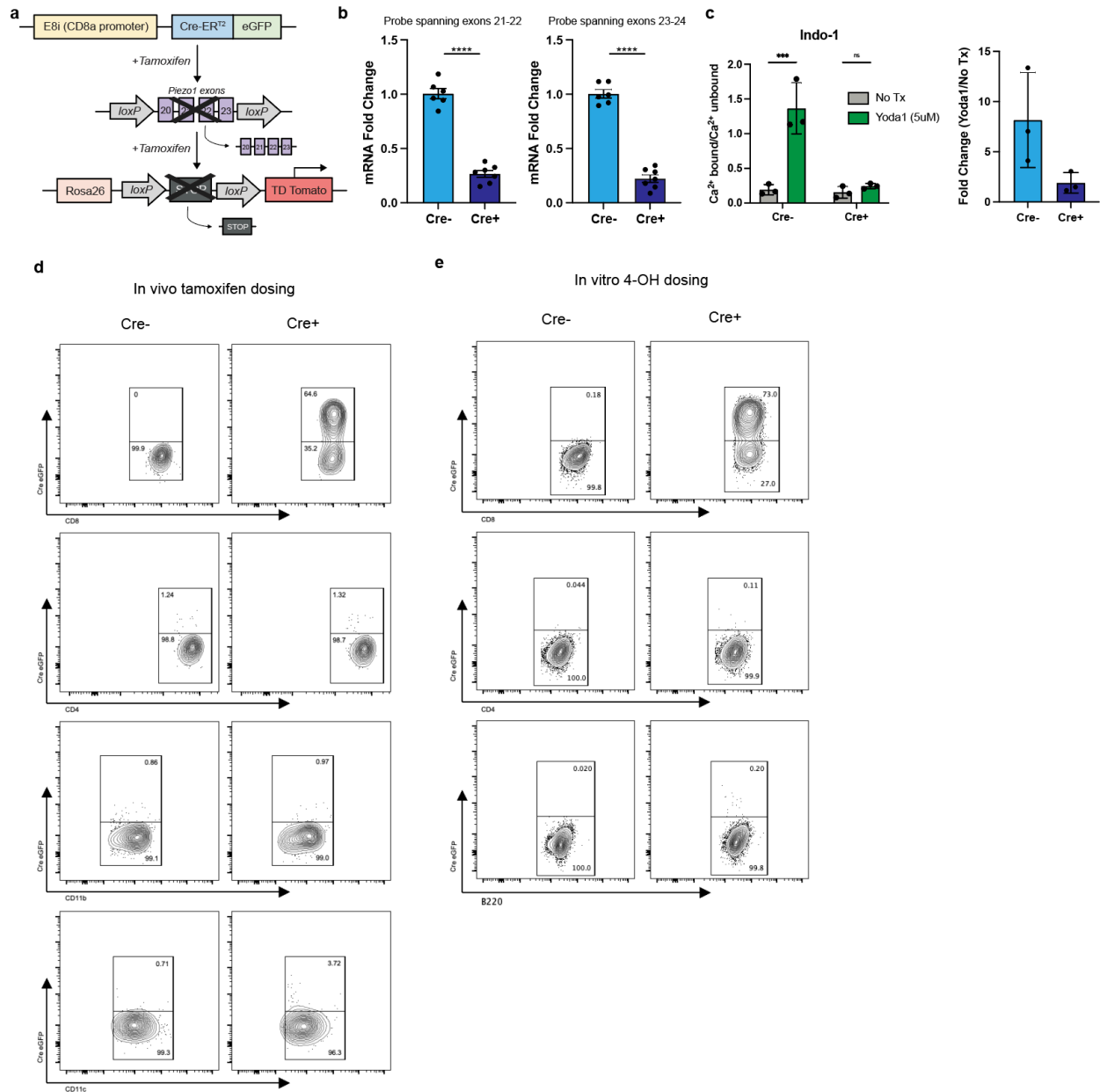
**Figure 2.S8: E8i-Cre-ER^T2 PIEZO1 KO is specific to CD8+ T cells.** a) Schematic of E8i-Cre-ER^T2 *Piezo1^flx/flx* mouse model. b) Relative fold change of PIEZO1 expression in Cre+ and Cre- CD8+ T cells following 8 doses of 100mg tamoxifen using qPCR and TaqMan probes recognizing specific Piezo1 floxed regions. Data are presented as means of n=6 ± SD. Statistical significance was assessed using Student's unpaired t-test. c) Ratio of bound/unbound $Ca^{2+}$ and fold change of $Ca^{2+}$ influx in non-treated versus Yoda1-treated CD8+ T cells from Cre+ and Cre- mice stained with Indo-1 following tamoxifen dosing. Data are presented as means of n=3 ± SD. Statistical significance was assessed using Student's unpaired t-test. * $p<0.05$, ** $p<0.01$, *** $p<0.001$, **** $p<0.0001$. d) Flow cytometric analysis comparing Cre expression using an eGFP reporter in Cre+ or Cre- murine CD8+, CD4+, CD11b+ and CD11c+ splenocytes following *in vivo* tamoxifen treatment. e) Flow cytometric analysis comparing Cre expression using an eGFP reporter in Cre+ or Cre- murine CD8+, CD4+ and B220+ splenocytes following in vitro 4-OH tamoxifen treatment. Numbers on plots indicate frequencies.
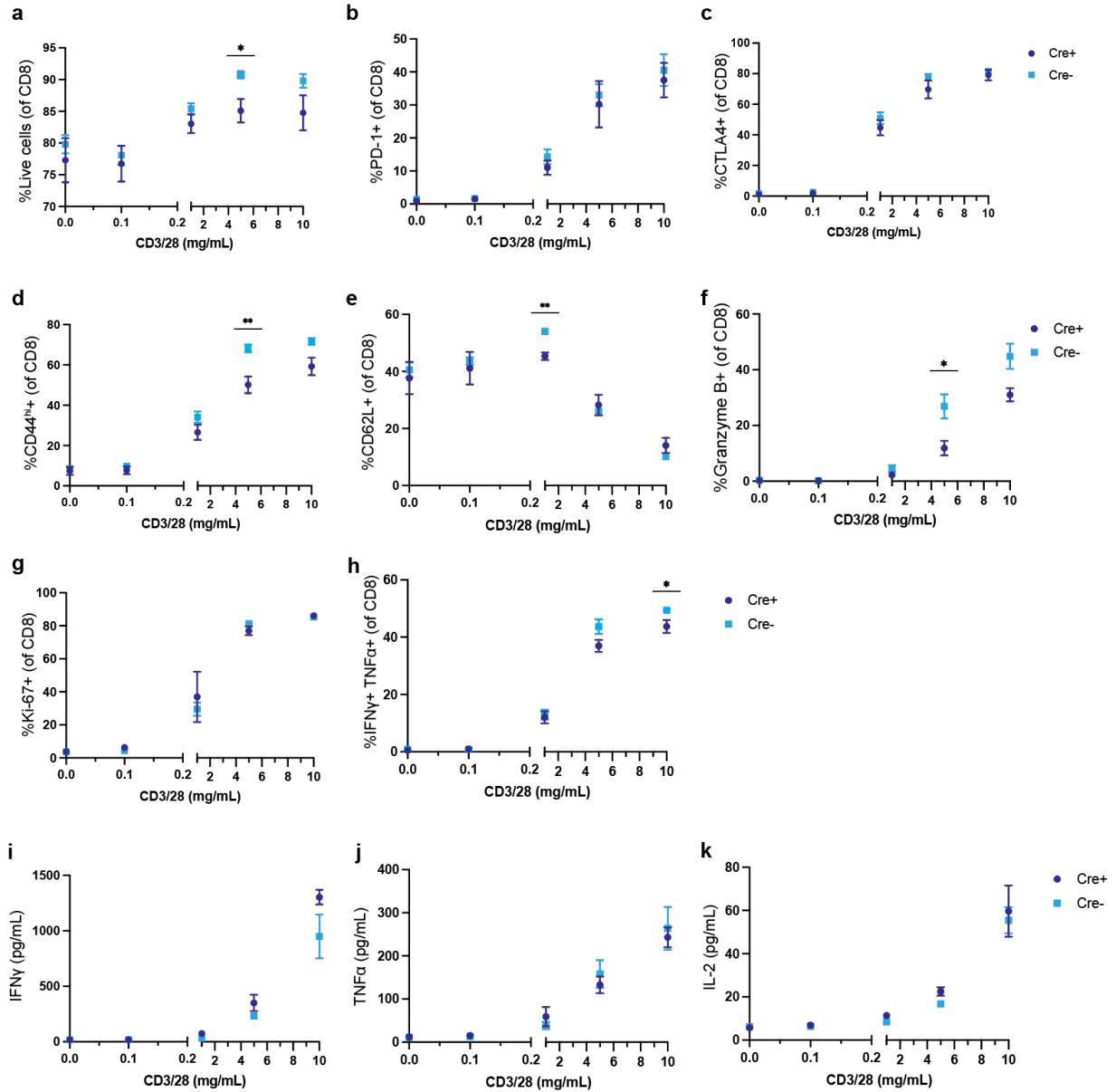
131

**Figure 2.S9: E8i-Cre-ER^T2 *Piezo1^flx/flx* CD8^+ T cells show minimal phenotypic alterations at baseline.** CD8^+ T cells isolated from spleens of Cre+ and Cre- E8i-Cre-ER^T2 *Piezo1^flx/flx* mice were stimulated for 24 h with increasing doses of anti-CD3/CD28 crosslinking antibodies (0-10 ug/mL, x-axis) and assessed for frequencies of a) live cells, b) PD-1, c) CTLA-4, d) CD44, e) CD62L, f) granzyme B, g) Ki-67 and h) IFNγ/TNFα. Cytometric bead array assays were performed on the supernatants of stimulated Cre+ and Cre- CD8^+ T cells to assess concentrations (pg/mL) of i) IFNγ, j) TNFα and k) IL-2. Data are presented as means of n=3-4 ± SD. Statistical significance was assessed using Student's unpaired t-test. Only significant differences are indicated. * p<0.05, ** p<0.01, *** p<0.001, **** p<0.0001.
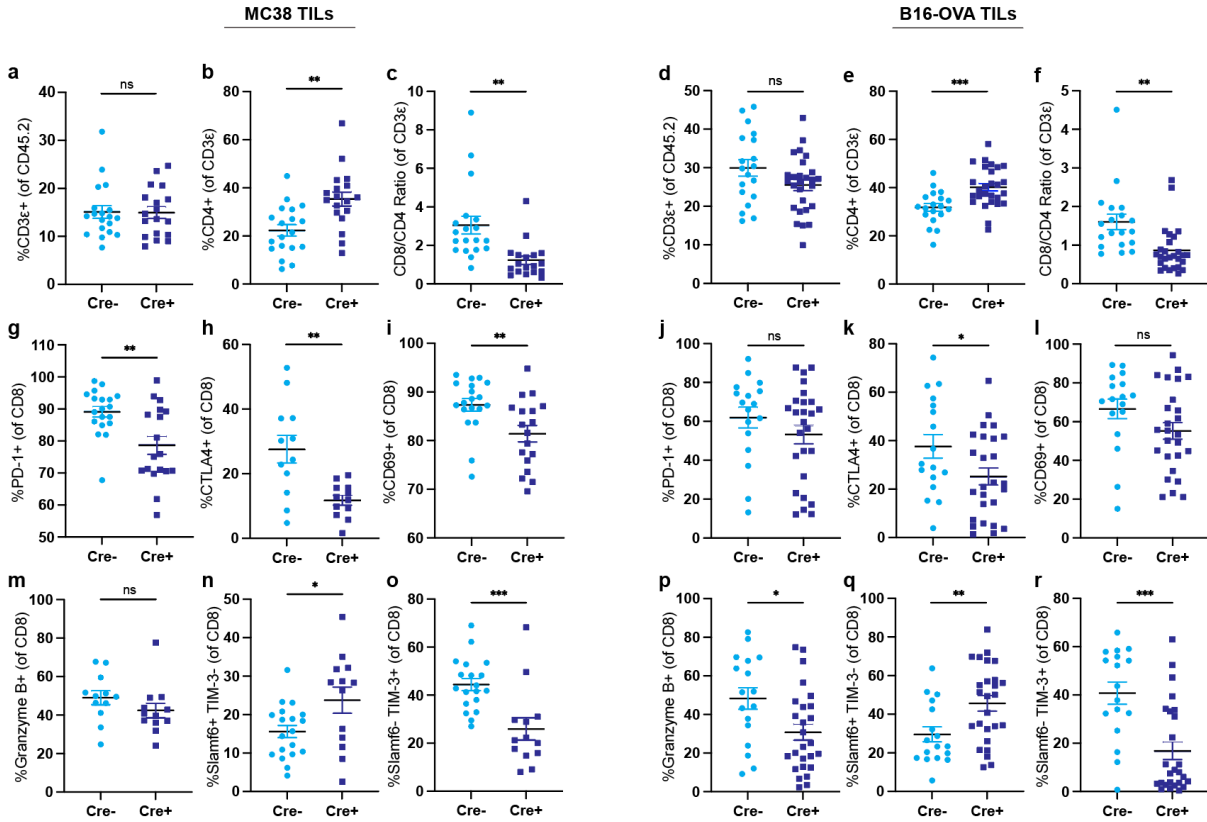
**Figure 2.S10: Flow cytometric analysis of tumor bearing E8i-Cre-ER^T2 *Piezo1^{flx/flx}* mice.** CD8^+ TIL frequencies or counts of a,d) CD3ε, b,e) total CD4^+ T cells, c,f) CD8^+/CD4^+ ratio (counts), g,j) CD69, h,k) CTLA4, i,l)  CD69, m,p) granzyme B, n,q) Slamf6 and o,r) TIM-3 isolated from Cre+ and Cre- mice bearing MC38 or B16-OVA tumors on day 15. Data are presented as means of n=18-26 ± SD from three independent experiments. Statistical significance was measured using Student's unpaired t-test. * p<0.05, ** p<0.01, *** p<0.001, **** p<0.0001.
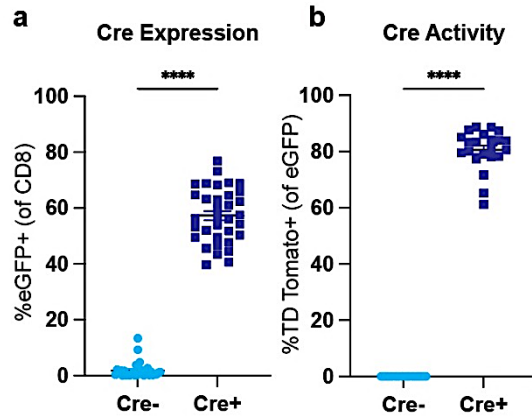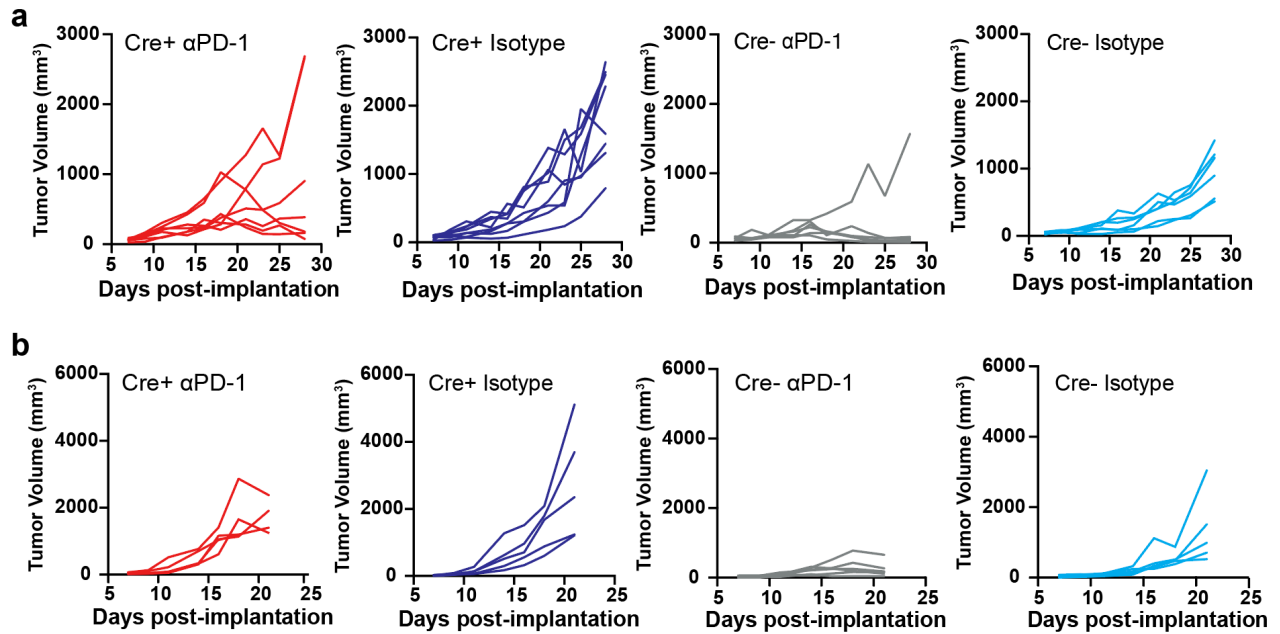
**Figure 2.S11: E8i-Cre-ER^T2 *Piezo1^flx/flx* reporter expression.** a) Cre expression measured by eGFP and b) Cre activity measured by TD-tomato frequencies in CD8$^+$ T cells isolated from the spleen of MC38 and B16-OVA tumor bearing mice at day 15. Data are presented as means of n=22-34 ± SD from four independent experiments. Statistical significance was measured using Student's unpaired t-test. * p<0.05, ** p<0.01, *** p<0.001, **** p<0.0001.

**Figure 2.S12: Individual tumor growth curves of E8i-Cre-ER^{T2} mice.** Individual tumor growth curves from data depicted in Figure 2.3k-l of Cre+ and Cre- E8i-Cre-ER^{T2} PIEZO1^{flx/flx} mice treated with PD-1 blockade or isotype control and bearing a) MC38 or b) B16-OVA tumors.
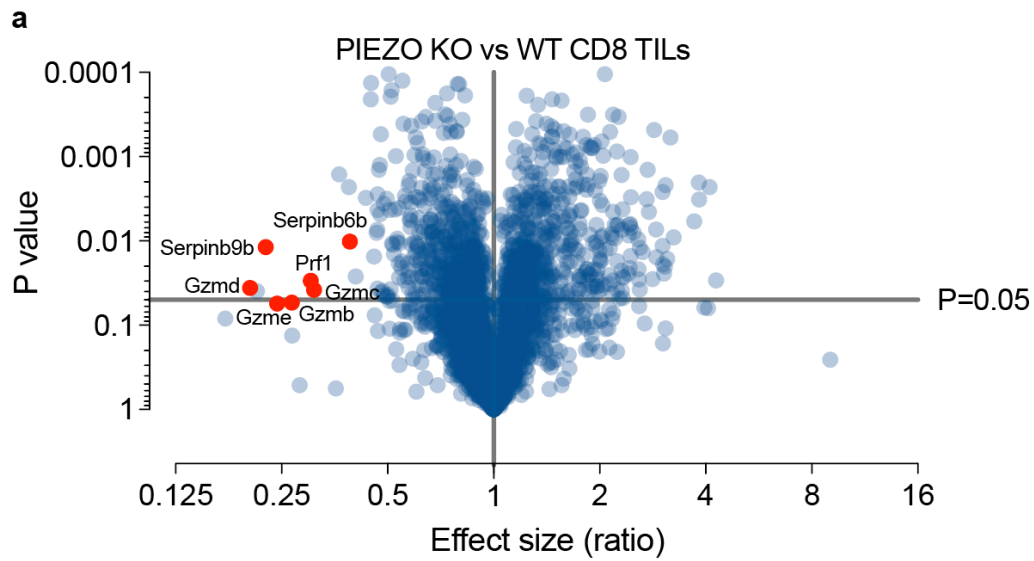
**Figure 2.S13: Proteomic analysis of E8i-Cre-ER$^{T2}$ *Piezo1$^{flx/flx}$* CD8$^+$ TILs.** a) Volcano plot depicting p value versus effect size between CD8$^+$ TILs isolated from Cre+ and Cre- mice on day 15 post B16-OVA tumor implantation. Data are presented as means of n=2-3 ± SD. Statistical significance was assessed using Student's multiple unpaired t tests.
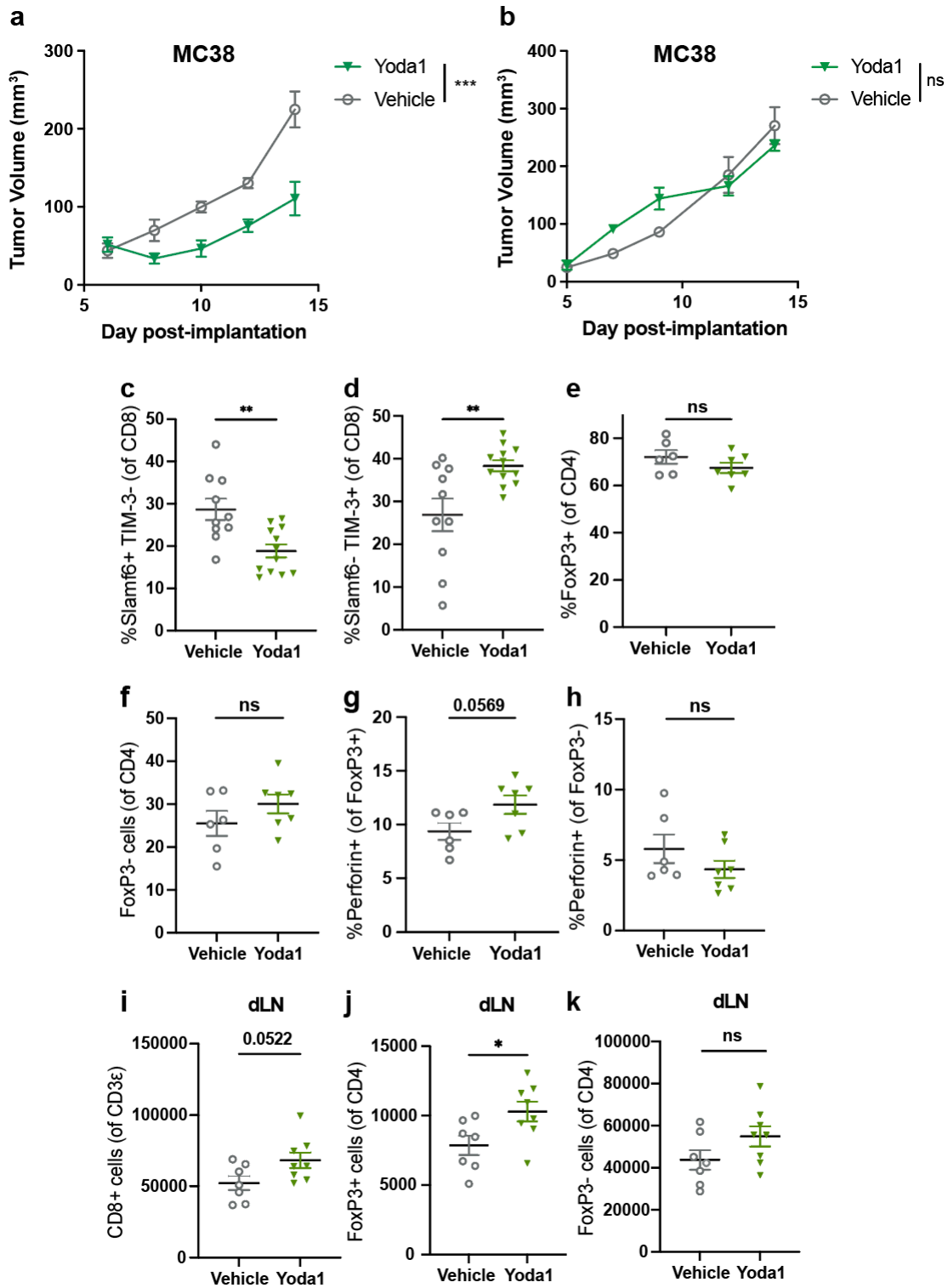
**Figure 2.S14: PIEZO agonism influences TIL phenotypes in WT mice.** Tumor volume (mm$^3$) measured over time (days) for a) trial 1 and b) trial 2 of WT mice bearing MC38 tumors and treated with Yoda1 (7.5 mg/kg). Data are presented as means of n=4-8 ± SD. Statistical significance was assessed using 2-way ANOVA analysis. CD8$^+$ TIL frequencies of c) Slamf6 and d) TIM-3 assessed by flow cytometry. CD4$^+$ TIL frequencies of CD4$^+$ e) Tcon (FoxP3-) f) Treg (FoxP3+), g) Treg perforin and h) Tcon perforin assessed by flow cytometry. Number of i) CD8$^+$ j) Treg and k) Tcon cells recovered from the draining lymph node and assessed by flow cytometry. Data are presented as means of n=6-12 ± SD from one or two independent experiments. Statistical significance was assessed using Student's unpaired t test. ns, * p<0.05, ** p<0.01, *** p<0.001, **** p<0.0001.
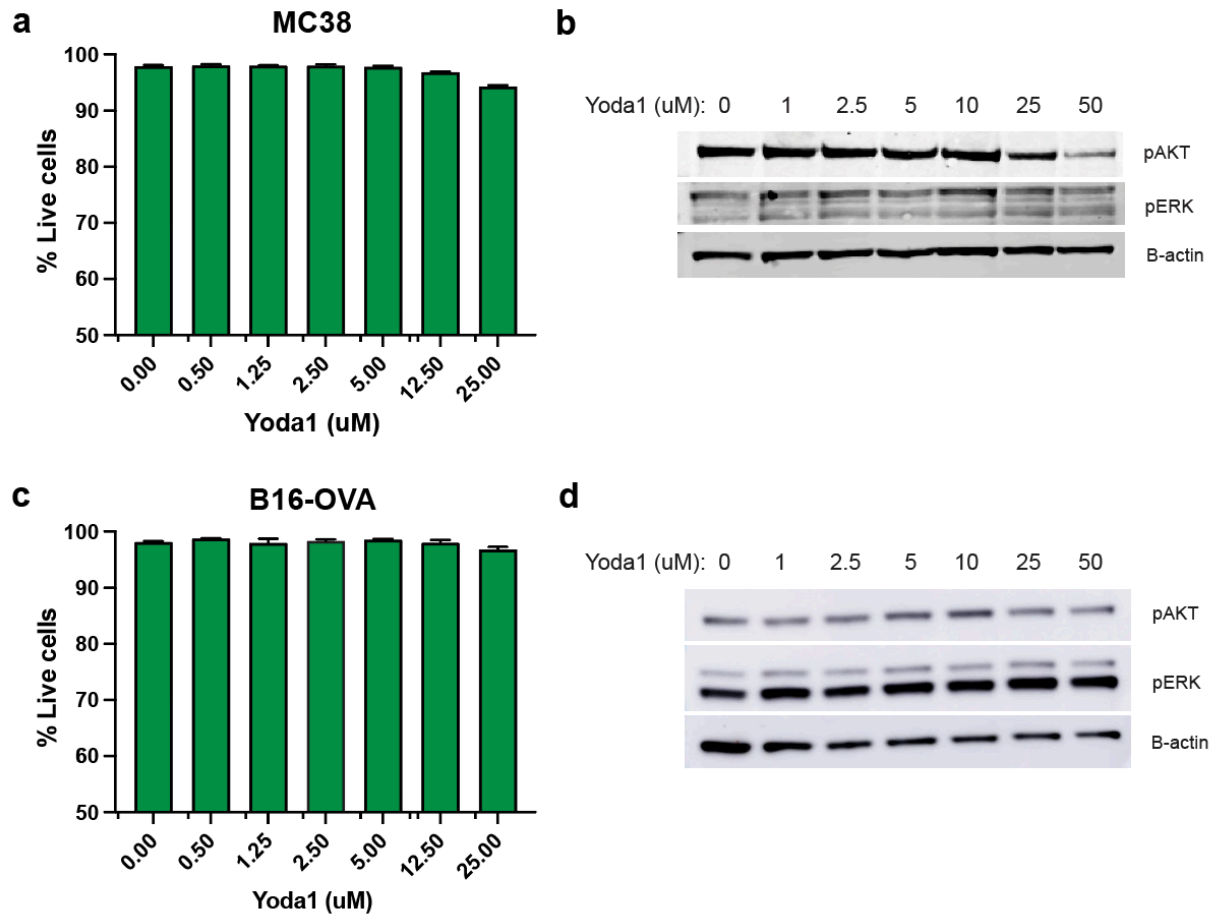
**Figure 2.S15: PIEZO1 agonism does not significantly affect tumor cell viability.** a) MC38 and b) B16-OVA tumor cells treated *in vitro* with increasing doses of Yoda1 (0.5-25μM) and assessed for viability percentages using near-IR live dead staining and flow cytometric analysis. Data are represented means of 6 technical replicates ± SD. Western blotting analysis of c) MC38 and d) B16-OVA tumor cells treated *in vitro* with increasing doses of Yoda1 (1-50μM) for 24 h and assessed for levels of pERK and pAKT using β-actin as a loading control.